MATHEMATICAL MODELS OF CHROMOSOME MOTILITY DURING MITOSIS

by

Blerta Shtylla

A dissertation submitted to the faculty of
The University of Utah
in partial fulfillment of the requirements for the degree of

Doctor of Philosophy

Department of Mathematics

The University of Utah

August 2011

The University of Utah Graduate School

STATEMENT OF DISSERTATION APPROVAL

The dissertation of **Blerta Shtylla**

has been approved by the following supervisory committee members:

James P. Keener	, Chair	**04/22/2011** Date Approved
Aaron Fogelson	, Member	**04/22/2011** Date Approved
Paul Bressloff	, Member	**04/22/2011** Date Approved
Jingyi Zhu	, Member	**4/22/2011** Date Approved
Markus Babst	, Member	**04/22/2011** Date Approved

and by **Aaron Bertram**, Chair of the Department of **Mathematics**

and by Charles A. Wight, Dean of The Graduate School.

ABSTRACT

Cell division is a complex process that involves carefully orchestrated chemical and mechanical events. Tight regulation is vital during division, since a breakdown in control mechanisms can lead to serious disorders such as cancer. A key step in division is the movement of chromosomes to specific locations in the cell with remarkable precision. In higher eukaryotes, the movement of chromosomes has been well observed over the course of hundreds of years. Yet, the mechanisms underlying chromosome motility and the control of precise chromosome localizations in the cell are poorly understood. More recently, a wealth of experimental data has become available for bacterial division. Despite the long supported theory that bacteria and eukaryotes differ widely when undergoing division, it is emerging that similar mechanisms for motility and cell cycle control might be at play in both cell types. Mathematical modeling is useful in the study of these dynamic cellular environments, where it is difficult to experimentally uncover the mechanisms that drive a multitude of mechanical and chemical events. In this dissertation, we develop various mathematical models that address the question of how dynamic polymers can move large objects such as chromosomes in higher eukaryotes and in bacteria. Then, we develop models that address how chemical and mechanical signals can be coordinated to control the precise localization of a chromosome. The mathematical models proposed here employ stochastic differential equations, ordinary differential equations and partial differential equations. The models are numerically simulated to obtain solutions for various parameter values, but we also use tools from bifurcation theory, asymptotic and perturbation methods for our model analysis. Our mathematical models can not only reproduce the experimental data at hand, but also make predictions about the mechanisms underlying chromosome motility in dividing cells.

For my parents.

CONTENTS

ACKNOWLEDGEMENTS

I would like to thank all the people who have helped and inspired me during my doctoral study and who have made this thesis possible.

I especially want to thank my advisor, James Keener, for his guidance during my research and study. His perpetual energy and enthusiasm in research has been a great source of inspiration. I greatly appreciate all his contributions of time, ideas, and funding to make my doctoral study productive and stimulating.

I am thankful to my dissertation committee members, Aaron Fogelson, Paul Bressloff, Jingyi Zhu and Markus Babst, for their guidance and for their time, interest, and helpful comments.

I would like to thank my undergraduate professors, especially Louis Zulli, who showed me the joy of research in mathematics and has been an invaluable mentor and friend through the years.

I gratefully acknowledge the funding sources that made my Ph.D. work possible. I was funded by the National Science Foundation, the Mathematics Department Graduate Teaching Fellowship, and the University of Utah Graduate Research Fellowship.

I am indebted to many current and former student colleagues at Utah for providing a stimulating and fun environment in which to learn and grow. I am especially grateful to: Britt Bannish, Erica Graham, Cheryl Zapata, Chris Reimen, Sean Laverty, Darci Taylor, Karin Leiderman, Lindsay Erickson, and Courtney Davis.

I wish to thank my friends Gozde Ulas, Inku Subedi, and Prince Chidyagwai for helping me get through the difficult times, and for all the emotional support, camaraderie, and caring they provided.

I would like to thank my family for all their love, support, and encouragement. For the presence of my sister Arlinda in Utah. For my husband Jeremy, whose unwavering support and encouragement during the final stages of this Ph.D. is so appreciated. Thank you.

Lastly, and most importantly, I wish to thank my parents, Luljeta and Zamir Shtylla, who are my greatest source of strength and who have supported me in all my pursuits. To them I dedicate this thesis.

CHAPTER 1

INTRODUCTION

In just one minute 300 million cells in the human body die and become immediately replaced. New cells are furnished from existing cells through a process called cell division or mitosis. Proper mitosis progression is extremely important in multicellular organisms since disruptions in cell division can lead to very serious disorders such as cancer. Indeed, cancer in somatic cells can be defined as a disease of mitosis. The development of future vaccines and cancer treatments that target aberrant mitotic cells will require a good understanding of mitotic mechanisms and checkpoints. Advances in technology have allowed for a wealth of experimental data to be collected about cell division, however the mechanisms that drive the observed cellular properties are not clear. A very conspicuous and poorly understood step in mitosis is the movement of chromosomes to specific locations in the cell. In this thesis, we develop and analyze mathematical models which propose mechanisms for how chromosomes move and how biochemical reactions can be used to control this movement in space and time in two model systems: newt lung cells (eukaryotic cells), and *Caulobacter crescendus* bacterial cells (prokaryotic cells). We start in this first chapter by introducing the necessary biological background and experimental data that are going to be important in the development of mathematical models presented in subsequent chapters.

1.1 Chromosome movement in higher eukaryotes

Cell division or mitosis is only one of a few states that a healthy cell can experience as part of its cell cycle. The cell cycle of an eukaryotic cell is made up of three distinct stages: DNA replication, cell growth, and cell division. See Figure 1.1. Due to large energy requirements, cells undergo growth stages such as G1 and G2 before replicating their genetic material in S phase and physically separating DNA for the two daughter cells in M phase or mitosis.

During mitosis, a cell undergoes significant physical changes which are grouped into a sequence of consecutive steps or phases. The stages of mitosis are depicted in Figure 1.2. In prophase, duplicated chromosomes start to condense and an array of fibers (called

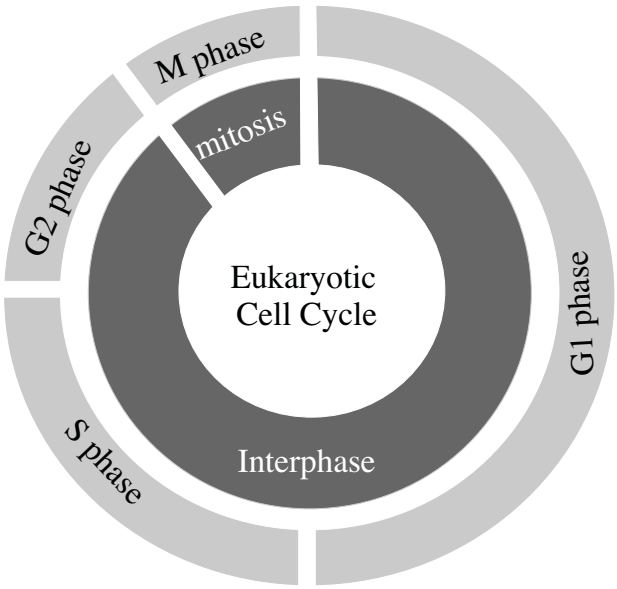

Figure 1.1. A diagram of the eukaryotic cell cycle. A cell undergoes four phases during the cell cycle. In G1 phase cells grow and use a significant amount of nutrients while they prepare to enter the next phase. In S phase new DNA is produced as the cell's current DNA is being copied. In G2 another growth phase takes place and in M phase the cell physically separates into two daughter cells with identical genetic material. G1, G2 and S phase are grouped into interphase, which is where a cell typically spends most of its time. Some cells do not enter G1 phase after mitosis and instead remain in a quiescent state called G0.

microtubules) develops from two structures called centrosomes (or poles). The fibers in a dividing cell form a dense network known as the mitotic spindle. In prometaphase, the nuclear envelope breaks and spindle fibers interact with chromosomes, some attach at specific sites while some push on the chromosome itself. In metaphase, the centrosomes have migrated to the two ends of the cell and chromosomes are being moved by the spindle at the middle of the cell, called the metaphase plate. We will frequently refer to the movement of chromosomes to the metaphase plate as congression. In anaphase, the spindle begins to shorten thereby causing each chromosome half to be pulled in two different directions. Finally, in telophase/cytokinesis, the nuclear envelopes reform and the mitotic spindle starts to disintegrate. In its final step (cytokinesis) the cytoplasm is divided in half with the help of filaments that constrict the mother cell at the metaphase plate. Given the complexity of these stages of mitosis, it is quite striking that a cell can segregate identical copies of DNA to the daughter cells. This precision has intrigued biologists since the late 1800s.

The ability of a cell to precisely split chromosomes into two equal groups for the daughter

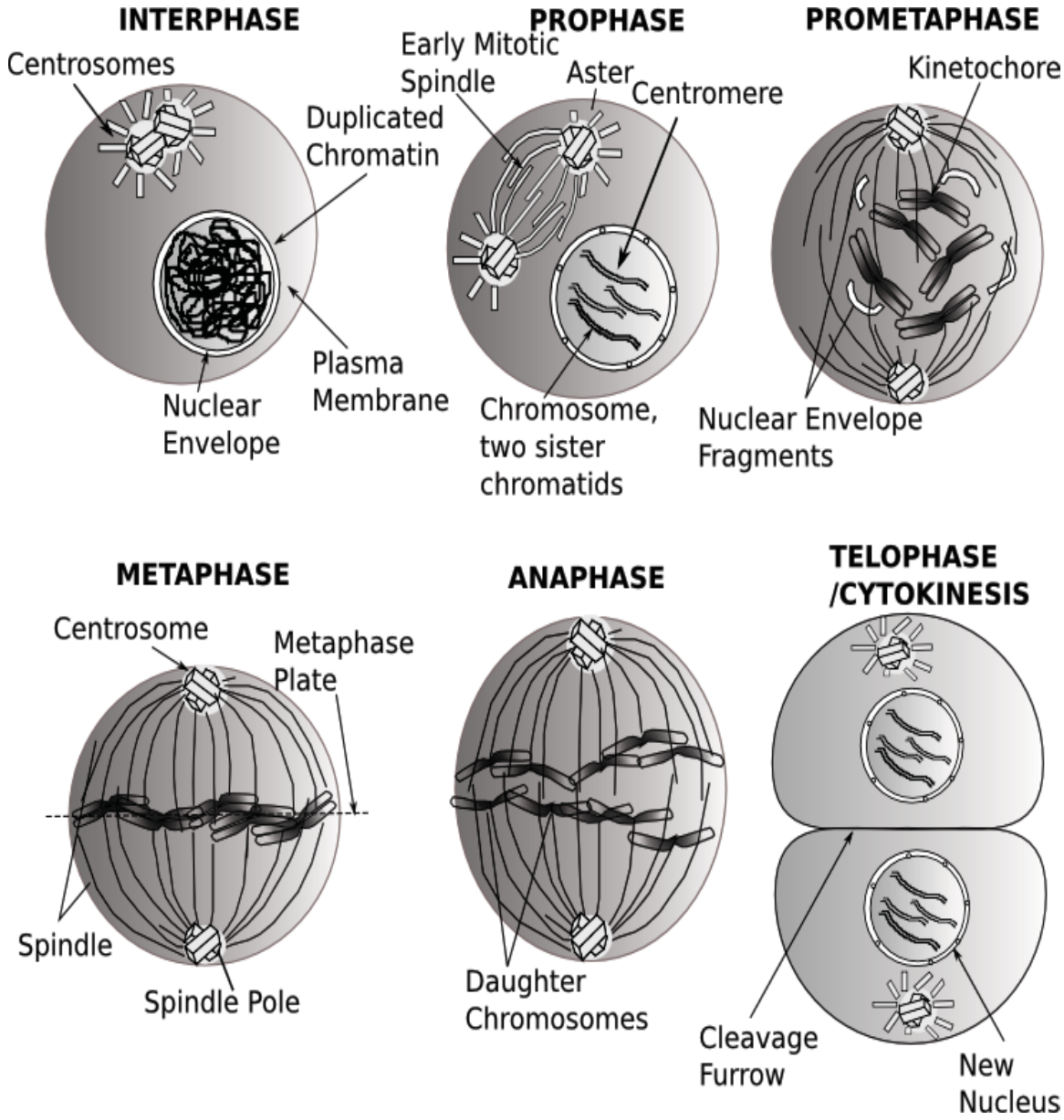

Figure 1.2. A diagram of mitosis stages in animal cells. During interphase, the genetic material has been replicated. In prophase chromosomes are condensed, while a dense network of fibers appears from the centrosomes. In prometaphase, the nuclear envelope breaks down and chromosomes are released in the cell. In the meanwhile, the mitotic spindle fibers have pushed centrosomes to opposite parts of the cell. The fibers start to interact with chromosomes at specific sites called kinetochores. In metaphase, chromosomes are pushed by the fibers at the middle of the cell, or metaphase plate. In anaphase, the fibers pull chromosome arms toward the centrosomes. Finally in telophase and cytokinesis, chromosomes have been moved to opposite sides of the cells and the cytoplasm is pinched in half. The nuclear envelope reforms around the chromosomes.

cells is tightly correlated with the proper movement of chromosomes in the cell. During mitosis, chromosomes have already been replicated and condensed into a two-strand compact structure, as depicted in Figure 1.3. Each of the replicated DNA copies in a chromosome is called a chromatid. The two chromosome chromatids (or sister chromatids) are joined by a structure called centromere. Chromosome movement is very tightly controlled in space and time to ensure that two identical copies of cells result from division. The movement of chromosomes is facilitated by the mitotic spindle network of microtubules, which interacts with and facilitates the movement of chromosomes in the cell. The spindle microtubules can associate and attach to a chromosome with the help of dedicated proteinaceous structures called kinetochores (Kt) [4]. See Figure 1.3.

The mitotic spindle is able to generate the necessary movements of chromosomes due to the dynamic nature of microtubules. A microtubule is a hollow polymer with diameter 25 nm built by $\alpha\beta$ tubulin dimers which are arranged into 13 protofilaments. Since the dimers preserve their orientation, the polymer lattice also inherits polarity; molecular motors use this lattice polarity to establish directionality in their movement while delivering cargo [4]. Microtubules frequently experience a state called dynamic instability, in which polymerizing and rapidly depolymerizing polymers coexist at steady state [4]. When a polymer changes

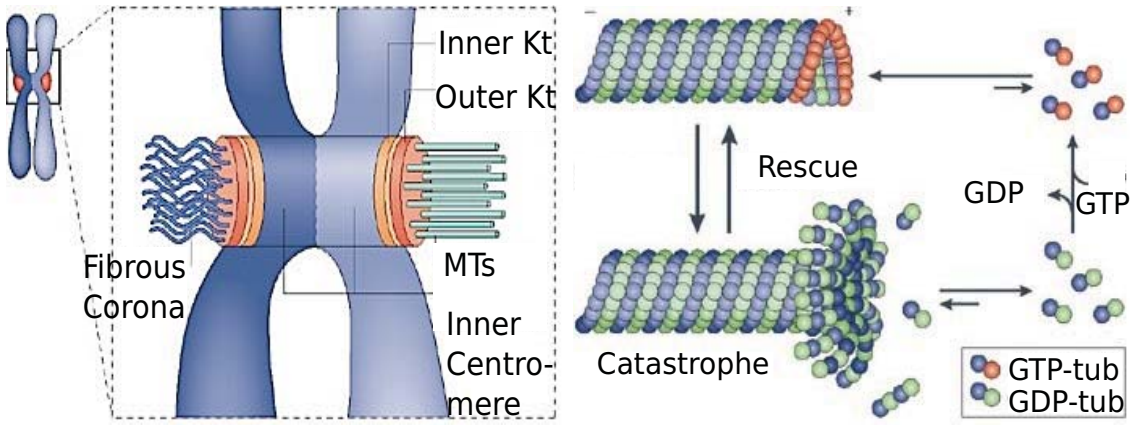

Figure 1.3. A schematic of vertebrate chromosomes and of the dynamic instability of microtubules. A chromosome is attached to mitotic fibers (microtubules) with the help of specific sites called kinetochores. Typically kinetochores can bind multiple microtubules at the same time. In this diagram, only one kinetochore of the chromosome is bound to microtubules while the other kinetochore is unattached. Multiple filamentous proteins are localized at kinetochores as marked by the fibrous corona. Microtubules undergo dynamic instability during mitosis, which is marked by stochastic transitions of the filaments between growth and shrinking states. Adapted by permission from Macmillan Publishers Ltd: Nat. Rev. Mol. Cell Biol. [4], copyright 2008.

from a polymerization to a depolymerization state the event is called a catastrophe; the opposite is a rescue. A diagram of a MT undergoing polymerization/depolymerization is shown in Figure 1.3. Polymerization of GTP hydrolyzed β tubulin locks GTP associated energy into the lattice so that there is a 1000 fold difference in the dissociation of GDP-tubulin at depolymerizing ends relative to GTP-tubulin dissociation at a polymerizing end [4]. Therefore a microtubule retains a polymerizing tip due to the lag between subunit addition and the stabilizing GTP-hydrolysis (stabilizing cap). The cap could be lost either stochastically or by external signals, either of which results in rapid depolymerization. Polymerization and depolymerization of MTs can generate significant forces *in vivo* [4].

In vertebrate cells, chromosome movement has some striking characteristics. Experiments have shown peculiar chromosome movement which is characterized by periods of motion at approximately constant speeds marked by abrupt switches in direction [15][21]. This led to the classification of the behavior as chromosome oscillations or "Directional Instability" [21]. Depending on the state of attachment of a chromosome, we can have a monooriented chromosome, which is attached to microtubules coming only from one pole. Bioriented chromosomes are attached to microtubules emanating from both poles. Both monooriented and bioriented chromosomes experience directional instability. Monooriented chromosome oscillations are highly regular with amplitudes $\approx 2-3$ μm and periods $\approx 2-3$ min [21]. Bioriented chromosomes also display oscillations with amplitudes $\approx 1-3$ μm and periods of $\approx 1-2$ min. While monooriented chromosomes show consistent, very sharp switches in direction ≈ 6 sec, bioriented chromosomes occasionally display phases of no motion which are not seen in monooriented chromosomes [15][21]. After biorientation motion preserves constant velocities with a bias toward the metaphase plate (or spindle equator) controlled by the duration of poleward and antipoleward trips [21].

The cornerstone experiment which quantified chromosome motion in vertebrate cells was conducted by Salmon et al. in [21], where dividing newt lung cells were observed. newt lung cells make an excellent model organism for mitosis observations since they have very large cells with diameters ranging $40-50$ μm, which imposes extended excursions for kinetochores for both congression to the equator and anaphase separation [21]. Furthermore, the cells remain flat and optically clear and motion coming solely from Kt/MT interactions could be discerned [21]. Using high resolution video microscopy and semiautomatic tracking, chromosome motions could be followed for various time intervals in dividing cells. A distance versus time plot for kinetochore movements from [21] is shown in Figure 1.4.

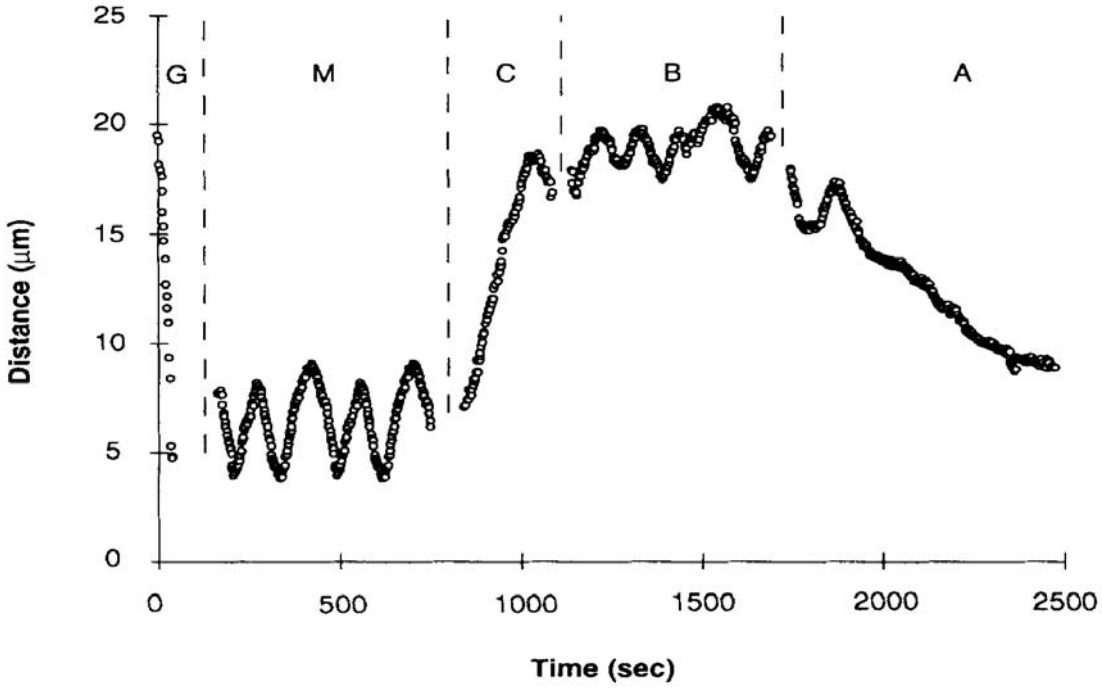

Figure 1.4. Distance versus time plot of typical single kinetochore movements throughout mitosis adapted from [21]. G-phase represents chromosome gliding on ATP dependent molecular motors toward the pole with high load dependent velocities. M-phase represents monooriented state in which typically chromosomes display very sharp changes in direction once close to the pole (in this figure the pole is positioned at $y = 0$). S-phase represents congressing phase in which an attachment on the other kinetochore of a monooriented chromosome is established. One kinetochore becomes the leader and the other is trailing. B-phase represents lower amplitude chromosome oscillations around the equator. At A phase the sister chromatids split and each arm moves separately toward the corresponding pole.

A few important observations were made in [21] which we will refer to later in the thesis:

- Kinetochores abruptly and autonomously change between phases of poleward (P) and anti-poleward (AP) motion which are coupled to the dynamic instability of kinetochore associated microtubule (kMT) plus ends.
- The anti-poleward and poleward trips have constant velocities averaging to $1.7 - 1.8$ μm/min with little variation from prometaphase to anaphase.
- Chromosomes display neutral phases (or confused phase) with bioriented chromosomes having longer neutral phases than monooriented ones. However such phases are usually brief compared to P and AP phases.

- Congression movements are primarily the result of the differences in the duration of P and AP movements and not their velocities.

- Kinetochore poleward movements produce pulling forces on the centromere whereas AP movements produce pushing forces.

Perhaps the most curious prediction from this study had to do with the role of tension in coordinating AP and P trips. High tension across the centromere (high loads on kinetochores) was hypothesized to be the main modulator of P and AP phase switching with high tension (stretch) increasing the probability of AP motion and low tension increasing the probability of P motion [15][21]. This study points to a possible mechanism by which tension and kMT tip dynamics (i.e., poleward and antipoleward movements) can be coordinated. In order to better understand the above described behavior one needs to not only take a closer look at what could be generating P and AP motion at the kinetochores, but also how tension could be communicated to the chemical species localized there to generate the observed chromosomal motions. Accordingly, in the next section we discuss some key kinetochore components.

1.1.1 Molecular composition of kinetochores

Chromosome motion imposes difficult tasks on vertebrate kinetochores. On the one hand, the Kt scaffold has to provide microtubule attachment sites robust enough to endure large loads (chromosome). On the other hand, the attachment site should be flexible enough to couple motion to the dynamics of the anchored microtubules. Experiments have shown that kinetochores have three distinct regions: the inner, central and outer kinetochore [4][13]. The inner kinetochore interacts directly with the chromatin, thus connecting the rest of the structure to the chromosome arm. The outer kinetochore is a $50-60$ nm region that provides a location where spindle microtubules can interact with the chromosome [4]. Finally, the central kinetochore contains linker complexes that connect the inner with the outer kinetochore. For the remainder of this section we will review the most recent data on kinetochore proteins which are implicated in chromosome motility.

In order for a microtubule to attach, kinetochores need to be equipped with microtubule attachment sites. The structure for such sites is provided by the KMN network, which contains two important complexes: Ndc80 and KNL-1 [4], as depicted in Figure 1.5. Initial studies showed that Ndc80 was vital to the ability of the kinetochore to form stable microtubule attachments, however it was not clear whether this complex interacted with

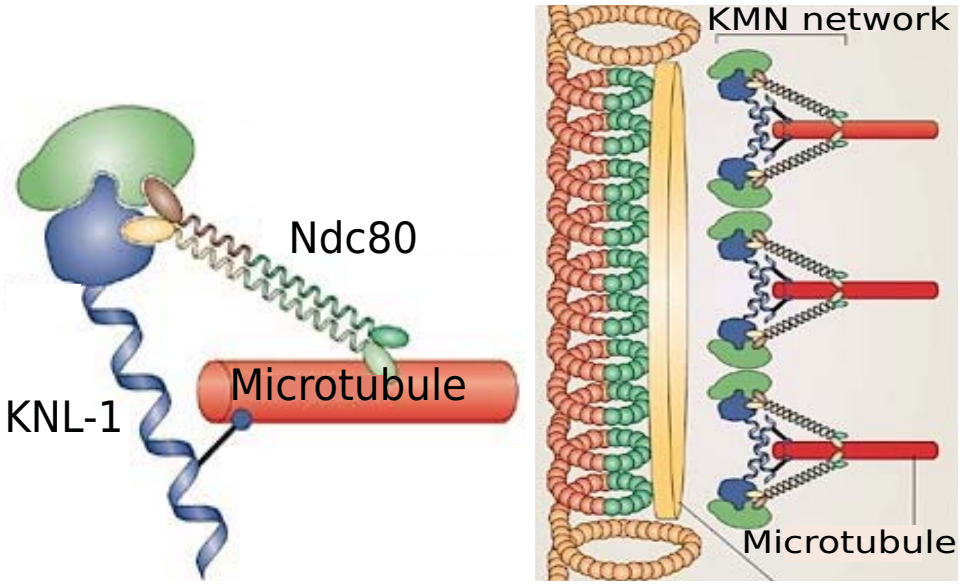

Figure 1.5. A diagram of the KMN network at kinetochores. The KMN network located at kinetochores provides a site for Kt/MT interaction. The network is composed of fibrous proteins Ndc80 and KNL-1 which bind the microtubule lattice. Multiple KMN binding sites are arranged on a kinetochore to support multiple Kt/MT interactions. Adapted by permission from Macmillan Publishers Ltd: Nat. Rev. Mol. Cell Biol. [17], copyright 2007.

microtubules directly [13]. Indeed, recent experiments have shown that Ndc80 has a rod-like structure $\approx$ 50 nm with globular heads at each end, one of which has high a affinity for the inner kinetochore, and the other binds microtubules directly [4][8][24] (see Figure 1.5). Ndc80 interacts with the microtubule lattice through weak electrostatic interactions [6]. Furthermore, at higher concentrations the Ndc80 complexes display cooperativity in binding to the microtubule lattice [3][5][6][8]. KNL1 also binds directly to microtubules and shows cooperativity in binding [3]. The Ndc80 complex binding affinity to microtubules is synergistically increased when in complex with KLN-1 [4]. Current models place the microtubule binding complexes into an array which contains several weak sites that make multiple contacts with microtubules [4]. The proposed arrangement of kinetochore binding sites is shown in Figure 1.5. Therefore the experimental data points to multiple fibrous structures that allow for attachments flexible enough to support microtubule dynamics without letting go.

Microtubules that are bound to Kts have been shown to have stabilized tips *in vitro*, however it had been observed that under certain circumstances kinetochores can instead promote microtubule dynamics [13]. Recent experiments have shed light into the different

proteins located at the kinetochore that can alter microtubule dynamics. The kinesin-13 family member, MCAK is the most powerful microtubule destabilizing enzyme known to date [9]. MCAK is found throughout the cell but it is particularly concentrated at kinetochores, centromeres and spindle poles [11]. There are two main models for MCAK roles at the kinetochores: 1) The first model widely implicates MCAK in the correction of meteoric attachments during cell division [11], 2) The second model proposes MCAK as a direct regulator of chromosome motion by affecting local kMT tip rates. To this end a recent study in [25], used mutants and chimeras of MCAK designed so that they would specifically target kinetochores to study possible mechanistic roles of this kinesin. Using live imaging, the experiments showed that depletion of centromeric MCAK considerably decreases sister kinetochore coordination which decreases speed and increases intra-kinetochore tension [25]. This group proposes that MCAK is not solely specialized for error correction, instead MCAK could enhance motility and coordination of sister kinetochores, with error correction a corollary of these main tasks since erroneous attachments slow down congression. Indeed, [12] earlier reported that depletion of centromeric MCAK leads to delayed congression, alignment defects and severe missegregation. At any rate, the precise role of this protein in chromosome motion or other mitotic events is not well known; it is certainly puzzling that cells place such a powerful destabilizing agent at a site where attachment maintenance is of vital importance.

Given its powerful depolymerizing action, MCAK activity requires tight control from the cell. Aurora B kinase, a regulator of chromosome movement and microtubule dynamics regulates via phosphorylation both the localization of MCAK at the centromere, as well as its depolymerase activity (phosphorylated MCAK is inactive) [1][2][25]. Aurora B kinase is found in a complex with INCENP, survivin and borealin (Chromosomal Passenger Complex -CPC) [17], Figure 1.6. Of these complex components Aurora B kinase is the only enzymatic protein with the rest of the members regulating the activity and stability of Aurora B. Just like Aurora B, the complex is localized at centromeres. INCENP binding activates Aurora B, in turn Aurora B phosphorylates INCENP which further activates the kinase in a positive feedback loop [17].

The CPC complex is proposed to be involved in tension sensing at kinetochores. First, in an Aurora B regulation study by [2], a model was proposed for force dependent kinase activation. The model speculated that force could affect the morphology of the complex by separating Survivin and Aurora B and physically blocking their interactions. Such a

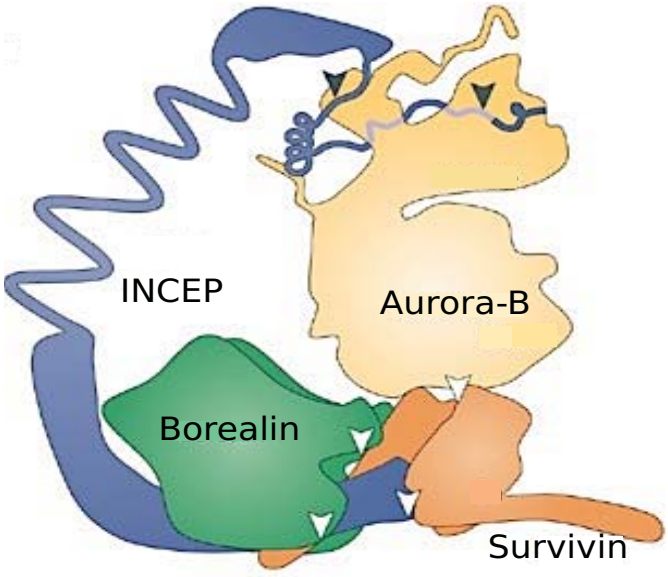

Figure 1.6. A diagram for the CPC complex. Aurora B kinase activity is regulated by the rest of the components of the complex. The complex is implicated in tension sensing, since an increased physical distance between the components affect the regulation of Aurora B action. Adapted by permission from Macmillan Publishers Ltd: Nat. Rev. Mol. Cell Biol. [17], copyright 2007.

mechanism would predict different levels of activated Aurora B for different forces applied to the complex. However, in order for this force-dependent activation to be useful, CPC needs to be in contact with centromere components that undergo physical stretch. A study by [18] in budding yeast revealed a possible role of CPC in a tension detecting mechanism at kinetochores. It was already known that ICENP can bind microtubules, however the study confirmed Survivin association with a kinetochore component (CBF3), therefore the complex could be placed as a linker between kinetochores and microtubules and change activation state upon stretch-dependent events. Therefore, we can envision a situation where CPC acts as a localized tension sensor at the kinetochore, which in turn affects Aurora B activation and subsequently MCAK activity, see Figure 1.7. To our knowledge this is the most direct connecting path between mechanical forces and kinetochore chemical reactions. We will build upon these interactions when formulating our mitotic chromosomal movement model in Chapter 3.

Finally, many other proteins that affect kMT tip dynamics localize at kinetochores, as depicted in Figure 1.7. Cytoplasmic linker proteins (CLIP), cytoplasmic associating proteins (CLASP), MAP215 are proteins which are implicated in promoting polymerization

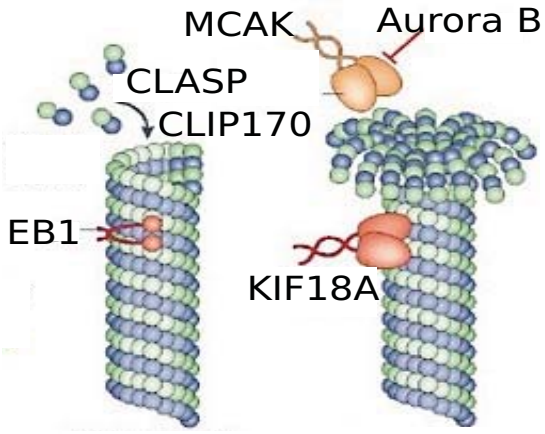

Figure 1.7. Kinetochore associated proteins. A variety of proteins which affect microtubule dynamics localize at kinetochores. MCAK and KIF18A cause MTs to depolymerize whereas CLIP, CLASP, MAP and EB1 promote polymerization. Adapted by permission from Macmillan Publishers Ltd: Nat. Rev. Mol. Cell Biol. [4], copyright 2008.

at kinetochores [4]. EB1 has been shown to bind and stabilize microtubule lattice seams, kinesin-8 (KiF18A) has been identified to have both motor and depolymerizing activities (MCAK is not motile) [4]. In conclusion, kinetochores are not only equipped with binding structures for kMTs, but they also recruit many proteins which directly affect kMT tip dynamics. The interactions between all these components produces the motions observed in experiments.

Movements of chromosomes with multiple kMT attachments are arguably one of the most difficult phenomena to understand mechanistically [7]. The first generation of theoretical models only focus on modeling mechanical and kinetic effects due to the availability of data. However, kinetochores contain many proteins which are part of mitotic regulatory pathways and affect kMT kinetic rates; the effects that these pathways can have on motion are not well known. Modeling can be useful when information is incomplete. In Chapters 2 and 3, we develop and analyze mathematical models which describe various aspects of chromosome motion in higher eukaryotes. Our model organisms are newt lung cells, and we use data from [21] in order to construct our models. We take a two step approach to modeling chromosome movement in higher eukaryotes. First, in Chapter 2, we formulate a model for kinetochore/kMT coupling which allows us to make predictions about the relationship between velocities and loads. Then in Chapter 3, we integrate our chromosome motor model into a negative feedback mechanism that relates localized chemical reactions

with force dependent spatial cues. We use our models to answer three important questions: 1) How can very unstable polymers (microtubules) carry large loads (chromosomes) at constant velocities over significant distances? 2) Why and how does directional instability take place? 3) How is congression achieved and how do chemical signals affect anaphase division? Given the large number of proteins involved in the process as well as the small size of kinetochores, mathematical modeling can help in sorting out the important factors that contribute to the characteristic well observed mechanical events.

1.2 Chromosome segregation in bacteria

Bacteria are among the most widespread organisms on Earth. A key factor for survival in these systems is the selection for fast reproduction rates, which has led to highly streamlined architectures and small genomes [22]. Due to their perceived simplicity, bacteria have been long thought to be in a primitive cell state, whereby many of the features seen in eukaryotic cells simply did not exist. Recent technological advances have given us a window into the structural details of bacterial cells and the resulting observations contradict long-held beliefs. More specifically, many complex processes in bacterial cells, such as cell division, have been shown to be regulated by dedicated mechanisms, which are comprised of dynamic cytoskeletal elements, much like in eukaryotic cells. For the remainder of this chapter, we give an overview of the experimental data available for chromosome segregation in *Caulobacter crescendus*.

C. crescendus is a gram-negative bacterium. Like in many other bacterial cells, the large genome of *C. crescentus* is packed into a circular chromosome, see Figure 1.8. It was initially thought that the chromosomal DNA in *C. crescendus* was randomly spread throughout the cell. However, closer analysis of data revealed that chromosomes in this cell followed specific patterns. More specifically, as depicted in Figure 1.8, the origin of replication (ori) in a chromosome is always found at the flagellated pole and the terminus (ter) is located at the opposite end of the cell [22]. Given the specific orientation of chromosomes in these cells, it is clear that the bacterium has to ensure that chromosome location in the cell is preserved throughout its life-cycle.

Experimental studies have shown that the specific localization of chromosomal sites in *C. crescendus* is established while the bacterium segregates its DNA during division. A diagram of the *C. crescendus* life cycle is shown in Figure 1.9. In the course of its life cycle, *C. crescendus* transitions from a flagellated swarmer cell into an immobile stalked cell. The division of this bacterium cell is asymmetric. Out of the two daughter cells, only the stalked

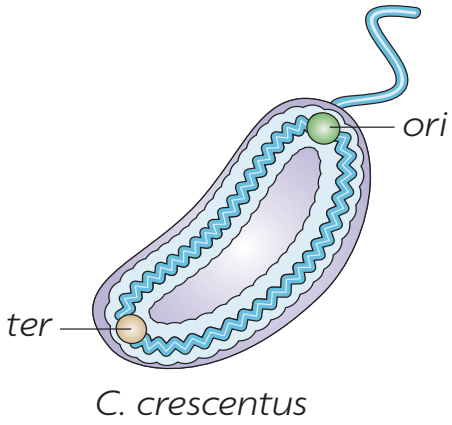

Figure 1.8. *C. crescendus* chromosome. The circular chromosome is oriented so that the ori is located by the flagellum and the ter is located at the opposite side. Reprinted by permission from Macmillan Publishers Ltd: Nat. Rev. Microbiol. [22], copyright 2008.

cell can immediately enter division, whereas the flagellated cell has to wait for another cycle of division. Interestingly, the flagellum is shed during the swarmer to stalk transition and it always reappears on the other pole, opposite to the stalk.

During the asymmetric division of this bacterial cell, the circular chromosome undergoes a sequence of tightly controlled movements that result into two identical chromosome copies for the daughter cells. Next, we discuss the machinery that mediates chromosome movement in *C. crescendus*.

1.2.1 Mitotic apparatus of *C. crescendus*

Before replication is initiated, the mother cell ori of *C. crescendus* is anchored to the membrane in a region we refer to as the old pole, as depicted in Figure 1.9. After replication is initiated, one copy of the chromosome moves from the old mother cell pole to the new cell pole traversing the whole length of the cell in a matter of minutes. While this movement is taking place, the other chromosome copy remains steadily anchored to the old pole. In *C. crescendus*, chromosome segregation is unidirectional (i.e., no oscillations in wild type cells). Because chromosome movement in this bacterial system is taking place while the chromosome is being replicated, it was not clear whether the replication fork or if the membrane of the growing cell were involved in the movement of the chromosome. However, the observed chromosome segregation velocities were much too rapid to be accounted for by passive transport, and furthermore other chromosome regions (such as ParB in Figure

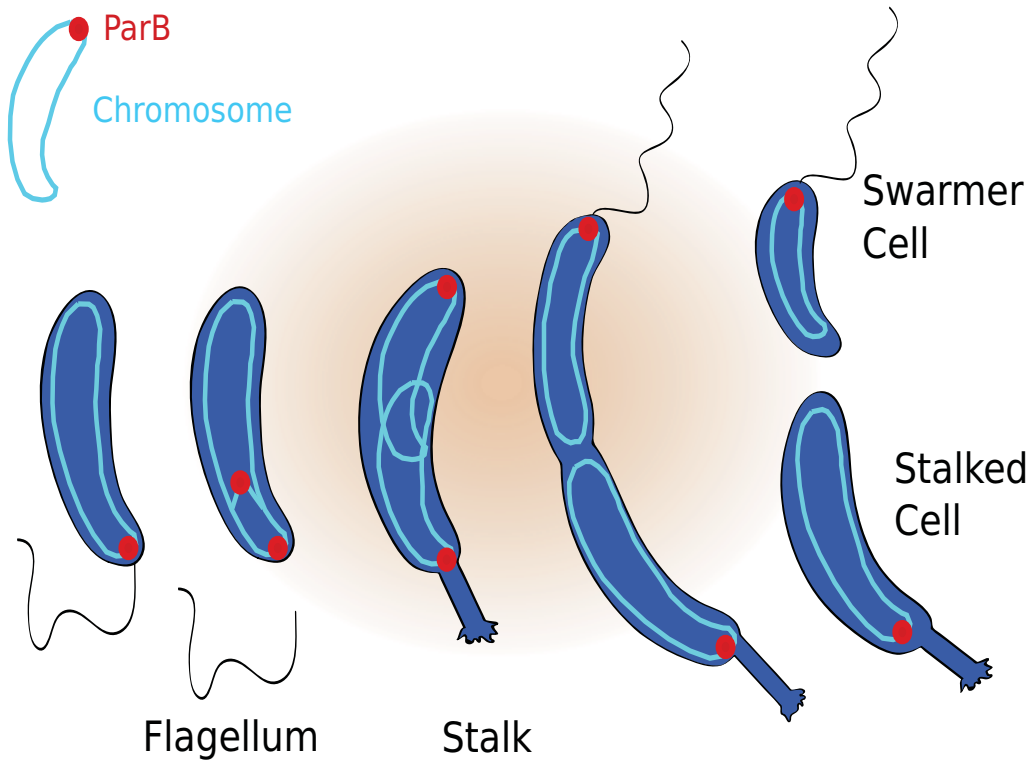

Figure 1.9. *C. crescendus* life cycle. *C. crescendus* differentiates from a mobile flagellated swarm cell to a sessile stalked cell. The stalked cell undergoes asymmetric division which results into a new stalked cell and a flagellated swarmer cell. Only the stalked cell can immediately enter another round of cell division. The swarmer cell has to develop into a stalked cell before it can divide again.

1.9) always reached the new pole faster than ori, indicating that the replication fork was does not generate a pulling force [23].

Experimental evidence suggests that an active mechanism mediates the movement of the chromosome copy in *C. crescendus*. The type I DNA partitioning system is believed to drive segregation in these bacterial cells. There are three components to this system: 1) ParA, an ATPase, 2) parS, a centromere-like site that localizes close to the origin of replication of the chromosome, and 3) ParB, a mediator protein which binds parS and also regulates ParA activity [14]. The ParAB system has been shown to be required for the proper movement of chromosomes in various bacterial cells [22]. ParB binds parS and spreads along the chromosome, forming a large nucleoprotein complex similar to kinetochores in eukaryotes. ParA proteins are Walker-type ATPases. A ParA protein will bind ATP and then dimerizes

with another ATP-bound ParA. ATP-bound ParA dimers have been shown to interact with ParB directly [14]. On the other hand, ParB stimulates the ATPase activity of ParA dimers which results in the release of ParA monomers. In experiments, ParB is observed to move from the old pole to the new pole, while the chromosome copy follows [14][19].

ParA proteins form dynamic cloud-like structures in dividing *C. crescendus* cells [19]. Further, *in vitro* experiments with purified ParA have shown that ParA polymerizes into linear polymers in the presence of ATP [14]. Super-resolution imaging *in vivo* also indicates that ParA is assembled into linear narrow structures oriented along the long axis of dividing cells. Taken together, the experimental data seem to suggest that ParA clouds are composed of linear polymers that are laterally bundled with one another [14]. Thus, a dynamic picture for ParA/ParB proteins seems to emerge in this bacterium. ParA binds ATP and creates dimers that are added to ParA polymers. If ParB comes in contact with ParA polymers, it will bind and also stimulate the ATPase activity of ParA, causing ParA to depolymerize. Indeed, experimental observations have shown a correlation between ParB movement and a retracting cloud of ParA during chromosome segregation [14][19]. Images of chromosome movement marked by ParB location *in vivo*, taken from [14], are shown in Figure 1.10.

In vivo observation of dividing cells, as depicted in Figure 1.10, indicates that initially a ParA bundle of filaments extends from the new pole to the old pole near parS/ParB. Contact between ParB and the ParA structure results in the shrinking of the ParA bundle

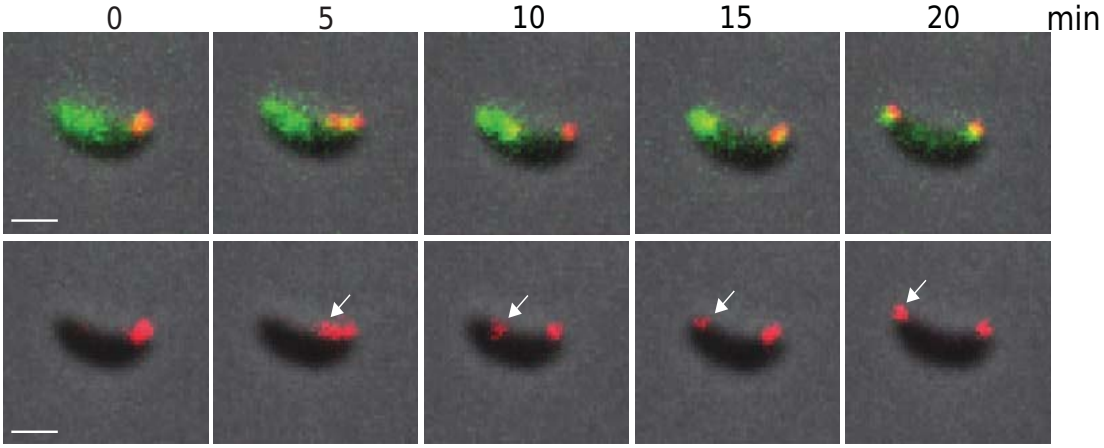

Figure 1.10. ParA and ParB dynamics *in vivo*. Time-lapse epifluorescence microscopy of *C. crescendus* cells undergoing chromosome segregation. ParA structures (green) lead the ParB complex (red) toward the new pole. Adapted by permission from Macmillan Publishers Ltd: Nat. Cell Biol. [14], copyright 2010.

toward the new pole. ParA bundle shrinking is accompanied with the translocation of parS/ParB, creating what is referred to as a "pulling" mechanism. After ParB has reached the new pole, the ParA structure reorganizes and it reappears along the entire length of the cell. The underlying mechanisms that drive this supposed pulling motion in the ParAB system are not well understood.

Even though ParA and ParB together are sufficient to generate motion of the chromosome in *C. crescendus*, the unidirectionality of segregation seems to be controlled by additional proteins. *C. crescendus* cells are highly polarized since during division a bacterium develops both a flagellum and a stalk at opposite ends. The protein TipN localizes at the new pole in dividing cells, where it ensures that new pole markers such as the flagellum are properly localized [19]. Surprisingly, TipN can affect the movement of ParB even though it remains bound to the new pole membrane while the chromosome copies are being segregated. In $\triangle$tipN cells ParB motion was found to experience frequent pauses along with reversals in direction, as opposed to the unidirectional movement of ParB for wild-type cells [19]. In cells depleted of TipN, ParA structures appear between the ParB complex and the old pole, indicating that ParA localization is related to TipN action. Further, in contrast to wild type cells, which show an accumulation of ParA protein at the new pole, $\triangle$tipN cells do not display new-pole ParA accumulation. Experiments in [14] have shown that ParA monomers can directly interact with TipN. Thus, erratic segregation could result due to poor ParA monomer localization in the cell when TipN is removed. In Figure 1.11 are shown images of chromosome segregation in $\triangle$tipN cells.

Given the experimental evidence, it is postulated that TipN is part of a segregation regulatory mechanism. It is not clear from experiments, however, how TipN could control ParA monomer concentration in the cell. There are two theories in the literature: 1) TipN might nucleate or stabilize ParA structures at the new pole [14], 2) TipN simply provides a binding site at the new pole that increases the local concentration and biases the insertion of ParA molecules into the bundle at the pole [19]. Mathematical modeling can help test the viability of these two proposed mechanisms.

The control of ParA dynamics in *C. crescendus* cells seems to be key to the control of chromosome movement. Besides TipN, there is one other protein which is implicated in ParA monomer sequestration. PopZ is a protein that assembles into a matrix at both cell poles [19], and it has been shown to anchor ParB at the new pole after segregation in order to prevent backward movement of the complex. However, in addition PopZ can directly interact with ParA monomers and is thought to accumulate ParA monomer at the

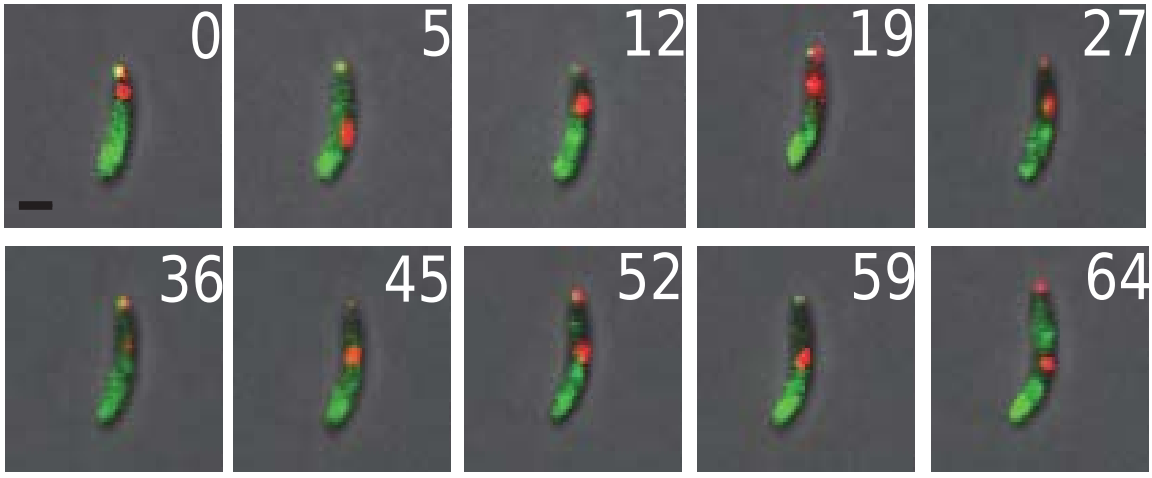

Figure 1.11. ParA and ParB dynamics in △tipN cells. Time-lapse epifluorescence microscopy of *C. crescendus* cells undergoing chromosome segregation, images are captured every several min as indicated in the figure panels. ParA structures (green) appear between ParB (red) and the old pole. ParB fails to segregate unidirectionally. Adapted by permission from Macmillan Publishers Ltd: Nat. Cell Biol. [14], copyright 2010.

old cell pole when TipN is depleted [19]. In many △tipN cells, ParA monomers are shown to slowly accumulate at the old pole as ParB slowly and erratically moves toward the new pole; simultaneously large ParA filaments appear between ParB and the old pole [14][19]. Based on the current working model, PopZ works similarly to TipN to somehow control ParA monomer concentrations in the cytoplasm. The similar action of PopZ and TipN is reinforced by experimental data from △popZ cells, which show that when TipN is depleted from these cells, ParB completely fails to segregate to the new pole. So a double deletion in these pole proteins seems to remove all polar sequestration mechanisms for ParA and a subsequent loss of ParB movement toward the new pole. All in all, the deletion experiments seem to indicate that TipN is a necessary protein for unidirectional chromosome movement, and that if ParA bundle dynamics are not carefully managed, proper chromosome movement is lost. We remark that the biochemical control of chromosome movement in *C. crescendus* is almost identical to the tight control of chromosome movement in higher eukaryotes via MT rate altering enzymes at kinetochores.

We conclude our discussion about the mitotic apparatus of *C. crescendus* by returning to the ParA polymerization dynamics. A variety of Par family proteins form dynamic scaffolds in bacterial cells. The best studied one is the network of ParM polymers which

works in *E. coli* to segregate plasmids. *In vitro*, ParM forms polymers in an ATP dependent fashion, similarly to F-actin. However, ParM assembly dynamics are distinct from what is seen in actin in a couple of ways. First, ParM polymers are not polar and elongate in either direction and also the nucleation of polymers is rapid and spontaneous [22]. Second, instead of treadmilling, ParM polymers constantly transition between states of rapid growth and disassembly, similar to the dynamic instability observed in eukaryotic MTs. The same dynamic instability property has been observed in ParA filaments in *T. thermophilus* [16]. Thus, it is expected that the same dynamic properties seen for ParM filaments work for ParA filaments in *C. crescendus*.

The interaction of ParM filaments with ParR is also of great interest in the context of the ParAB system. In *E. coli* ParR is attached to plasmids and works in the opposite fashion to ParB by stabilizing ParM filaments. Biochemical and EM experiments have shown that ParR wraps around or encircles the ends of elongating ParM filaments in a similar way to kinetochore protein arrangement around kMTs [10]. A diagram for the model of ParR/ParM interactions is shown in Figure 1.12. These interactions indicate that the Par apparatus in bacterial systems has many similarities with the mitotic apparatus used in higher eukaryotes.

There is a wide variety of biological models that are proposed for how a segregating

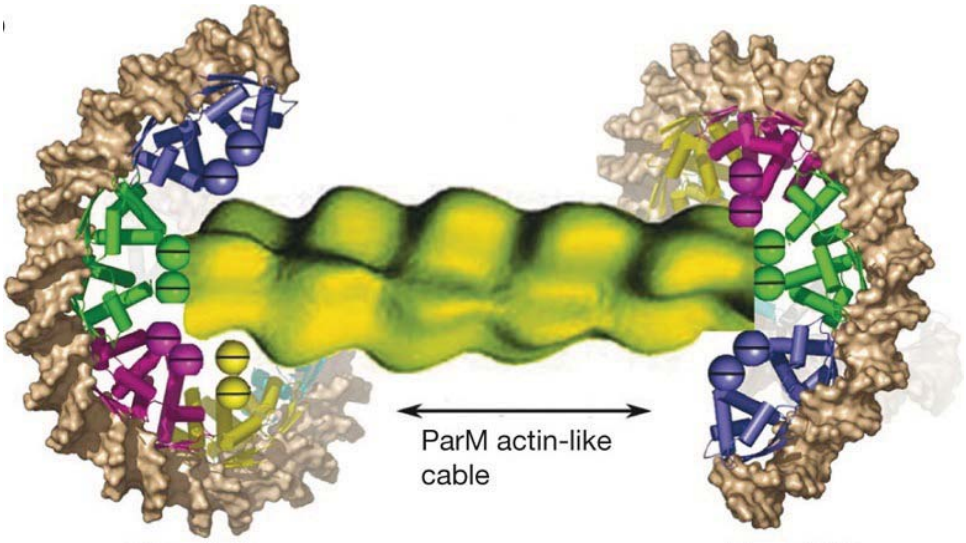

Figure 1.12. ParR interaction with ParM filaments. DNA is colored brown and ParM yellow. The ParR molecules are shown in magenta, green, blue and yellow, and cyan. Figure reprinted by permission from MacMillan Publishers Ltd: Nature [20], copyright 2007.

chromosome moves in the *C. crescendus* cell, however the molecular mechanisms that mediate the ParAB-mediated chromosome movement are not well understood. In this respect mathematical modeling can make a contribution to our understanding of chromosome motility by quantitatively assessing the various mechanisms that could be at work in these cells. In light of the experimental evidence, there are two questions that are of interest and which we can address with mathematical modeling: 1) What is the molecular mechanisms by which a ParA bundle pulls on ParB, and how do ParA dynamics affect ParB movement? 2) What is the role of ParA monomer regulatory proteins such as TipN in the control of chromosome segregation? We address these questions in Chapter 4 by developing mathematical models for chromosome segregation in *C. crescendus*.

1.3 References

[1] P. P. Andrews, Y. Ovechkina, N. Morrice, M. Wagenbach, K. Duncan, L. Wordeman, and J. R. Swedlow, *Aurora B regulates MCAK at the mitotic centromere*, Dev. Cell, 6 (2004), pp. 253–268.

[2] M. A. Bolton, W. Lan, S. E. Powers, M. L. McCleland, J. Kuang, and P. T. Stukenberg, *Aurora B kinase exists in a complex with survivin and INCENP and its kinase activity is stimulated by survivin binding and phosphorylation*, Mol. Biol. Cell, 12 (2002), pp. 3064–3077.

[3] I. M. Cheeseman and A. Desai, *The conserved KMN network constitutes the core microtubule-binding site of the kinetochore*, Cell, 127 (2006), pp. 983–997.

[4] ——, *Molecular architecture of the kinetochore-microtubule interface*, Nat. Rev. Mol. Cell Biol., 9 (2008), pp. 33–46.

[5] C. Ciferri, A. Musacchio, and A. Petrovic, *The Ndc80 complex: hub of kinetochore activity*, FEBS Lett., 581 (2007), pp. 2862–2869.

[6] C. Ciferri, S. Pasqualato, E. Screpanti, G. Varetti, S. Santaguida, G. D. Reis, A. Maiolica, J. Polka, J. G. D. Luca, P. D. Wulf, M. Salek, J. Rappsilber, C. A. Moores, E. D. Salmon, and A. Musacchio, *Implications for kinetochore microtubule attachment from the structure of and engineered Ndc80 complex*, Cell, 133 (2008), pp. 427–439.

[7] G. Civelekoglu-Scholey, D. J. Sharp, A. Mogilner, and J. M. Scholey, *Model of chromosome motility in drosophila embryos: adaption of general mechanism for rapid mitosis*, Biophys J., 90 (2006), pp. 3966–3982.

[8] M. Emanuele, D. J. Burke, and T. Stukenberg, *A hec of a mictotubule attachment*, Nat. Struct. Mol. Biol., 14 (2007), pp. 11–13.

[9] S. C. Ems-McClung, K. M. Hertzer, X. Zhang, M. W. Miller, and C. Walczak, *The interplay of the N- and C-terminal domains of MCAK control microtubule depolymerization activity and spindle assembly*, Mol. Biol. Cell, 18 (2007), pp. 282–294.

[10] K. Gerdes, M. Howard, and F. Szardenings, *Pushing and pulling in prokaryotic DNA segregation*, Cell, 141 (2010), pp. 927–942.

[11] G. J. Gorbsky, *Mitosis: MCAK under the aura of Aurora B*, Curr. Biol., 14 (2004), pp. 346–348.

[12] S. L. Kline-Smith, A. Khodjakov, P. Hergert, and C. Walczak, *Depletion of centromeric MCAK leads to chromosome congression and segregation defects due to improper kinetochore attachments*, Mol. Biol. Cell, 15 (2004), pp. 1146–1159.

[13] H. Maiato, J. DeLuca, E. D. Salmon, and W. C. Earnshaw, *The dynamic kinetochore-microtubule interface*, J. Cell Sci., 117 (2004), pp. 5461–5477.

[14] J. L. Ptacin, S. F. Lee, E. C. Garner, E. Toro, M. Eckart, L. R. Comolli, W. E. Moerner, and L. Shapiro, *A spindle-like apparatus guides bacterial chromosome segregation*, Nat. Cell Biol., 12 (2010), pp. 791–798.

[15] C. L. Rieder and E. D. Salmon, *Motile kinetochores and polar ejection forces dictate chromosome position on the vertebrate mitotic spindle*, J. Cell Biol., 124 (1994), pp. 223–233.

[16] S. Ringgaard, J. van Zon, M. Howard, and K. Gerdes, *Movement and eqipositioning of plasmids by ParA filament disassembly*, Proc. Natl. Acad. Sci. USA, 106 (2010), pp. 19369–19374.

[17] S. Ruchaud, M. Carmena, and W. C. Earnshaw, *Chromosomal passengers: conducting cell division*, Nat. Rev. Mol. Cell Biol., 8 (2007), pp. 798–812.

[18] S. Sandall, F. Severin, I. X. McLeod, J. R. Y. III, K. Oegema, A. Hyman, and A. Desai, *A Bir1-Sli15 complex connects centromeres to microtubules and is required to sense kinetochore tension*, Cell, 127 (2006), pp. 1179–1191.

[19] W. B. Schofield, H. C. Lim, and C. Jacobs-Wagner, *Cell cycle coordination and regulation of bacterial chromosome segregation dynamics by polarly localized proteins*, EMBO J., 29 (2010), pp. 3068–3081.

[20] M. A. Schumacher, T. C. Glover, A. J. Brzoska, S. O. Jensen, T. D. Dunham, R. A. Skurray, and N. Firth, *Segrosome structure revealed by a complex of ParR with centromere DNA*, Nature, 450 (2007), pp. 1268–1271.

[21] R. V. Skibbens, V. P. Skeen, and E. D. Salmon, *Directional instability of kinetochore motility during chromosome congression and segregation in mitotic newt lung cells: a push pull mechanism*, J. Cell Biol., 122 (1993), pp. 859–875.

[22] M. Thanbichler and L. Shapiro, *Getting organized-how bacterial cells move proteins and DNA*, Nat. Rev. Microbiol., 6 (2008), pp. 28–40.

[23] E. Toro, S.-H. Hong, H. H. McAdams, and L. Shapiro, *Caulobacter requires a dedicated mechanism to initiate chromosome segregation*, Proc. Nat. Acad. Sci. USA, 105 (2008), pp. 15435–15440.

[24] R. R. Wei, J. Al-Bassam, and S. C. Harrison, *The Ndc80/HEC1 complex is a contact point for kinetochore-microtubule attachment*, Nat. Struct. Mol. Biol., 14 (2007), pp. 54–58.

[25] L. Wordeman, M. Wagenbach, and G. von Dassow, *MCAK facilitates chromosome movement by promoting kinetochore microtubule turnover*, J. Cell Biol., 179 (2007), pp. 869–879.

CHAPTER 2

KINETOCHORE MOTORS

In this chapter, we construct and analyze a mathematical model for kinetochore motors operating at the chromosome/microtubule interface. Motor dynamics are modeled using a jump-diffusion process that incorporates biased diffusion due to the binding of microtubules by kinetochore binder elements and thermal ratchet forces that arise when the polymer grows against the kinetochore plate. The resulting force-velocity relations are nonlinear and depend on the strength of microtubule binding at kinetochores, as well as the spatial distribution of binders and of microtubule rate altering enzymes inside the kinetochore. In the case when kinetochore binders are weakly bound and spaced with the same period as the microtubule binding sites, the numerical results for the motor force-velocity relation and breaking loads are in complete agreement with our approximate analytic solutions. We show that in this limit motor velocity depends directly on the balance of polymer tip polymerization/depolymerization rates and is fairly insensitive to load variations. In the strong binding regime, the motor can support attachment for large kinetochore loads but responds with smaller velocities, independent of the polymer tip dynamics. When the kinetochore binders are redistributed with spacing off-register from the microtubule lattice period, our numerics match our analytical velocity results independent of binding strength at kinetochores; motor velocities do not decrease in response to binding strength variation in this case.

2.1 Introduction

Molecular motor enzymes that harvest the chemical energy of ATP hydrolysis to move unidirectionally are used in various cellular processes. However, cells sometimes make use of mechanisms for motion that do not involve ATP-dependent molecular motors. Cellular protrusions such as filopodia and lamellipodia, for example, do not appear to involve molecular motors but instead use thermal ratchets in conjunction with dynamic polymers to generate motion [13]. Another example comes from mitosis, where chromosomes move by tethering to the dynamic tips of microtubules (MT) in an ATP-independent fashion [1][4].

The mechanisms underlying this dynamic coupling of chromosome movement to attached polymerizing/depolymerizing MTs is not well understood.

A chromosome moves by attaching to microtubule plus ends with the help of specialized macromolecular complexes called kinetochores. For each chromosome arm, a single kinetochore (Kt) complex that can bind either one or several microtubules at once is assembled on the chromatid. Microtubules are hollow cylindrical structures that contain 13 linear protofilaments composed of α-β tubulin dimers. During mitosis microtubules stochastically transition between growth and shortening states both when they are attached (kMT) or not attached to a kinetochore [1]. For a polymerizing MT, GTP-tubulin is added at the growing end; these dimers have a preferred flat orientation relative to the polymer lattice. Subsequently, GTP-tubulin is hydrolyzed with some time delay into GDP-tubulin, which prefers a bent conformation. Inside the lattice, lateral tubulin interactions hold the monomers in a straight conformation with the energy of hydrolysis stored as strain. When the lateral interactions are lost, the strain is released so that the ends of depolymerizing MT protofilaments bend and the MT tips become gently flared.

Two important motility characteristics of chromosome movement have been observed experimentally. First, chromosome movement has been shown to be coupled to the polymerization/depolymerization state of an inserted microtubule [10] with velocities dependent on the balance of kMT tip polymerization/depolymerization rates. Second, kinetochores that are attached to a spindle pole by tethering to a kMT display toward and away motion with similar speeds [16] indicating that kinetochore motors are fairly insensitive to variations in load.

Several theoretical models that propose various force-generation mechanisms at kinetochores have been put forward. These models can be separated into two distinct classes: 1) biased diffusion models, and 2) forced walk models. Each model uses variations in kinetochore motor (coupler) geometry and size to convert the energy of Kt-MT interactions into useful work [6].

The first model for chromosome attachment, initially advanced by Hill [5], uses a biased diffusion mechanism. Hill's model proposes that movement is facilitated by a rigid array (so called "sleeve") of weak binding sites that diffuse on the lattice of a kMT. An increased overlap between the sleeve and the lattice is favorable due to free energy decrease from the attachment of more bonds between the sleeve coupler and the microtubule. As the microtubule shortens, sleeve diffusion relocates the bonds so that overlap is preserved generating poleward motion, i.e., biased diffusion. The key aspects of this model are that it

allows for continuous attachment for both growing and shortening microtubules, and also produces speeds that are fairly insensitive to load, in good agreement with experimental data.

Forced walk models use the force of flaring of depolymerizing MT tips in conjunction with force couplers (such as rings) built to resist protofilament outward bending in order to generate depolymerization-coupled movement [11]. If constructed appropriately, these motors can track depolymerizing tips efficiently. However, attachment cannot be maintained when a polymer transitions into a polymerizing state (with blunt ends), nor do velocities remain constant for varying loads. Therefore, these types of motors fail to capture the full range of chromosome motions seen experimentally.

Recent experiments indicate that binding at kinetochores is weak and that diffusion may play a significant role in movement [14][17]. These results seem to support a biased diffusion mechanism but also provide new data that require a more comprehensive treatment of the biased diffusion mechanism at play. Hill's model uses a discrete Markov chain model to show that attachment can be maintained at steady-state for a kinetochore attached to a slowly depolymerizing tip. This work was extended by [7] to account for polymer growth inside the sleeve. In both cases, the transition rate assumptions are valid only in the high activation barrier limit and model implementation into a larger scale mitosis model requires time consuming numerical simulations. Furthermore, for the biased diffusion models that have been studied thus far there has been no inclusion of polymerization thermal ratchet effects that arise when the inserted kMT grows against the kinetochore plate. Also, to our knowledge, the biased diffusion model has not been studied when there are variations in the spatial distributions of Kt binders on the MT lattice.

The present chapter is aimed at developing a mathematical model for kinetochore motors that incorporates a biased diffusion mechanism but also takes into account several features of kinetochore motors not addressed in previous biased diffusion models. This chapter is organized as follows. In section 2.2 we state model assumptions and derive model equations. Then we separate our study into two parts. In the first part of the chapter (sections 2.3-2.4) we consider the case when the spacing between the Kt binders and the MT lattice binding sites are integer multiples of each other (in-register case); in the second part (sections 2.5 and 2.6) we examine the case when binder spacing is not an integer multiple of the MT lattice binding site spacing (off-register case). In section 2.3 we find numerical solutions for system breaking loads and the force-velocity relation when the strength of binding between the motor and the MT lattice is varied. In section 2.4 we use homogenization to find analytical

expressions for the breaking loads and the force-velocity relation in the limit of low unit activation energy for binding. Finally, in sections 2.5 and 2.6 we repeat our simulations and calculations from section 2.3 and 2.4 for the off-register case.

2.2 Mathematical model

Based on recent structural data [1][9], it is assumed that a kinetochore motor consists of a collection of fibers extending from the kinetochore plate, each with multiple binding attachments (motor binders) that can weakly bind onto the lattice of an inserted MT, see Figure 2.1. These fibers form a structure analogous to the rigid sleeve of Hill, but they are assumed to be sufficiently flexible so that they can attach to the flaring microtubules. The MT lattice is assumed to have one motor binder binding site per tubulin dimer. Thus, each binder has an additional preference to attach to a specific binding site after associating with the MT lattice.

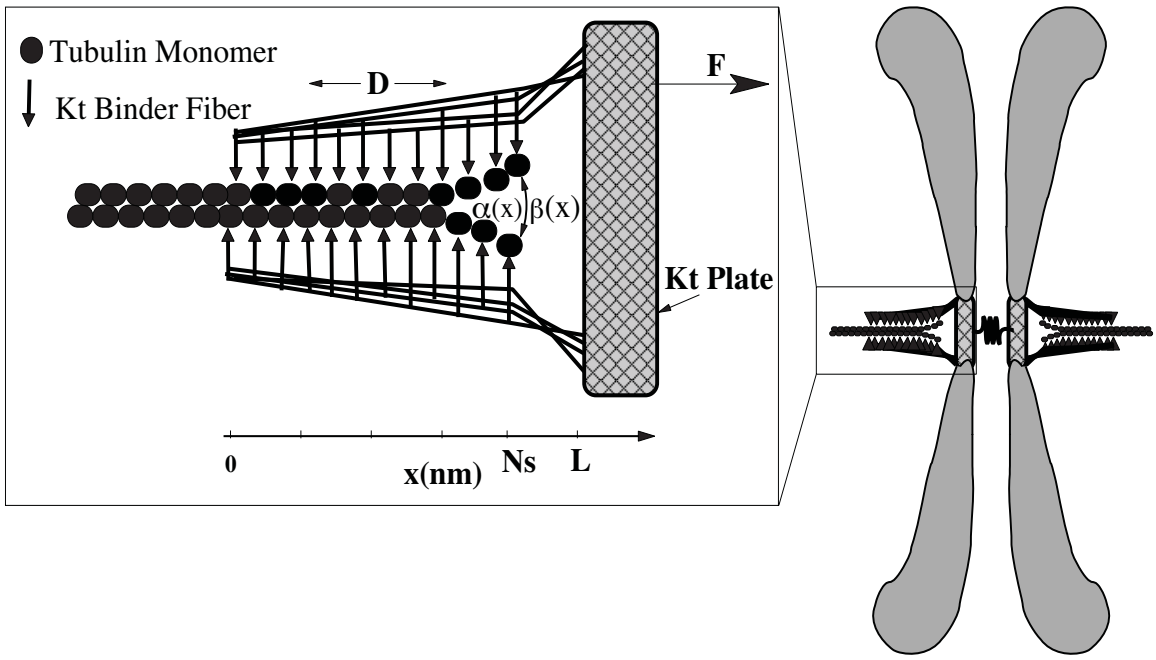

Figure 2.1. A schematic of the kinetochore motor model components. The kinetochore is composed of several binder fibers which are connected to the Kt plate on one end and can bind the MT lattice. For a kinetochore motor, N binders are uniformly spaced a distance s apart from one another along the microtubule lattice, from $x = 0$ to $x = Ns$. The attached MT polymer is dynamic and the tip polymerizes/depolymerizes with prescribed rates $\alpha(x), \beta(x)$.

Since a motor binder is assumed to be weakly bound to a microtubule, the kinetochore binders experience thermal motion (diffusion) on the lattice of an attached MT. However, since the binders are physically linked to each other on the fibers, the entire coupler experiences 1D diffusion on the polymer lattice.

Finally, a polymer embedded in the kinetochore motor can grow/shorten with prescribed polymerization/depolymerization rates, specified below. We also assume that if due to thermal motion the kinetochore plate is pushed against the polymer tip, polymerization is prevented by the lack of space, while the energy of polymerization is sufficiently large so that a tubulin monomer is not subsequently cleaved [13].

To describe the motion of the kinetochore motor, we suppose that motion is one dimensional along the horizontal x-axis. The motor position variable, x, marks the distance between the polymer tip and the coupler end distal to the kinetochore plate. Thus, the position axis starts at the coupler entry point ($x = 0$ nm) and extends to the Kt plate ($x = L$), Figure 2.1.

In the viscous-dominated limit, the motor system can be modeled with a one dimensional jump-diffusion process described by the stochastic differential equation (Langevin equation)

$$dx(t) = \frac{1}{\nu}(-\Psi'(x) - F)dt + \sigma_D(x(t))dW_t + \delta dN_\alpha(t) - \delta dN_\beta(t), \tag{2.1}$$

where $x(t)$ represents the position of the polymer tip relative to the coupler, $N_\alpha(t)$, and $N_\beta(t)$ are independent homogenous Poisson processes with amplitudes δ (tubulin size) and position dependent rates $\alpha(x)$ and $\beta(x)$, which govern MT tubulin addition/removal respectively; W_t is standard white noise applied to the motor with amplitude $\sigma_D(x(t))$. The term $\Psi'(x)$ represents polymer lattice binding forces, F describes loads on the kinetochore motor, and ν is the effective drag coefficient for the coupler.

Binding interactions between the coupler and the polymer are characterized by the potential function, $\Psi(x)$. We construct this function by envisioning the MT polymer as a semi-infinite linear chain of monomer beads that are rigidly connected. For a MT with 13 protofilaments and 8 nm long tubulin dimers, the monomer size in the linear chain is $\delta = 8/13$ nm. Individual binders can attach to the monomer beads with potential energy function $\psi(x)$, as shown in Figure 2.2. The net energy associated with polymer binding by the motor is the sum of the potential energy of all attached binders,

$$\Psi(x) = \sum_{n=0}^{N} \psi(x - ns). \tag{2.2}$$

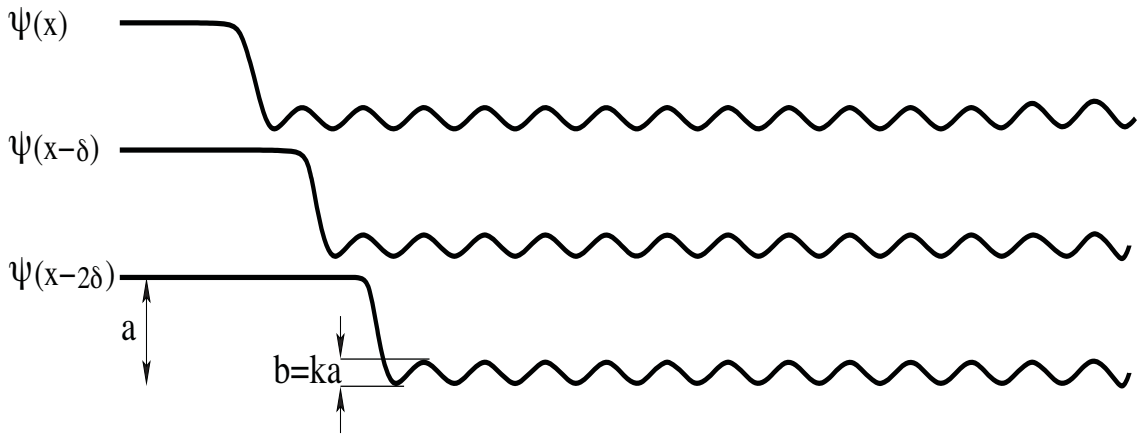

Figure 2.2. Diagram of the potential well component functions, $\psi(x)$. The energy function becomes periodic when a binder is bound to the MT due to the polymer lattice binding site periodicity.

The unit energy terms, $\psi(x)$, in the sum are shifted by an arbitrary amount, s to account for the offset between consecutive Kt binders. We use

$$\psi(x) = \frac{b}{2}\sin\left(\frac{2\pi x}{\delta}\right)\Big(1+\tanh(\lambda_1 x)\Big) - \frac{a}{2}\Big(1+\tanh(\lambda_2 x)\Big), \tag{2.3}$$

with $\lambda_1 >> \lambda_2$. An exact representation of the function $\Psi(x)$ can be given, however, it is more convenient for computational purposes to use an approximate representation for the well, which we provide in the following sections.

In our analysis we consider two cases for the shift parameter s: a) $s = \delta$ in which case the period of the binders is the same as the MT lattice binding site period (in-register), and b) $s = \bar{\kappa}\delta$ where $\bar{\kappa}$ is not an integer (off-register). In the second case, we are interested in $\bar{\kappa} > 1$ since for these values the number of linkers that can bind the MT is in good agreement with the binder numbers recently predicted in experimental studies [14].

For this model binding involves two steps, first binder association with the polymer and then binder transition on the lattice due to additional preference for polymer binding sites. Therefore, for $\psi(x)$ we assume that for each new binding interaction established between the binders and the polymer, the system free energy is lowered by the amount "$-a$", see Figure 2.2. Once one binder is engaged, it then has to hop between δ-separated binding sites on the MT lattice, which produces the periodic part of the unit energy function $\psi(x)$. Each thermally induced hopping event of the linkers on the polymer lattice has to overcome

a unit potential energy barrier corresponding to the energy needed for existing bonds to break and a new one to reform. We denote the barrier by "b" in the well, where $b = ka$ as shown in Figure 2.2. While the kMT increases overlap with the kinetochore motor, more bonds are established so that total system free energy in Ψ decreases in multiples of a; however more bonds must also be broken so that the net potential barrier increases by some multiple of b, as shown in Figure 2.3. The rate of increase in the net barrier for Ψ depends on the overlap parameter, s. When $s = \delta$ the net barrier increases linearly, since for each attachment event exactly one bond must be broken to readjust the overlap. If on the other hand, $s = \bar{\kappa}\delta$ then the net activation barrier grows slower than linear as overlap increases. In both cases, we obtain a corrugated well, $\Psi(x)$ that has the net effect of a drift force that biases the diffusion of the polymer further inside the coupler.

It is possible that the polymer tip moves either by diffusion or polymerization past the last coupler binder. At this position all the available binding sites are occupied, so there is no gain for the system to bias thermal motion in either direction; further kMT insertion into the coupler does not lower the free energy. Nonetheless, if the coupler moves in this region it must cross the potential barrier associated with breaking all N_1 or N_2 bonds. Consequently, the potential well function $\Psi(x)$ loses its tilt and becomes periodic past the last binder position at $x = N_i s$ nm as shown in Figure 2.3A and 2.3B. The numbers N_1,

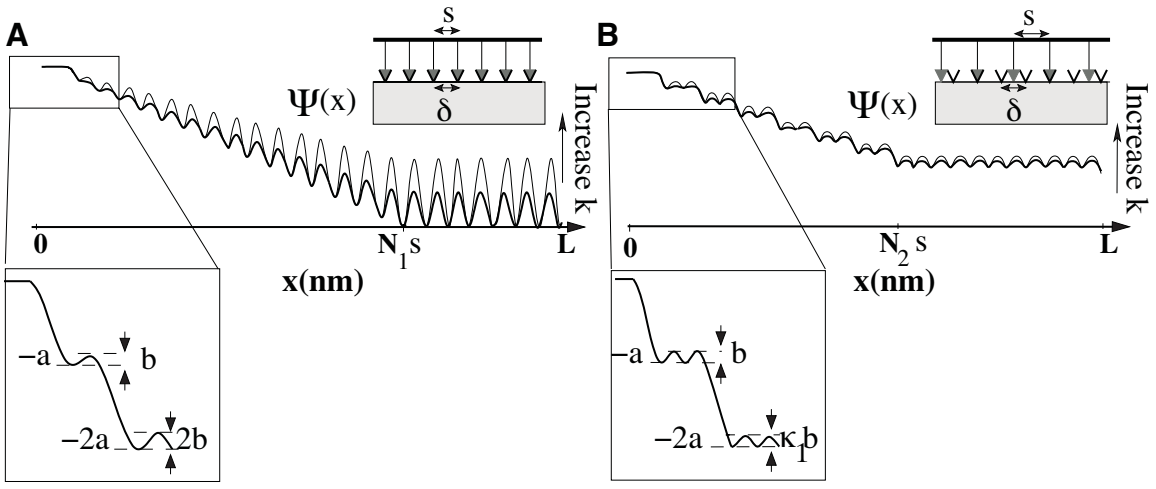

Figure 2.3. Diagram of the potential energy well, $\Psi(x)$ for varying s. **A.** The potential energy well for the in-register well with binder spacing $s = \delta$. **B.** The potential energy well for the off-register well with $s = \bar{\kappa}\delta$.

N_2 are chosen such that the motor binders are uniformly spread along ≈ 40 nm for both the in-register and off-register Kt motors.

Spindle forces acting on a chromosome create mechanical stress on kinetochores producing load (F) on the motor. With our sign convention, $F > 0$ pushes on a kinetochore in such a way as to increase the distance between the polymer tip and the kinetochore (i.e., to decrease x), whereas $F < 0$ favors polymer tip insertion toward $x = L$, increasing x.

Finally, the tip of the inserted polymer is dynamic and can grow or shorten with prescribed rates that vary with the position of the tip relative to the kinetochore coupler. A plot of the rates is shown in Figure 2.4. We assume that a powerful depolymerase (such as the kinesin MCAK [1]) is enriched at the coupler end proximal to the kinetochore plate. Hence, we choose a depolymerization rate that depends on the position of the kMT tip relative to the motor with $\beta(x) = \beta_0 + (\beta_2 - \beta_0)/(1 + \exp(-\lambda(x - \beta_1)))$, where λ controls the steepness of the rate transition and $\beta_1 < N_i s$. On the other hand, we keep the polymerization rate constant independent of the MT tip position relative to the coupler, except for the restriction that if the polymer tip is located less than δ away from the $x = L$ boundary, then no new monomers can be inserted with $\alpha(x) = \alpha_0/(1 + \exp(\lambda(x - \alpha_1)))$. We note here that we have not chosen the polymerization rate to be a heaviside function as in [13]. This is because, we believe, it is unlikely that the polymerization rate drops instantaneously at the $x = L - \delta$ position if one takes into account random fluctuations in MT monomer size. Thus, we assume that a space slightly more than δ between the polymer tip and the KT plate is necessary for the MT to be able to polymerize at the full rate α_0. Finally, the constant basal polymerization and depolymerization rates α_0, β_0 reflect the presence of several kinetochore enzymes that have been shown to favor slow kMT growth or shortening [1].

The SDE in eq. (2.1) corresponds to the forward Chapman-Kolmogorov equation [3]

$$\begin{aligned}\frac{\partial p(x,t)}{\partial t} = &-\frac{1}{\nu}\frac{\partial}{\partial x}\Big(V'(x)p(x,t)\Big) + D\frac{\partial^2}{\partial x^2}p(x,t) + \alpha(x-\delta)p(x-\delta,t) \\ &+ \beta(x+\delta)p(x+\delta,t) - (\alpha(x)+\beta(x))p(x,t) \end{aligned} \tag{2.4}$$

where $p(x,t)$ is the probability density function for the relative position of the attached MT tip with respect to the coupler, x, and $V'(x) = -\Psi'(x) - F$. For the additive Gaussian noise we take $\sigma_D(x(t)) = \sqrt{2D}$, where D is the diffusion coefficient of the coupler, calculated according to the Einstein relation $D = k_B T/\nu$. The value used for this coefficient agrees with coefficients chosen in previous models [5][7].

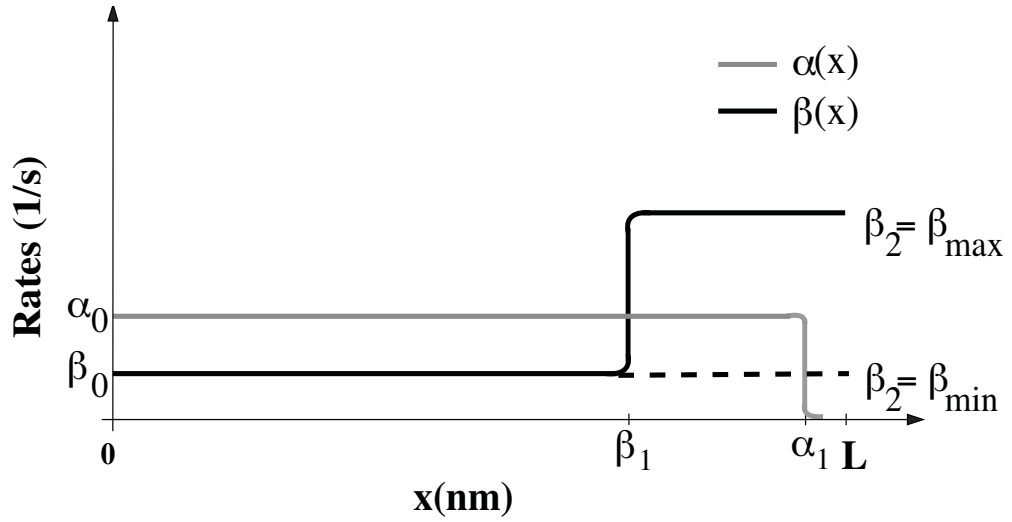

Figure 2.4. Kinetochore microtubule tip rate functions. The polymerization rate is given by $\alpha(x)$ and $\beta(x)$ describes the depolymerization rate. Parameter values are given in Table 2.1.

To complete the specification of the problem, we impose a reflecting boundary at $x = L$ where the kinetochore wall physically impedes polymer penetration. At $x = 0$, we prescribe an absorbing boundary, since if the polymer tip crosses this point the coupling connection is broken and not likely to be reestablished. Unless otherwise stated, the parameters used for calculations in this chapter are given by those in Table 2.1. Some parameters in Table 2.1 are estimated from parameter ranges reported in the literature. The specific values chosen here produce motor velocities that are in agreement with chromosome movement velocities observed in newt lung cells [16].

2.3 In-Register well

We approximate the potential well function of the in-register case with

$$\Psi(x) = \begin{cases} f(x)\left(1 - \cos(\frac{2\pi x}{\delta})\right) + h(x) & x \leq N_1 s \\ f(N_1\delta)\left(1 - \cos(\frac{2\pi x}{\delta})\right) + h(N_1\delta) & x > N_1 s. \end{cases} \tag{2.5}$$

where $f(x) = \frac{a}{2\delta}\left(\frac{b}{a}x + C\right)$, $C = 0.172$ and $h(x) = -\frac{ax}{\delta}$. The linear and scalar coefficients in eq. (2.5) arise because we use a Fourier series to approximate the well function expression given in eq. (2.2). In what follows we set $b = ka$ and then vary k to control the relative amplitude of well corrugation, as depicted by the diagram in Figure 2.3A.

Table 2.1. Model parameter values.

Parameter	Description	Value
L	Kinetochore thickness	50 nm [1]
δ	Binding site period on the MT lattice	8/13 nm
ν	Effective viscous drag coefficient	6 pNs/μm [7]
α_0	Rate of tubulin subunit addition	80 s^{-1} [7]
β_0	Basal rate of tubulin subunit removal	27 s^{-1} [7]
β_2	Max. rate of removal of tubulin	27 s^{-1}, 100 s^{-1} (estimated)
β_1	Depol. rate transition point	35 nm (estimated)
α_1	Pol. rate transition point	$L - 1.6\delta$ (estimated)
a	Free energy of binding	2.6 k_BT [5]
D	Coupler diffusion coefficient	690 nm/s^2 [5][7]
N_1	In-register Kt binder number	65
N_2	Off-register Kt binder number	30

2.3.1 Numerical calculation of force-velocity relations

As it is customary for molecular motors, we are interested in calculating the force-velocity relation. In general, the velocity of the Kt motor with respect to an outside frame of reference must account for the internal velocity of the inserted kMT relative to the coupler. However, if the polymer-coupler assembly has reached an internal equilibrium or steady-state (i.e., there is no motion of the tip relative to the binding sites), the velocity calculation is greatly simplified. This is because, at steady-state the ensemble of binding sites plus the polymer is moving with respect to an outside frame of reference at a velocity that is equal to the balance of kMT polymerization/depolymerization rates.

Before we start seeking steady-state solutions we must recognize an important fact: with our current boundary conditions a steady-state solution of eq. (2.1) does not exist. This is due to the absorbing boundary condition at $x = 0$, which causes the polymer to eventually decouple. Nevertheless, if the polymer reaches a metastable position inside the coupler sufficiently far away from the absorbing boundary, we can safely approximate the $x = 0$ position as a reflecting barrier and solve for a steady-state solution of eq. (2.1). One way to determine the validity of this approximation is to determine the time it takes a polymer to find the absorbing boundary if it starts from some position in $(0, L)$. Thus, as a first step we formulate and then solve the mean first exit time problem for the polymer tip of an attached MT.

We let $T(x)$ be the mean time for exit through $x = 0$, starting from $x \leq L$. Then [3]

$$-1 = \frac{1}{\nu}V'(x)\partial_x T(x) + D\partial_x^2 T(x) + \alpha(x)(T(x+\delta) - T(x)) + \beta(x)(T(x-\delta) - T(x)) \quad (2.6)$$

with boundary conditions $T(0) = 0$, $T'(L) = 0$.

The dde in eq. (2.6) cannot be solved analytically, however we can obtain an estimate for the solutions numerically. For our numerical studies we simulate a large number of Monte Carlo trials (1000 trials) of the Langevin equation in eq. (2.1) for various model parameter values. For each trial we record the exit time and then the results are averaged over the total number of paths tried.

In Figure 2.5, we show a plot of the Monte Carlo trials for the mean first exit times of the system for various loads, F and activation energy levels, measured by the parameter k. From Figure 2.5, we see that increases in motor loads decrease the time for exit from the coupler significantly. This is expected since forces $F > 0$ decrease x by counteracting well attractive forces thus making it easier for the motor to escape through the absorbing boundary. From our simulations, we observe that for a wide range of loads the polymer does not exit the coupler for long times as compared to the relaxation time, i.e., $\langle T(L)\rangle > 100$ s, whereas the time to relaxation to a steady-state is ≈ 1 s. Indeed, in Figure 2.5 simulations are only shown for $F \geq 19$ pN due to the large values of the first passage times that result when F is smaller than 19 pN. Thereby, a steady-state approximation is appropriate for forces with large exit times. Further, when the activation energies increase, the system takes longer to escape from the absorbing boundary, as shown by the upward shifts in the mean first exit time curves in Figure 2.5 as k increases. These shifts can be explained by observing that for higher k it takes more energy for the polymer to detach from the

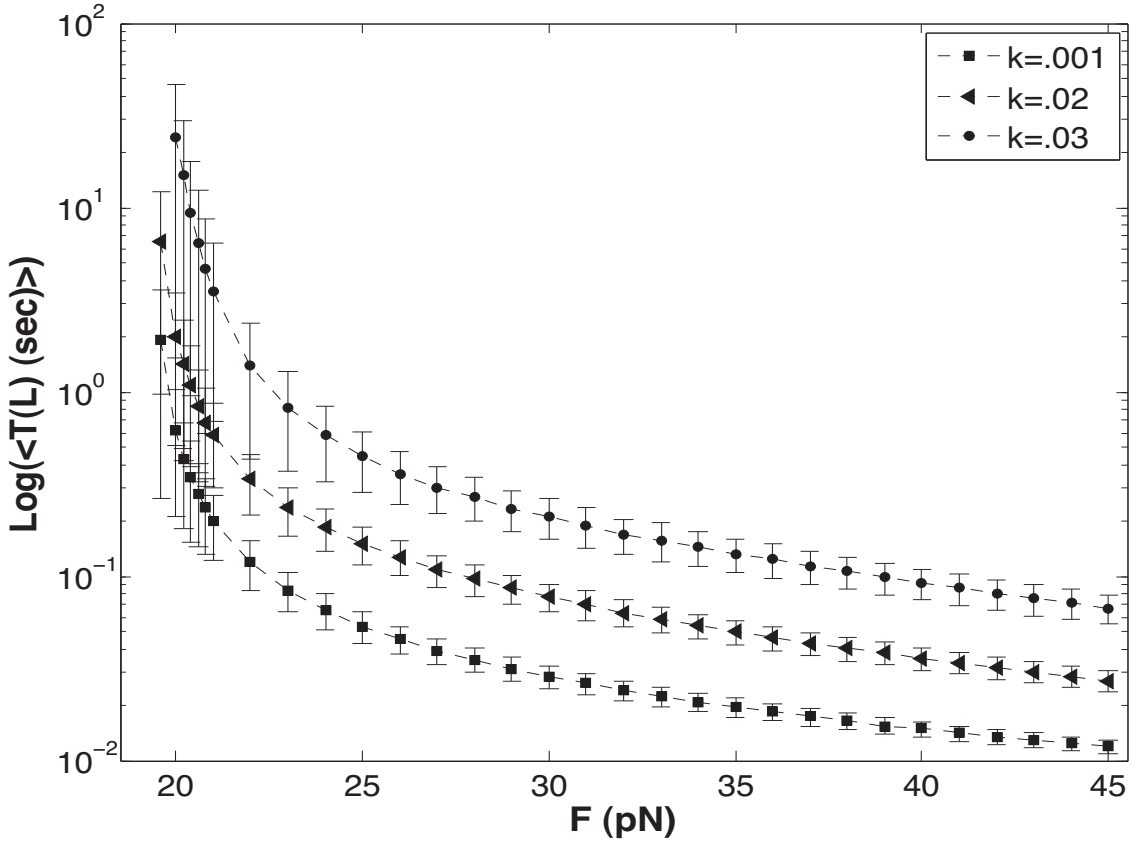

Figure 2.5. Monte Carlo simulation results for the mean first exit times from $x = 0$, starting from $x = L$. Each curve represents the mean first exit time estimates for a given value of k, with $\beta_2 = 100\ \mathrm{s}^{-1}$. Polymer tips start at $x = L$ at $t = 0$ and then the measured times for exit from the left boundary are averaged over 1000 trials for each F. The error bars mark the standard deviation. The maximum time allotted for exit was $T_{\max} = 800$ s. For $F < 19$ pN exit times exceeded $T_{\max}$ so computations were restricted to $F \geq 19$ pN.

coupler and hence more force is necessary to pull the polymer out of the chamber. For low activation energies ($k = 0.001$), the system is more "slippery" with metastable states occurring for a smaller range of loads with $F \leq 18$ pN. The range of forces supported by these motors is in agreement with the predictions of [7]. Measurements of anaphase forces in meiotic grasshopper spermatocytes, have produced maximal chromosomal forces on the order of 700 pN [12]. With our force estimates, we predict that for the total number of motors engaged in these chromosomes, we have 35×18 pN $= 630$ pN, which is consistent with experimental observations. Hence, we conclude that it is necessary to restrict the range of loads ($F \leq F_{\text{break}} \approx 18$ pN) for which the system can be examined at steady-state, and that the activation energies for the binding sites can significantly affect the range of forces that the motor can support.

Now that we have a range of loads for which the system equilibrates, we seek to find the kMT tip positions at steady-state for various amounts of motor loads and Kt/MT binding strengths. The steady-state positions can be obtained by solving the delay-differential equation

$$\begin{aligned} 0 = &-\frac{1}{\nu}\frac{\partial}{\partial x}\left(V'(x)p(x,t)\right) + D\frac{\partial^2}{\partial x^2}p(x,t) + \alpha(x-\delta)p(x-\delta,t) + \beta(x+\delta)p(x+\delta,t) \\ &- (\alpha(x)+\beta(x))p(x,t). \end{aligned} \tag{2.7}$$

Eq. (2.7) cannot be solved analytically, but numerical solutions of the steady-state distributions can be easily obtained with Monte-Carlo simulations of the Langevin equation in eq. (2.1). For each trial, we allow the system to relax into steady-state and then record the final position of the kMT tip after some prescribed amount of time.

In Figure 2.6 and Figure 2.7, we have plotted normalized histograms of the system at steady-state for varying values of the parameter k and force, F. In Figure 2.6 the plots are generated for a depolymerizing motor ($\beta_2 > \alpha_0$), whereas in Figure 2.7 the plots are generated for a polymerizing motor ($\beta_2 < \alpha_0$). In both rate regimes, as the activation energy increases the polymer settles on average closer to $x = x_0$, the position where the kMT tip rates equilibrate with one another so that $\alpha(x_0) = \beta(x_0)$ ($x_0 \approx \beta_1$ for a depolymerizing motor and $x_0 \approx \alpha_1$ for a polymerizing motor). For the highest barrier tried with $k = 0.08$, one immediately notices that the distributions are centered exactly at x_0. This can be explained by noting that for high activation barriers, the only way the system can transition down the potential well landscape is by jumping via the net Poisson jump rates given that the diffusion rate is too small to overcome the well barriers. Also, since the Poisson jumps

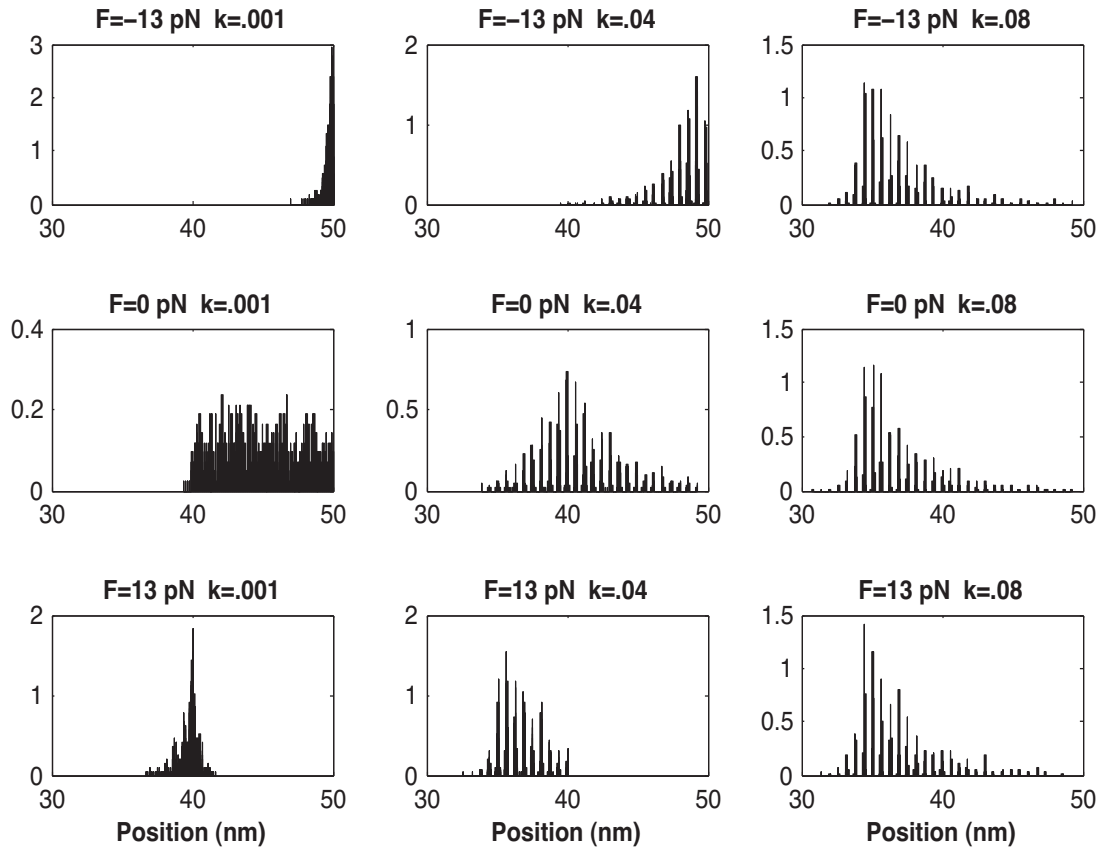

Figure 2.6. Normalized histograms of the numerical simulation results with varying activation barriers and motor loads for a depolymerizing motor with $\beta_2 = 100\text{s}^{-1} > \alpha_0 = 80\text{s}^{-1}$. The histograms are generated by gathering simulation statistics for 1000 trials after relaxation into steady-state.

control the equilibrium positions when k is large, it follows that the motor steady-state positions are insensitive to motor loads, which when varied only alter the tilt and thus minimum of the potential well function. On the other hand, if the well barriers are low, then diffusion is sufficient to transition the polymer tip to the minimum energy state of $\Psi(x)$ independent of the polymerization/depolymerization rates (as long as α, β are small). Further, in the low k limit, the positions where the distributions center in the well depend on the amount of load on the motor. As the pulling loads ($F > 0$) on the motor increase, the well loses its tilt and the peaks of the distributions relocate closer to $x = 0$. Whereas as the pushing loads increase ($F < 0$) in magnitude the overlap bias is increased and the steady-state distributions are pushed closer to $x = L$ boundary (see the $k = 0.001$ panels in Figure 2.6 and Figure 2.7). For intermediate $k = 0.04$, we see that the distributions

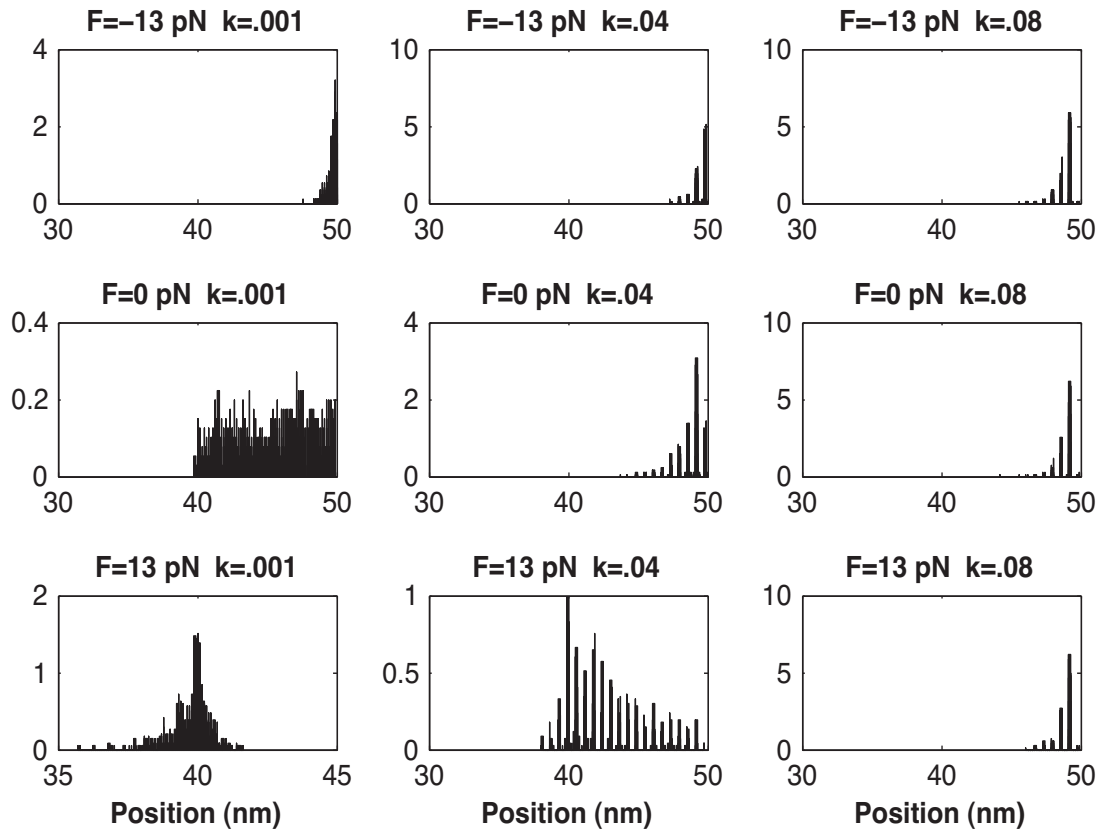

Figure 2.7. Normalized histograms of the numerical simulation results with varying activation barriers and motor loads for a polymerizing motor $\beta_2 = 27\text{s}^{-1} < \alpha_0 = 80\text{s}^{-1}$. Each histogram is generated by gathering simulation statistics for 1000 trials after relaxation into steady-state.

are sensitive to the loads while also settling closer to x_0. In summary, we deduce that the position of the peaks of the steady-state probability distributions of kMT tips depend on the height of the unit activation barrier, k. If k is sufficiently small, then the distributions also depend on the motor loads, F.

We are now ready to calculate motor velocities. As noted at the beginning of this section, at steady-state, the velocity of the system with respect to an outside frame of reference (let this frame have horizontal displacement measured by y) has a velocity which depends entirely on the net balance between the polymerization and depolymerization rates,

$$v = \delta \int \Big(\alpha(y) - \beta(y)\Big) p_s(y) dy, \tag{2.8}$$

with $p_s(y)$ the steady-state distribution probability density for the position of the kMT tip. Eq. (2.8) tells us that the motor velocity can be easily obtained by calculating the balance of the jump rates at the kMT tip steady-state position. Therefore, even though we do not currently have analytic expressions for $p_s(y)$, we can obtain velocity values for a given load F from Monte-Carlo simulations by sampling the forward and backward jump rates after the system reaches an equilibrium.

In Figure 2.8, we show load-velocity calculations from the simulations for various values of k.

From the load-velocity curves plotted in Figure 2.8, we see that the system produces distinct regions of constant velocity for a wide range of pulling loads when k is small ($k \leq 0.03$) for both polymerizing and depolymerizing motors. This can be explained by examining the steady-state distributions in Figures 2.6, 2.7. For low activation barriers, as the forces on the motor vary, the steady-state distributions experience shifts on the x-axis. However, since at steady-state the velocity depends only on the kMT polymerization/depolymerization

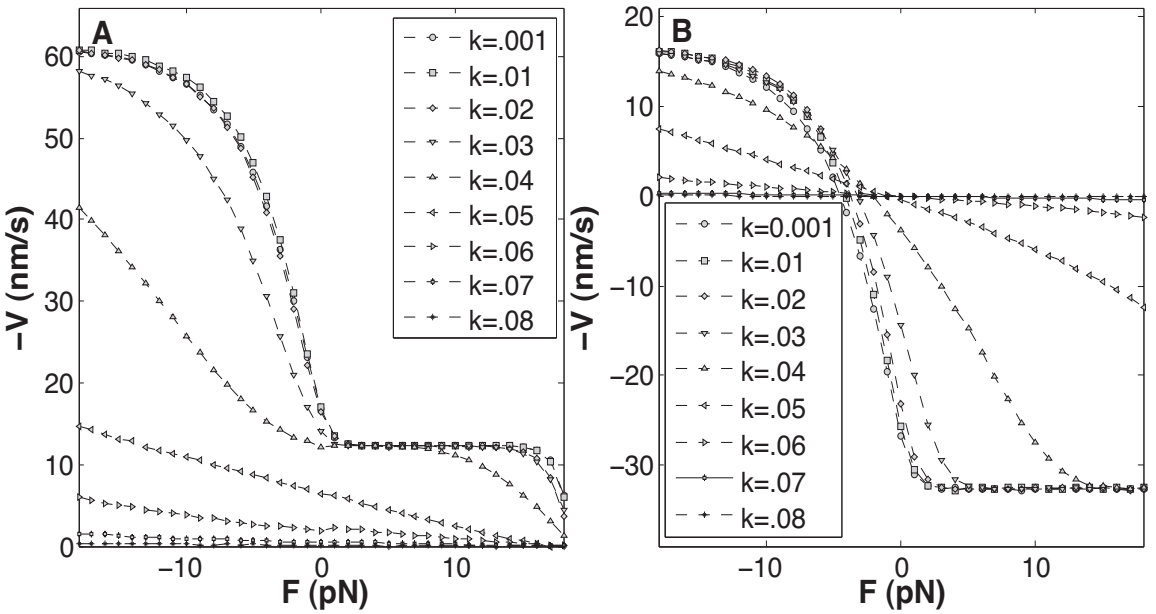

Figure 2.8. Numerical load-velocity relationships for varying k. Velocities are obtained by averaging the numerical trial velocities, which are calculated by sampling the forward and backward jumps of the MT tip after the system relaxes into steady-state. **A**. Force-velocity calculations for a depolymerizing motor with $\beta_2 = 100\text{s}^{-1} > \alpha_0 = 80\text{s}^{-1}$. **B**. Force-velocity calculations for a polymerizing motor with $\beta_2 = 27\text{s}^{-1} < \alpha_0 = 80\text{s}^{-1}$.

rates, if the difference between $\alpha(x)$ and $\beta(x)$ is the same in the new shifted equilibrium position then the motor velocity does not change. Consequently, there are flat velocity regions in the force-velocity curves for small k and $F > 0$ that keep the distributions in areas of constant net kMT rates. On the other hand, if we increase k the flat regions in the force-velocity curves start to disappear. This happens because as k increases, the steady-state distributions tend to center closer to the Poisson rate transition points, β_1, α_1. Being already located in sensitive regions, small perturbations in load can easily push the tip distributions on either side of the rate transition points and thus considerably disrupt the $\alpha(x), \beta(x)$ contribution to the velocity. Thus, the motors are more sensitive to loads and the force-velocity relations become more uniformly monotone when k is increased, as shown in Figure 2.8. Indeed, if we increase k enough, the steady-state distributions become immobilized and center at exactly the rate transition points so that motor velocities decay to almost zero, resulting in the motor being stalled independent of load (see the force-velocity curves for $k = 0.08$).

The nonlinear force-velocity relations for $k \leq 0.03$ shown in Figure 2.8 are quite different from the typical linear force-velocity relations obtained for conventional motors such as kinesin and dynein. As noted above, the constant velocity regions depend directly on the balance of kMT rates for a kinetochore motor. It follows that if we change the concentration of the kinesin inside the motor by lowering β_2, for example, then the force-velocity relation for the motor will shift down the velocity axis to reflect the change in the rate balance (compare the force-velocity curves for $k \leq 0.03$ in Figure 2.8A and Figure 2.8B). Thus, variations in kMT depolymerization rates in the low k regime produce shifts in the force-velocity relations. This shift is significant when $\beta_2 < \alpha_0$ since motor velocities reverse signs, signaling a change in motor direction. The latter means that our motor model displays chemically controlled bidirectionality induced by modification of the depolymerase concentrations at the Kt. This feature of chemical control can be very useful when modeling chromosome movement during mitosis, where both chemical and mechanical signals can create feedback for kinetochore motion control [15].

Next, we consider the monotone regions of the force-velocity relations for small k. By our convention for F values, if $F < 0$ the motor operates in the thermal ratchet regime. Under large pushing load, the gap between the polymer tip and the Kt plate becomes very small, with steady-state distributions equilibrating less than δ away from $x = L$. In this scenario, since there is little space between the polymer and the barrier, polymerization against

the Kt plate is insignificant and motor velocities limit to $\delta\beta_2$. If β_2 is large, then motors experience rapid increments in depolymerizing velocity as F becomes more negative, see Figure 2.8A. In the polymerizing motor case shown in panel B of Figure 2.8, this ratcheting effect is particularly prominent since it indicates that a polymerizing motor eventually transitions into a depolymerizing state (i.e., reverses direction of motion) when subjected to large negative pushing loads. On the other hand, if too much pulling load is placed on the motor (F large and positive), the polymer is pulled out of the chamber and velocities quickly decay due to steady-state distribution shifts in regions where $\alpha_0 > \beta_0$ (note that for the polymerizing motor shown in Figure 2.8B for large $F > 0$, velocities remain constant because of our choice of $\beta_2 = \beta_0$).

In summary, our numerical solutions show that the jump-diffusion model proposed here produces constant motor velocities that are sensitive to kMT tip rate variations for weak binding (k small "slippery" regime), in agreement with experimental observations. We also found that when the activation barriers for detachment are increased, the motor transitions into stationary states where attachment is maintained against large loads as shown by the mean first exit time calculations. It is possible that this stalled or "sticky" motor regime is employed in cells where Kts need to maintain attachment despite significant increases in forces opposing movement. Our model shows that attachment robustness can be greatly improved by increasing binding affinities of the Kt binders for the MT lattice, however robustness is achieved at the expense of velocity. Experimental work has shown that the inhibition of phosphorylation of Ndc80 binding filaments by Aurora B kinases at kinetochores, increases the binding affinity of the linkers for the kMT lattice and also results in kinetochores being immobilized on the kMT lattice [2]. Our model predicts that this observed immobility could be the result of only changes in filament affinity for the kMT lattice, independent of the polymerization/depolymerization dynamics of the inserted polymer tip. In the second part of this chapter we will see that variations in the spatial distribution of Kt binders on the MT lattice can dramatically change motor response to changes in the parameter k.

2.3.2 Asymptotic approximation

From the simulations of the jump-diffusion model, we see that the height of the activation energy barrier between binding sites can greatly affect motor motion characteristics. However, Monte-Carlo simulations are computationally expensive so it would be useful to explore parameter ranges for which analytical expressions for the force-velocity relationship

can be derived. In this section, we use homogenization theory in order to obtain simpler approximate analytical force-velocity relation expressions for the Kt motor model.

Since we are ultimately interested in determining the force-velocity relation for the motor, the equation of interest for approximation is the steady-state equation for the probability density, which reads

$$0 = -\frac{1}{\nu}\frac{\partial}{\partial x}\left[\left(f(x)\cos\left(\frac{2\pi x}{\delta}\right)+r(x)\right)' p(x)\right] + Dp_{xx}(x) - \Big(\alpha(x)+\beta(x)\Big)p(x) + \beta(x+\delta)p(x+\delta)+\alpha(x-\delta)p(x-\delta), \tag{2.9}$$

where we have used the expression in eq. (2.5) for $\Psi(x)$ and $r(x) = -f(x) - h(x) - Fx$.

We start by Taylor expanding the jump terms, which introduces an infinite sum term in eq. (2.9). Then, using the no flux boundary conditions we integrate eq. (2.9) once to obtain

$$0 = -\frac{1}{\nu}\left(f(x)\cos\left(\frac{2\pi x}{\delta}\right)+r(x)\right)' p(x) + Dp_x(x) + \sum_{n=1}^{\infty}\frac{\delta^n}{n!}\frac{d^{n-1}}{dx^{n-1}}\Big(\Big(\beta(x)+(-1)^n\alpha(x)\Big)p(x)\Big). \tag{2.10}$$

From the numerical solutions of the steady-state distributions, we notice that the solution to eq. (2.10) should contain high frequency periodic oscillations with a slow varying amplitude. In order to identify equation terms that evolve on different spatial scales, it is necessary to rescale space in eq. (2.10). We set $x = Xy = \dfrac{\nu D\delta}{b}y$, where y is a dimensionless variable. In terms of the variable y the steady-state equation reads

$$0 = -\left(\hat{f}(y)\cos\left(\frac{2\pi y}{\varepsilon}\right)+\hat{r}(y)\right)' p(y) + p_y(y) + \alpha_2\sum_{n=1}^{\infty}\frac{\varepsilon^{n-1}}{n!}\frac{d^{n-1}}{dy^{n-1}}\left(\left(\hat{\beta}(y)+(-1)^n\hat{\alpha}(y)\right)p(y)\right), \tag{2.11}$$

where we identify $\varepsilon = b/k_BT$ as the small dimensionless parameter and $\alpha_2 = \beta_0\delta^2\nu/b$. Also, $\hat{f}(y) = f(y)/\nu D$, $\hat{r}(y) = r(y)/\nu D$, $\hat{\beta}(y) = \beta(y)/\beta_0$, $\hat{\alpha}(y) = \alpha(y)/\beta_0$. Note that this change of variables allowed us to rewrite the oscillatory part of the drift term as a high frequency periodic oscillator with a slow varying amplitude.

Following the multiscale technique we now introduce two spatial variables: a "slow" variable $z = y$ and a "fast" variable $\sigma = \dfrac{y}{\varepsilon}$. Immediately, we see that the drift term in eq. (2.11) contains fast oscillations with a slow varying amplitude.

Next, we treat z and σ as independent variables and by the chain rule, $\frac{d}{dy} = \frac{\partial}{\partial z} + \frac{1}{\varepsilon}\frac{\partial}{\partial \sigma}$. The equation now becomes

$$\begin{aligned} 0 = &- \left(\hat{f}'(z)\cos(2\pi\sigma) + \hat{r}'(z) - \frac{2\pi}{\varepsilon}\hat{f}(z)\sin(2\pi\sigma) \right) p(z) + p_z(z) + \frac{1}{\varepsilon}p_\sigma(z) \\ &+ \alpha_2 \sum_{n=1}^{\infty} \frac{\hat{\beta}(z) + (-1)^n \hat{\alpha}(z)}{n!} \frac{\partial^{n-1}}{\partial \sigma^{n-1}} p(z,\sigma) \\ &+ \varepsilon\alpha_2 \sum_{n=2}^{\infty} \frac{(n-1)}{n!} \frac{\partial}{\partial z} \frac{\partial^{n-2}}{\partial \sigma^{n-2}} \Big(\Big(\hat{\beta}(z) + (-1)^n \hat{\alpha}(z) \Big) p(z) \Big) + O\left(\varepsilon^2\right) ... \end{aligned} \tag{2.12}$$

As is customary for the multiscale method, we seek a solution that can be written as an asymptotic series $p(z) = p_0(z,\sigma) + \varepsilon p_1(z,\sigma) + O\left(\varepsilon^2\right)$ where $p_0(z,\sigma)$ represents the mean field, and p_1 has zero mean value in z and is periodic in σ, with period 1. Substituting the expansion for $p(z)$ into eq. (2.12) and collecting same order terms we obtain the following hierarchy of equations,

$$O\left(\frac{1}{\varepsilon}\right) : 2\pi\hat{f}(z)\sin(2\pi\sigma)p_0(z,\sigma) + p_{0\sigma}(z,\sigma) = 0, \tag{2.13}$$

$$\begin{aligned} O(1) : &2\pi\hat{f}(z)\sin(2\pi\sigma)p_1(z,\sigma) + p_{1\sigma}(z,\sigma) - \Big(\hat{f}'(z)\cos(2\pi\sigma) + \hat{r}'(z) \Big) p_0(z,\sigma) \\ &+ p_{0z}(z,\sigma) + \alpha_2 \sum_{n=1}^{\infty} \frac{1}{n!} \Big(\hat{\beta}(z) + (-1)^n \hat{\alpha}(z) \Big) \frac{\partial^{n-1}}{\partial \sigma^{n-1}} p_0(z,\sigma) = 0. \end{aligned} \tag{2.14}$$

Finally, the probability densities need to be normalized, with

$$1 = \int_0^{L/X} \Big(p_0(z,\sigma) + \varepsilon p_1(z,\sigma) \Big) dz. \tag{2.15}$$

We solve eq. (2.13) by direct integration to obtain

$$p_0(z,\sigma) = A_0(z) \exp\left(\hat{f}(z)\cos(2\pi\sigma) \right). \tag{2.16}$$

Next, we examine the infinite sum term in eq. (2.14). For a fixed arbitrary value of $z = z_0$, we define $F(\sigma) = \int_0^{\sigma} p_0(z_0,\eta)d\eta$. Taylor expansion of $F(\sigma)$ gives

$$\int_0^1 p_0(z_0,\eta)d\eta = F(\sigma+1) - F(\sigma) = \sum_{n=1}^{\infty} \frac{1}{n!} \frac{\partial^n}{\partial \sigma^n} \left(\int_0^{\sigma} p_0(z_0,\eta)d\eta \right), \tag{2.17}$$

$$-\int_0^1 p_0(z_0,\eta)d\eta = F(\sigma-1) - F(\sigma) = \sum_{n=1}^{\infty} \frac{(-1)^n}{n!} \frac{\partial^n}{\partial \sigma^n} \left(\int_0^{\sigma} p_0(z_0,\eta)d\eta \right), \tag{2.18}$$

where we have used the periodicity of $p_0(z,\sigma)$ in σ for a fixed $z = z_0$.

Substituting the expressions from eqs. (2.17)-(2.18) into the O(1) equation we have

$$O(1) : 2\pi\hat{f}(z)\sin(2\pi\sigma)p_1(z,\sigma) + p_{1\sigma}(z,\sigma) - \Big(\hat{f}'(z)\cos(2\pi\sigma) + \hat{r}'(z)\Big)p_0(z,\sigma) + p_{0z}(z,\sigma) + \alpha_2\Big(\hat{\beta}(z) - \hat{\alpha}(z)\Big)\int_0^1 p_0(z,\sigma)d\sigma = 0. \tag{2.19}$$

We solve for the coefficient $A_0(z)$ by examining the $O(1)$ eq. (2.19). Since we are looking for a solution $p_1(z,\sigma)$ that is periodic in σ, we impose the following solvability condition on eq. (2.19),

$$\begin{aligned} 0 &= \int_0^1 \Bigg(\left(p_1(z,\sigma)I(z,\sigma)\right)_\sigma + \exp\left(\hat{r}(z)\right)\Big(p_0(z,\sigma)\exp(-\hat{r}(z))I(z,\sigma)\Big)_z \\ &\quad + \alpha_2\Big(\hat{\beta}(z) - \hat{\alpha}(z)\Big)\int_0^1 p_0(z,\eta)d\eta I(z,\sigma)\Bigg)\, d\sigma \\ &= -\hat{r}'(z)A_0(z) + A_0'(z) + \alpha_2 A_0(z)\Big(\hat{\beta}(z) - \hat{\alpha}(z)\Big)I_0^2\left(\hat{f}(z)\right), \end{aligned} \tag{2.20}$$

where $I(z,\sigma) = \exp\Big(-\hat{f}(z)\cos(2\pi\sigma)\Big)$ and $I_0(\hat{f}(z))$ is the integral form of the modified Bessel function of the first kind.

Therefore,

$$A_0(z) = \hat{C}\exp\left(\hat{r}(z) - \alpha_2\int I_0^2\left(\hat{f}(z)\right)\Big(\hat{\beta}(z) - \hat{\alpha}(z)\Big)dz\right). \tag{2.21}$$

Finally, in terms of our original variable x this yields the solution

$$p_0(x) = C\exp\left(\frac{V(x)}{k_BT} - \frac{\delta\nu}{k_BT}\int I_0^2\left(\frac{f(x)}{k_BT}\right)\Big(\beta(x) - \alpha(x)\Big)dx\right), \tag{2.22}$$

where the coefficient C is found from the normalization condition for the probability densities in eq. (2.15). Therefore, our approximation for the probability density function at steady-state is

$$p(x) \approx C\exp\left(\frac{V(x)}{k_BT} - \frac{\delta\nu}{k_BT}\int I_0^2\left(\frac{f(x)}{k_BT}\right)\Big(\beta(x) - \alpha(x)\Big)dx\right) + O(\varepsilon). \tag{2.23}$$

With the steady-state solutions for the system in eq. (2.23), we can readily calculate motor velocities using

$$v \approx v_0 + O(\varepsilon) \tag{2.24}$$

$$= \delta \int_0^L \Big(\alpha(x) - \beta(x)\Big) p_0(x) dx + O(\varepsilon) \tag{2.25}$$

$$= \delta C \int_0^L \Big(\alpha(x) - \beta(x)\Big) \exp\left(\frac{V(x)}{k_B T} - \frac{\delta\nu}{k_B T} \int I_0^2 \left(\frac{f(x)}{k_B T}\right) \Big(\beta(x) - \alpha(x)\Big) dx\right) dx + O(\varepsilon). \tag{2.26}$$

The integral expression for the approximation of motor velocities given in eq. (2.26) contains a fast oscillating term in the integrand, which creates difficulties in numerical calculations. We can further simplify the velocity expression by deriving an approximation for $v_0(x)$ using a modification of the method of averaging [8].

To find the velocity, we want to solve the initial value problem

$$\frac{dV(x)}{dx} = \delta\Big(\alpha(x) - \beta(x)\Big) p_0(x), \tag{2.27}$$

$$V(0) = 0, \tag{2.28}$$

where we are interested in evaluating $V(L)$.

Using the same rescaling for space with $x = Xy$, we again introduce the fast and slow variables, $y = z$, $\sigma = \dfrac{y}{\varepsilon}$. With this change of variables the problem reads

$$\frac{dV(z,\sigma)}{dz} = \delta\Big(\alpha(z) - \beta(z)\Big) p_0(z,\sigma), \tag{2.29}$$

$$V(0) = 0. \tag{2.30}$$

We now assume a solution of the form $V(z,\sigma) = V_0(z) + \varepsilon V_1(z,\sigma)$ with $V_1(z,\sigma)$ periodic in σ. Notice that $V_0(z)$ represents the mean field so that $V_1(z,\sigma)$ has zero mean in z. Substituting the expansion into eq. (2.29) and retaining the O(1) terms yields

$$\frac{dV_0(z)}{dz} + \frac{dV_1(z,\sigma)}{d\sigma} = \delta\Big(\alpha(z) - \beta(z)\Big) p_0(z,\sigma). \tag{2.31}$$

Recalling that V_1 is periodic in σ it follows that

$$\int_0^\sigma \left(\frac{\partial V_0(z)}{\partial z} + \frac{\partial V_1(z,\eta)}{\partial \eta}\right) d\eta = \frac{\partial V_0}{\partial z}\sigma, \tag{2.32}$$

which in turn produces

$$\frac{\partial V_0(z)}{\partial z} = \frac{1}{\sigma}\int_0^\sigma \delta\Big(\alpha(z)-\beta(z)\Big)p_0(z,\eta)d\eta = \delta\Big(\alpha(z)-\beta(z)\Big)\overline{p_0(z,\sigma)}. \tag{2.33}$$

Substituting $\sigma = 1$, we obtain the first order approximation to the solution

$$\begin{aligned}\frac{dV_0(z)}{dz} &= \delta\Big(\alpha(z)-\beta(z)\Big)\exp\left(\hat{r}(z)-\alpha_2\int I_0^2\left(\hat{f}(z)\right)\Big(\hat{\beta}(z)-\hat{\alpha}(z)\Big)dz\right)\times \\ &\int_0^1 \exp\left(\hat{f}(z)\cos(2\pi\sigma)\right)d\sigma.\end{aligned} \tag{2.34}$$

We immediately recognize that the integral expression in eq. (2.34) is the integral form of the modified Bessel function of the first kind, $I_0(\hat{f}(z))$, therefore we can now write an explicit solution for the velocity of the coupler,

$$\begin{aligned}v &= V(L) \\ &= \delta\int_0^L\Big(\alpha(x)-\beta(x)\Big)\exp\left(\frac{r(x)}{k_BT}-\frac{\delta\nu}{k_BT}\int I_0^2\left(\frac{f(x)}{k_BT}\right)\Big(\beta(x)-\alpha(x)\Big)dx\right)\times \\ &\quad I_0\left(\frac{f(x)}{k_BT}\right)dx + O(\varepsilon).\end{aligned} \tag{2.35}$$

Next, we observe that the approximate solution, $p_0(x)$, is the steady-state solution of the Fokker-Planck equation,

$$\begin{aligned}\frac{\partial p_0(x,t)}{\partial t} &= -\frac{1}{\nu}\frac{\partial}{\partial x}\left[\Big(V'(x)-\delta\nu I_0^2\left(\frac{f(x)}{k_BT}\right)\Big(\beta(x)-\alpha(x)\Big)\Big)p_0(x,t)\right] \\ &\quad + D\frac{\partial^2}{\partial x^2}p_0(x,t),\end{aligned} \tag{2.36}$$

with appropriate boundary conditions. Thereby, by setting out to derive an asymptotic approximation, we have also gained a reduction of the jump-diffusion motor model into a simpler drift-diffusive model. The advantage of this approach is that for the approximate drift-diffusive process we can not only calculate the velocity explicitly, but also the mean first passage time problem is greatly simplified and can be obtained analytically. In what follows, we derive analytical solutions for the mean first exit time calculation starting with the approximate drift-diffusion model.

From the Fokker-Planck equation given in eq. (2.36), we obtain the following ordinary differential equation for the first passage time $T(x)$ at $x = 0$,

$$\frac{1}{\nu}\left(V'(x)-\delta\nu I_0^2\left(\frac{f(x)}{k_BT}\right)\Big(\beta(x)-\alpha(x)\Big)\right)\partial_x T(x)+D\partial_x^2 T(x)=-1 \tag{2.37}$$

with boundary conditions $T(0)=0$, $T'(L)=0$ as before. Note that since the delay terms do not appear in this case, we can use direct integration to obtain the solution for the mean first exit time

$$T(x)=\frac{1}{D}\int_0^x \exp\left(-\frac{V(y)}{k_BT}+\frac{\delta\nu}{k_BT}\int I_0^2\left(\frac{f(y')}{k_BT}\right)\Big(\beta(y')-\alpha(y')\Big)dy'\right)\times \tag{2.38}$$
$$\int_y^L \exp\left(\frac{V(z)}{k_BT}-\frac{\delta\nu}{k_BT}\int I_0^2\left(\frac{f(z')}{k_BT}\right)\Big(\beta(z')-\alpha(z')\Big)dz'\right)dzdy.$$

The underlying assumption for our asymptotic approximation so far has been that ε is sufficiently small in order for our approximate solutions to be accurate. Recall, that $\varepsilon=\frac{b}{k_BT}$, which means that b has to be small and since $b=ka$, the parameter k must be small. This conclusion is in agreement with our intuition, since the jump-diffusion process we started with can only be expected to reduce to a diffusive process we obtained in eq. (2.36) if the unit activation barrier in the $\Psi(x)$ term is sufficiently small, so that the diffusive steps can overcome the Poisson noise. As we show below, $k=10^{-3}$ is sufficiently small for our diffusive approximation to exactly match the numerics of the full jump-diffusion model.

In Figure 2.9, we have plotted a comparison between the approximate steady-state solutions, $p_0(x)$ and the histograms we obtained numerically in the previous section for $k=0.001$ for both a polymerizing and depolymerizing motor. As it can be seen from Figure 2.9, our analytical steady-state solutions are in very good agreement with the numerical simulation of the full jump-diffusion model for small k.

Next, a comparison between the load-velocity relationships from eq. (2.26) and the numerical calculations for the velocity presented in the previous section is given in Figure 2.10A.

From Figure 2.10A, we see that for small barriers with $k=0.001$, the analytic solution v_0 is in excellent agreement with the numerical results obtained for the full jump-diffusion model. This approximation remains in very good agreement for $k=0.01$, however the plot is not shown for clarity as these plots overlay with one another. For $k>0.01$, the diffusive limit solutions lose their accuracy and thus cannot be used to compare with the numerical calculations. Further, in panel B of Figure 2.10 we see that the averaged velocity expression

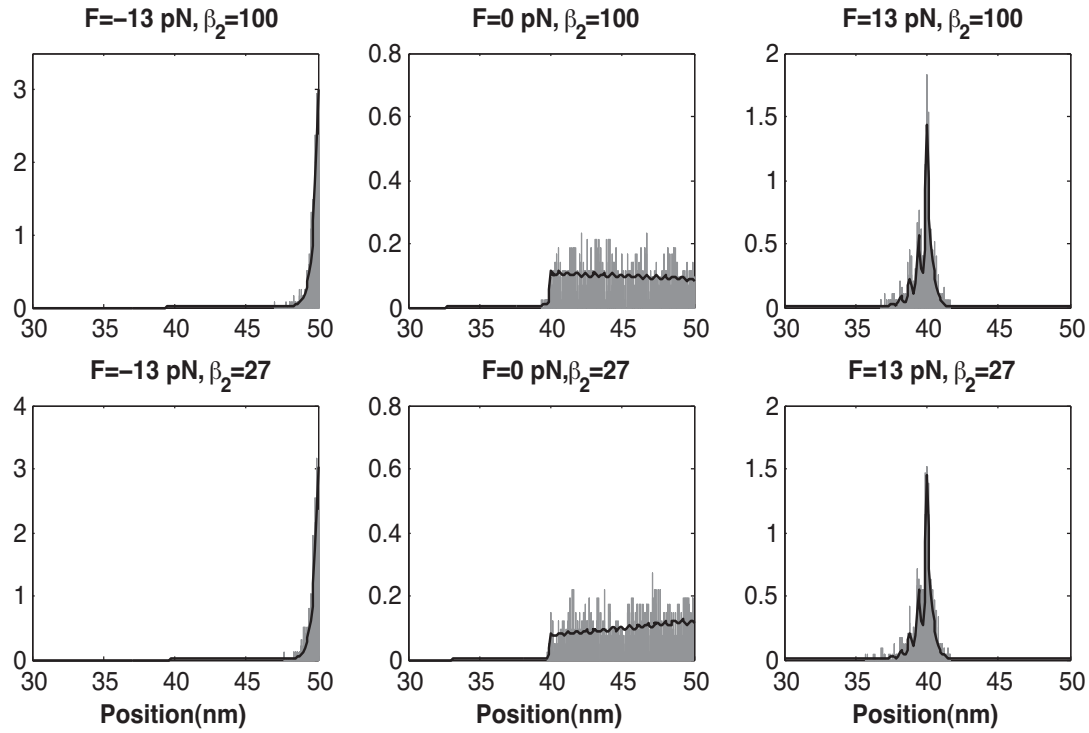

Figure 2.9. A comparison of the numerical versus the analytical steady-state distributions for the diffusive approximation of the steady-state probability density function for varying loads, F, and $k = 0.001$.

in eq. (2.35) is in very good agreement with eq. (2.26) for $k = 0.001$ and is also a good approximation for $k = 0.01$.

In Figure 2.11A-C, we have plotted the mean first exit time solution in eq. (2.38) for varying force terms, F with respect to the initial position, x. Notice from the plots that it takes a very long time for the tip to leave the coupler for small pulling forces and thus we consider the system to have reached a metastable state in panels A and B of Figure 2.11. However, for larger pulling loads (panel C) the exit times decrease significantly indicating that the forces are approaching the breaking loads for the motor. Thus, the mean first exit time calculation in the diffusive limit allows us to analytically determine breaking loads.

In Figure 2.11D, we show a log-log plot of first exit times through $x = 0$ starting from $x = L$, with respect to varying load, F. From Figure 2.11D we observe that our numerical results from section 3.1 and the analytical solution for the exit times in eq. (2.38) agree well with each other. Furthermore, panel D shows that our mean first exit time approximation

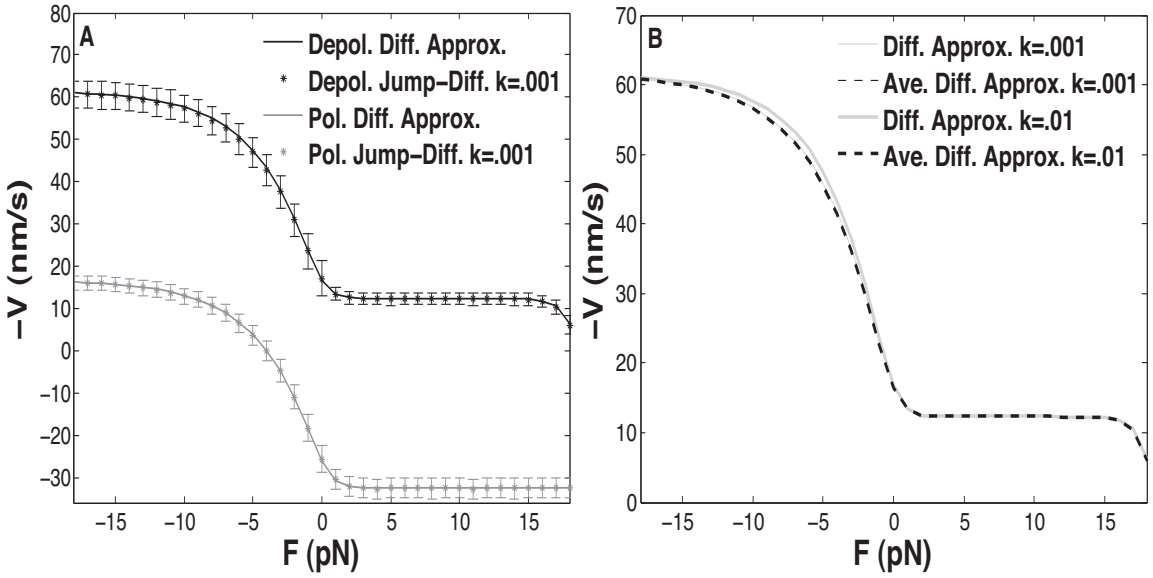

Figure 2.10. **A**. Load-velocity relationship comparison between the diffusive approximation $v_0(x)$ and the Monte Carlo simulations for $k = .001$ for a depolymerizing and polymerizing motor. For the numerical simulations, bars represent the standard deviation. **B**. Load-velocity relationship comparison between the diffusive approximation load-velocity relationship as given in eq. (2.26) and the averaged velocity in eq. (2.35) for $k = 0.001$ and $k = 0.01$.

experiences a sharp decline in exit times past $F = 18$ pN in agreement with our numerical results for breaking loads.

In conclusion, in this section we have shown that for small k, analytical expressions for the force-velocity relation can be obtained which are in good agreement with our numerical simulations. The parameter range for which we obtained analytical approximate solutions falls within the range of experimental predictions for kinetochore binding. Recent measurements of the diffusion coefficients of several microtubule binding proteins which are involved in Kt-MT binding seem to indicate that their activation energy for MT binding is indeed very low [17] and thus the diffusive limit we explore here might be a good approximate model for the interaction of the kinetochore coupler with a dynamic microtubule polymer.

2.4 Off-Register well

So far, we have discussed the case when the spacing of Kt binders is an integer multiple of the binding site spacing on the MT lattice, δ. However, the exact geometry of the Kt binder elements on the attached MT lattice is not yet known. Therefore, alternate scenarios

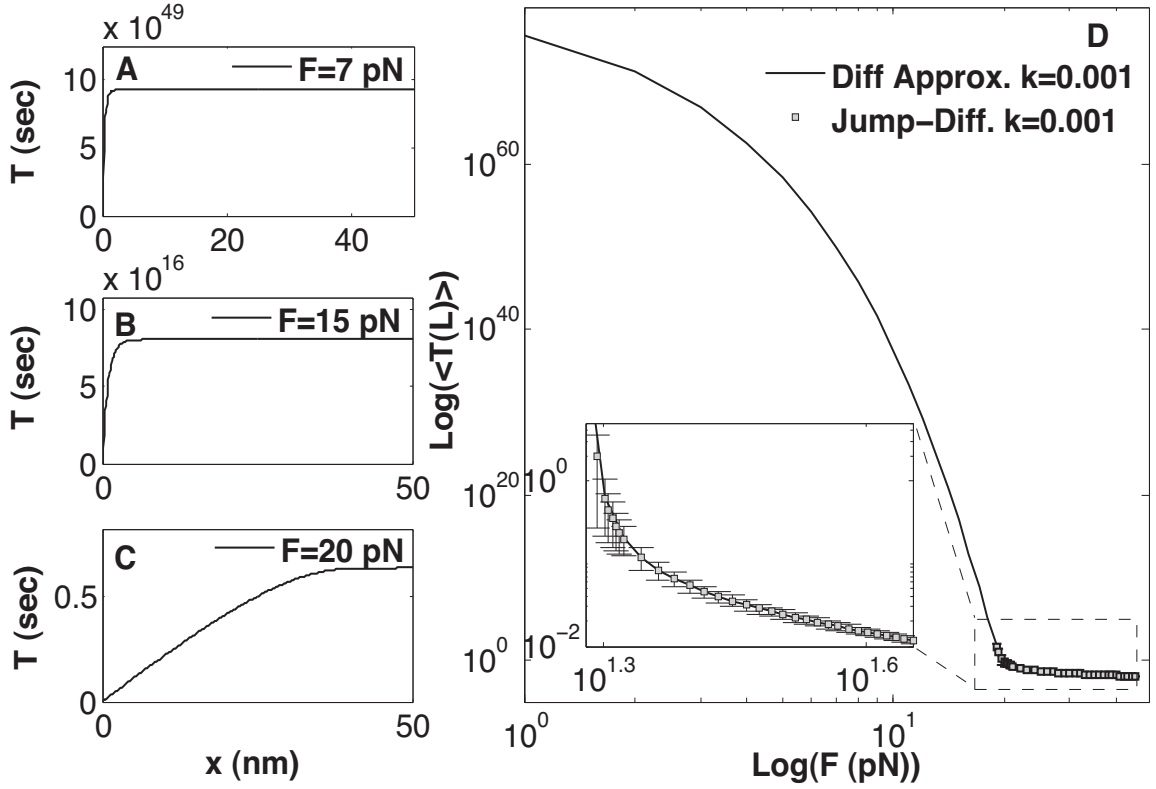

Figure 2.11. Mean first exit time calculation for the approximate diffusive model for $k = .001$. **A.** Mean time for exit, $T(x)$ from the boundary $x = 0$ starting from x, measured in sec for F=7 pN. **B.** Mean time for exit for F=15 pN. **C.** Mean time for exit for F=15 pN. **D.** Log-Log plot of mean first passage time through $x = 0$ starting from $L = 50nm$ versus motor load F. Inset. Comparison of the analytical solutions with the numerical results.

for the spacing between Kt linkers must be considered. If the kinetochore binders are not in-register with the binding sites on the polymer, then the Kt bound coupler linkers need not be all detached for a new attachment to be established. As a result, the geometry of the potential well is altered and two well parameters are important: s the linker spacing which establishes the period of free energy drops due to binding events in the well, and δ which establishes the period of transitions between the individual activation barriers. In the remainder of this chapter, we examine the case in which the linkers are spaced with distances that are not integer multiples of δ with $s = \bar{\kappa}\delta = \delta/\kappa = 3\sqrt{2}\delta/2$: the off-register well case.

We use a Fourier series approximation for the off-register well $\Psi(x)$, which reads

$$\Psi(x) = \begin{cases} -aC_1 \sin\left(\dfrac{2\pi x}{s}\right) + bC_2 g(x) - bC_3 \cos\left(\dfrac{2\pi x}{s}\right) + h(x) & x \leq N_2 s \\ -bC_3 + bC_2 g(x) + h\left(N_2 s\right) & x > N_2 s, \end{cases} \tag{2.39}$$

with $h(x) = -0.5aC_{20}x$ and $g(x) = \cos\left(2\pi(x - (N_2 + 1/2)s)/\delta\right) - \cos\left(2\pi(x + s/2/\delta\right)$. The coefficients from the approximation are: $C_{20} = 1.5$, $C_1 = 0.17$, $C_2 = 2.7$, $C_3 = 0.01$.

2.4.1 Numerical calculation of force-velocity relations

The steady-state expression in eq. (2.7) with the well function of eq. (2.39) can be solved numerically using Monte-Carlo simulations we described in section 3.1. The new well shape significantly affects how the motor responds to increases in individual activation barriers, b.

Numerical solutions for the steady-state distributions with the off-register well are shown in Figure 2.12 and Figure 2.13. For all the values of k that we consider in our study, the numerical solutions for the steady-state distributions settle at the lowest energy state of the potential well for both a polymerizing and depolymerizing off-register motor as shown in Figure 2.12 and Figure 2.13. Recall that the forces, F, change the well tilt and thus affect the position of the lowest energy state in the well, thereby we see shifts on the x-axis as the motor loads are varied. These steady-state results are quite different from what we saw for the in-register well in the previous section where high k values affected the steady-state histograms. This is due to the new well shape which does not hinder diffusion of the kMT tip to the lowest binding energy state since the increases in the individual barriers are not amplified significantly as the overlap increases.

Next, we numerically determine motor velocities for various motor loads at steady-state. In Figure 2.14 we have plotted the force-velocity relation for the motor with the off-register well for different values of the parameter k. The plots are obtained using Monte-Carlo simulations as in section 3.1. We observe that there are some differences in motor response when the well function is altered to be off-register. Namely, the force-velocity relations do not show a slow down in velocity as we increase the value of the parameter k. This is to be expected, since the new topology of the well changes how the steady-state histograms respond to variations in the value of k, as we saw in Figure 2.12 and Figure 2.13. For all the k we have tested here the steady-state distribution histograms experience shifts on the x-axis and accordingly the force-velocity curves show flat regions corresponding to loads that cause shifts in regions where the net balance of rates is unchanged. As a result, both a

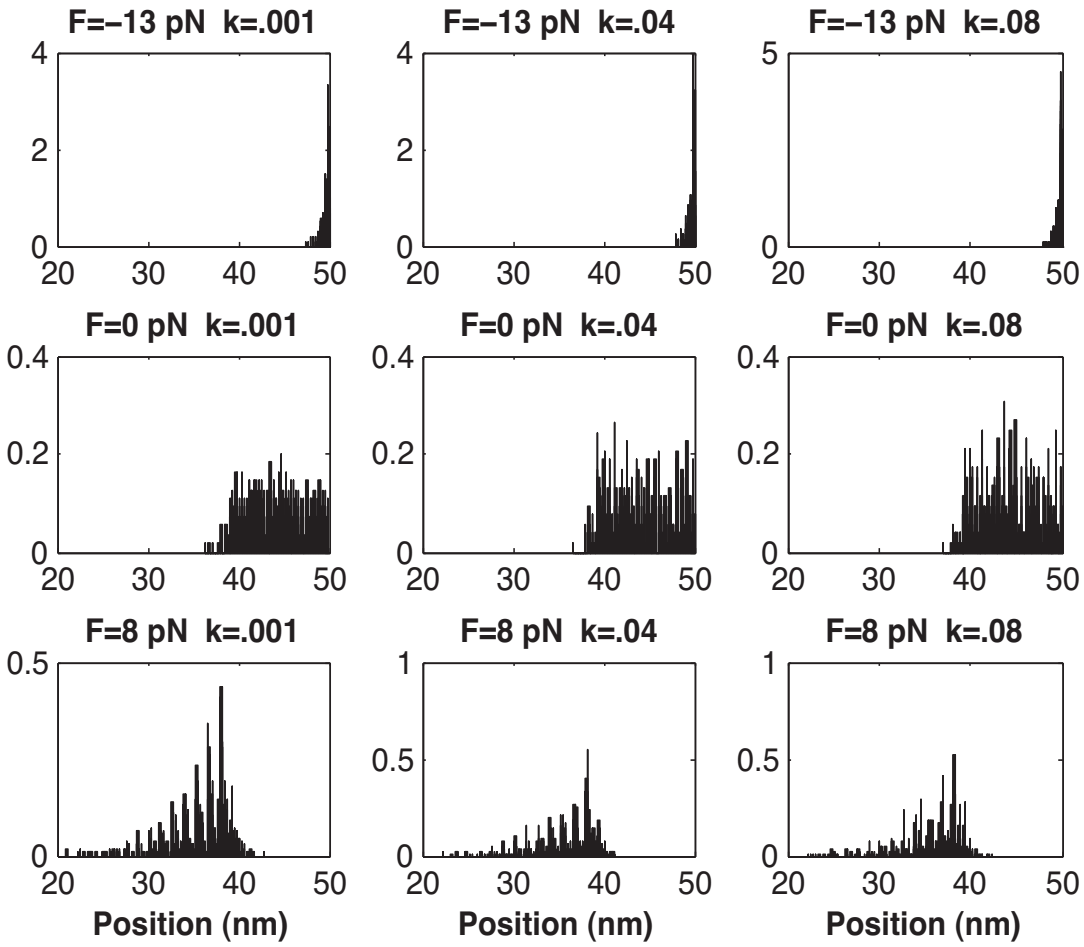

Figure 2.12. Off-register well normalized histograms of the numerical simulation results with varying activation barriers and motor loads for a depolymerizing motor with $\beta_2 = 100\text{s}^{-1} > \alpha_0 = 80\text{s}^{-1}$. Each histogram is generated by gathering simulation statistics for 1000 trials after relaxation into steady-state.

polymerizing and depolymerizing motor with an off-register well can only display a slippery or "floating grip" velocity mode.

Finally, the change of the well function also causes the breaking loads for the system to decrease. This is because with the given value of s we can only fit about half the number of binders on the MT lattice when the coupler is fully engaged (note that $F \leq 8$ pN in Figure 2.14). Since the motor breaking load needs to overcome the total energy of binding to detach a coupler, a reduction in the total amount of binders results in a decrease in the amount of load required to detach the MT polymer from the Kt.

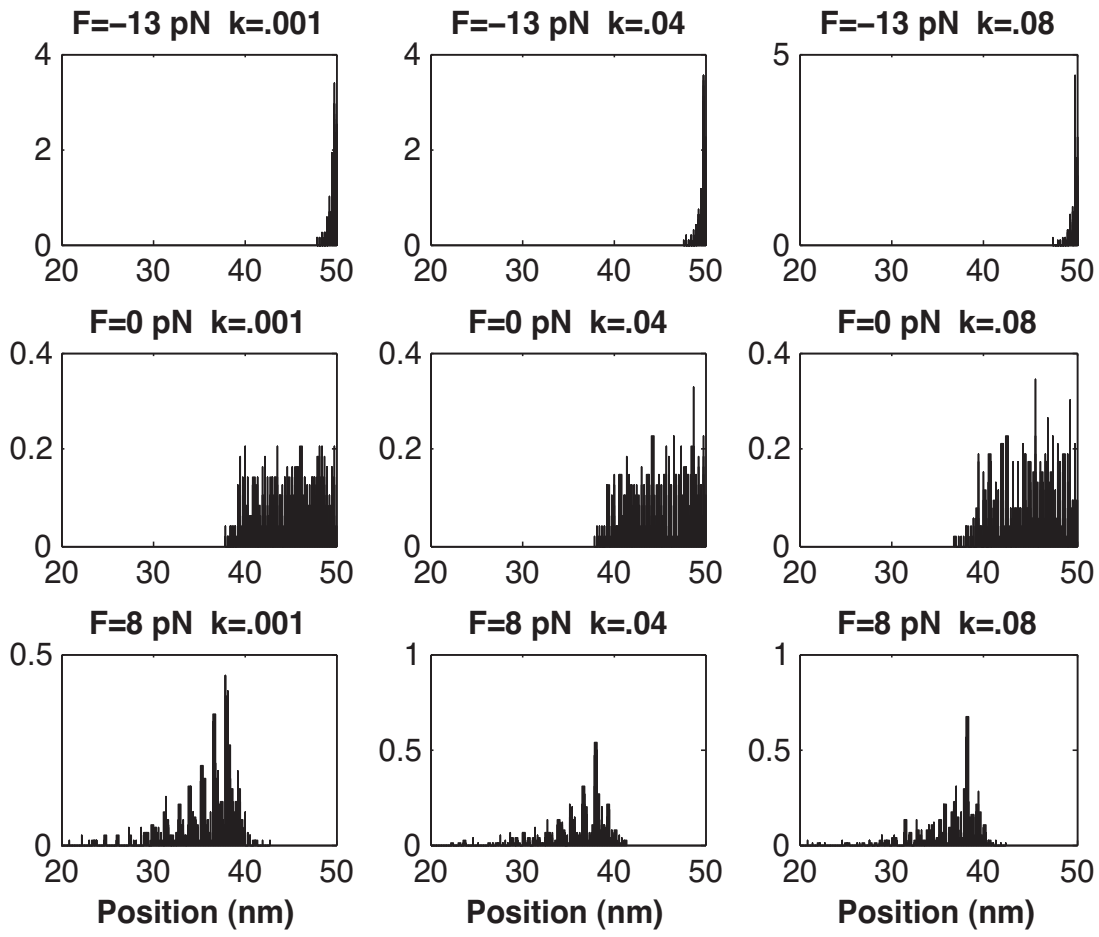

Figure 2.13. Off-register well normalized histograms of the numerical simulation results with varying activation barriers and motor loads for a polymerizing motor $\beta_2 = 27\text{s}^{-1} < \alpha_0 = 80\text{s}^{-1}$. Each histogram is generated by gathering simulation statistics for 1000 trials after relaxation into steady-state.

2.4.2 Asymptotic approximation

The simulations of the off-register case indicate that the motor remains in the slippery regime despite changes in the unit activation barrier values. Based on our previous calculations, we expect that in the off-register case the drift-diffusion approximation can be a good model approximation for a wider range of k values. Accordingly, in this section, we repeat the homogenization argument for the off-register well in order to derive analytic expressions for the force-velocity relation.

We repeat our steps from section 3.4 with the off-register well. After integrating once with the no-flux boundaries, the steady-state equation with the new well function yields

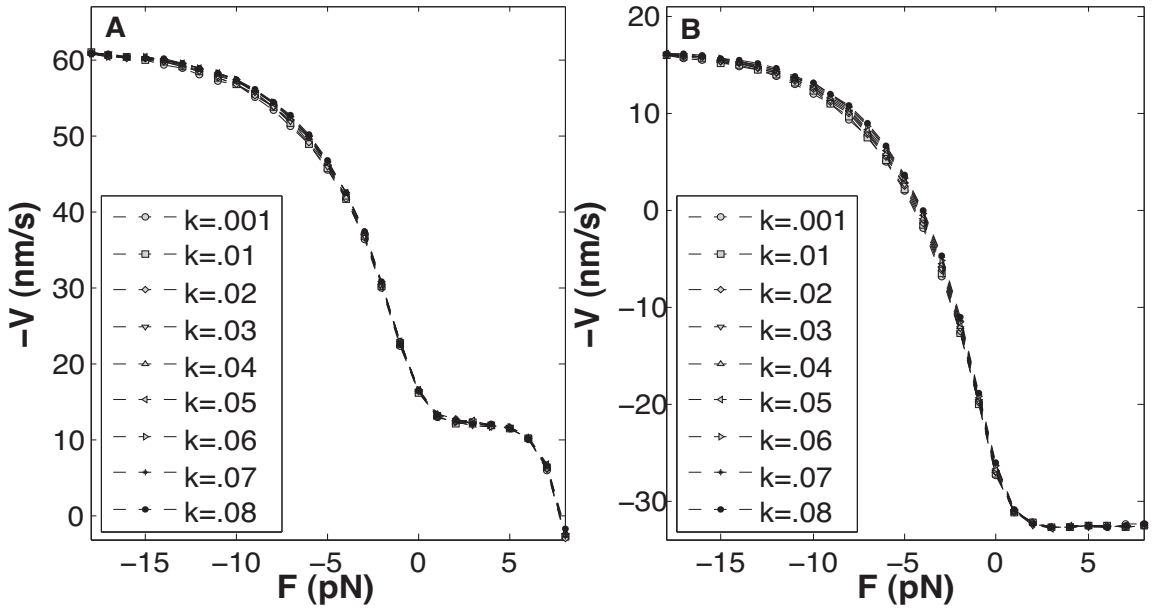

Figure 2.14. Numerical load-velocity relationships for varying k for the off-register well. **A**. Force-velocity calculations for a depolymerizing motor with $\beta_2 = 100\text{s}^{-1} > \alpha_0 = 80\text{s}^{-1}$. **B**. Force-velocity calculations for a polymerizing motor with $\beta_2 = 27\text{s}^{-1} < \alpha_0 = 80\text{s}^{-1}$.

$$0 = -\frac{1}{\nu}\left(aC_1 \sin\left(\frac{2\pi x}{s}\right) - bC_2 g(x) + bC_3 \cos\left(\frac{2\pi x}{s}\right) + r(x)\right)' p(x) + Dp_x(x) \qquad (2.40)$$
$$+ \sum_{n=1}^{\infty} \frac{\delta^n}{n!} \frac{d^{n-1}}{dx^{n-1}} \left(\Big(\beta(x) + (-1)^n \alpha(x)\Big) p(x) \right),$$

where $r(x) = -h(x) - Fx$.

As before, we rescale space by setting $x = Xy = \nu D\delta b/y$ and eq. (2.40) reads

$$0 = -\left(\frac{aC_1}{k_B T} \sin(2\pi\kappa\sigma) - \varepsilon C_2 g(2\pi\sigma) + \varepsilon C_3 \cos(2\pi\kappa\sigma) + \hat{r}(y)\right)' p(y) + p_y(y) \qquad (2.41)$$
$$+ \alpha_2 \sum_{n=1}^{\infty} \frac{\varepsilon^{n-1}}{n!} \frac{d^{n-1}}{dy^{n-1}} \left(\Big(\hat{\beta}(y) + (-1)^n \hat{\alpha}(y)\Big) p(y) \right).$$

This time, we assume the existence of a solution with the expansion $p(y) = p_0(y,\sigma) + \varepsilon p_1(y,\sigma) + O(\varepsilon^2)$, where we now require $p_1(y,\sigma)$ to be a bounded function. In accordance with our previous derivation we introduce two spatial variables: a "slow" variable $z = y$ and a "fast" variable $\sigma = \dfrac{y}{\varepsilon}$.

The hierarchy of equations after substituting the assumed asymptotic solution expansion into eq. (2.41) is

$$O\left(\frac{1}{\varepsilon}\right) : -\left(\frac{2\pi a C_1}{k_B T}\cos(2\pi\kappa\sigma)\right) p_0(z,\sigma) + p_{0\sigma}(z,\sigma) = 0, \tag{2.42}$$

$$\begin{aligned} O(1) : &-\left(\frac{2\pi a C_1}{k_B T}\cos(2\pi\kappa\sigma)\right) p_1(z,\sigma) + p_{1\sigma}(z,\sigma) - \Big(\hat{r}'(z) - 2\pi C_3 \sin(2\pi\kappa\sigma) \\ &- C_2 g'(2\pi\sigma)\Big) p_0(z,\sigma) + p_{0z}(z,\sigma) + \alpha_2\Big(\hat{\beta}(z) - \hat{\alpha}(z)\Big)\int_0^1 p_0(z,\sigma)d\sigma = 0. \end{aligned} \tag{2.43}$$

First, we see that the solution of the $O\left(1/\varepsilon\right)$ equation can be obtained, as before, by direct integration where we get

$$p_0(z,\sigma) = A_0(z)\exp\left(\frac{aC_1\sin(2\pi\kappa\sigma)}{k_B T}\right). \tag{2.44}$$

Note that $p_1(z,\sigma)$ is only required to be bounded, so after solving the $O(1/\varepsilon)$ equation, we have to check that the $O(1)$ equation indeed satisfies the required boundedness requirement. This last step allows us to obtain an expression for the coefficient $A_0(z)$.

Let,

$$I(z,\sigma) = \exp\left(-\frac{aC_1\sin(2\pi\kappa\sigma)}{k_B T}\right), \tag{2.45}$$

and the $O(1)$ equation can now be written as

$$\begin{aligned} 0 =& \Big(p_1(z,\sigma)I(z,\sigma)\Big)_\sigma + \exp(\hat{r}(z))\Big(p_0(z,\sigma)\exp(-\hat{r}(z))I(z,\sigma)\Big)_z \\ &+ \Big(C_2 g'(2\pi\sigma) + 2\pi C_3\sin(2\pi\kappa\sigma)\Big)A_0(z) + \alpha_2\Big(\hat{\beta}(z) - \hat{\alpha}(z)\Big)A_0(z)I(z,\sigma)I_0\left(\frac{aC_1}{k_B T}\right). \end{aligned} \tag{2.46}$$

where $I_0\left(aC_1/k_B T\right)$ again denotes the integral form of the modified Bessel function of the first kind, this time evaluated at $\hat{f}(z) = aC_1/k_B T$.

So,

$$\begin{aligned} p_1(z,\sigma) =& \frac{-1}{I(z,\sigma)}\int\Bigg(\exp(\hat{r}(z))\Big(p_0(z,\sigma)\exp(-\hat{r}(z))I(z,\sigma)\Big)_z + \Big(C_2 g'(2\pi\sigma) \\ &+ 2\pi C_3\sin(2\pi\kappa\sigma)\Big)A_0(z) + \alpha_2\Big(\hat{\beta}(z) - \hat{\alpha}(z)\Big)A_0(z)I_0\left(\frac{aC_1}{k_B T}\right)I(z,\sigma)\Bigg)d\sigma. \end{aligned} \tag{2.47}$$

Since we are interested in the boundedness of p_1 we examine the following limit

$$\lim_{c\to\infty}\int_0^c \exp(\hat{r}(z))\Big(p_0(z,\sigma)\exp(-\hat{r}(z))I(z,\sigma)\Big)_z + \Big(C_2 g'(2\pi\sigma) + 2\pi C_3\sin(2\pi\kappa\sigma)\Big)A_0(z) + \alpha_2\Big(\hat{\beta}(z)-\hat{\alpha}(z)\Big)A_0(z)I_0\left(\frac{aC_1}{k_BT}\right)I(z,\sigma)d\sigma, \tag{2.48}$$

$$= \lim_{c\to\infty} c\Big(A_{0z}(z) - \hat{r}'(z)A_0(z)\Big) + \alpha_2\int_0^c \Big(\hat{\beta}(z)-\hat{\alpha}(z)\Big)A_0(z)I_0\left(\frac{aC_1}{k_BT}\right)I(z,\sigma)d\sigma + K(z,\sigma), \tag{2.49}$$

$$= \lim_{N\to\infty} (N+\xi)\Big(A_{0z}(z) - \hat{r}'(z)A_0(z)\Big) + \alpha_2\Big(\hat{\beta}(z)-\hat{\alpha}(z)\Big)A_0(z)I_0\left(\frac{aC_1}{k_BT}\right)\int_0^{N+\xi} I(z,\sigma)d\sigma + K(z,\sigma), \tag{2.50}$$

$$= \lim_{N\to\infty} N\Big(A_{0z}(z) - \hat{r}'(z)A_0(z)\Big) + \alpha_2 N\Big(\hat{\beta}(z)-\hat{\alpha}(z)\Big)A_0(z)I_0^2\left(\frac{aC_1}{k_BT}\right) + K(z,\sigma) + O(\xi), \tag{2.51}$$

where $K(z,\sigma) = \Big(C_2 g(2\pi\sigma) - C_3\cos(2\pi\kappa\sigma)\Big)A_0(z) + K_1(z)$ is a bounded term. Also we have decomposed $c = N + \xi$ with $N = [|c|]$ and $0 \le \xi < 1$.

Immediately, we see that in order to bound the $p_1(y,\sigma)$ solution we must take care of the unbounded part of the above limit. We do so by setting

$$-\hat{r}'(z)A_0(z) + A_{0z}(z) + \alpha_2\Big(\hat{\beta}(z)-\hat{\alpha}(z)\Big)A_0(z)I_0^2\left(\frac{aC_1}{k_BT}\right) = 0, \tag{2.52}$$

which gives us the following condition on the coefficient $A_0(z)$,

$$A_0(z) = \exp\left(\hat{r}(z) - \alpha_2 I_0^2\left(\frac{aC_1}{k_BT}\right)\int\Big(\hat{\beta}(z)-\hat{\alpha}(z)\Big)dz\right). \tag{2.53}$$

Notice, the striking similarity of this expression with the expression we derived for the in-register well in eq. (2.21). In contrast to eq. (2.21), for the expression of eq. (2.53) the solution is greatly simplified due to the modified Bessel function, I_0, being evaluated at the specific value $\dfrac{aC_1}{k_BT}$. This results in a constant coefficient multiplying the jump term expansion in the zero order solution in eq. (2.53).

We can now write our approximation for the off-register case as

$$p_0(z,\sigma) = \exp\left(\frac{aC_1\sin(2\pi\kappa\sigma)}{k_BT} + \hat{r}(z) - \alpha_2 I_0^2\Big(\frac{aC_1}{k_BT}\Big)\int\Big(\hat{\beta}(z)-\hat{\alpha}(z)\Big)dz\right) + O(\varepsilon). \tag{2.54}$$

Next, we calculate the approximation for motor velocities using p_0 to obtain

$$\begin{aligned} v &\approx \delta \int_0^L \Big(\alpha(x) - \beta(x)\Big) p_0(x) dx + O(\varepsilon) \qquad (2.55) \\ &= \delta C \int_0^L \Big(\alpha(x) - \beta(x)\Big) \times \\ &\quad \exp\left(\frac{aC_1}{k_B T} \sin\left(\frac{2\pi x}{s}\right) + \frac{r(x)}{k_B T} - \frac{\delta\nu}{k_B T} I_0^2\left(\frac{aC_1}{k_B T}\right) \int \Big(\beta(x) - \alpha(x)\Big) dx \right) dx \\ &\quad + O(\varepsilon). \end{aligned}$$

We can further simplify our analytic solution for the velocity by applying averaging for the velocity expression which gives

$$\begin{aligned} v &\approx \delta \int \Big(\alpha(z) - \beta(z)\Big) \overline{p_0(z,\sigma)} dz + O(\varepsilon) \\ &= \delta C \int_0^L \Big(\alpha(x) - \beta(x)\Big) \exp\left(\frac{r(x)}{k_B T} - \frac{\delta\nu}{k_B T} I_0^2\left(\frac{aC_1}{k_B T}\right) \int \Big(\beta(x) - \alpha(x)\Big) dx \right) \times \\ &\quad I_0\left(\frac{aC_1}{k_B T}\right) dx + O(\varepsilon). \qquad (2.56) \end{aligned}$$

A comparison between the expression obtained for p_0 in eq. (2.54) and the numerical results from the previous section is shown in Figure 2.15.

Similar to the previous homogenization results, from Figure 2.15 we see that the analytical expression for the steady-state solution is in good agreement with numerical results. The main difference for $p_0(x)$ here as compared to the in-register calculation is that the value of k does not affect the approximate steady-state distributions (recall that in eq. (2.23), the term $I_0^2\left(\frac{f(x)}{k_B T}\right)$ depends on the value of the parameter k). Indeed, the independence of p_0 on k is a necessary feature due to the fact that the numerical solutions of the steady-state distributions show no changes as k is varied. Further, this also means that the analytical solutions presented here are a good match to the numerics for all the k values we have examined in this chapter (for clarity, a comparison only for $k = 0.001$ is shown in Figure 2.15).

In Figure 2.16A we show a comparison between the numerical results for the force-velocity relation and our analytic solution from eq. (2.55) (only the numerical solution for $k = .001$ is shown for clarity). The analytical velocity solution is a very good approximation to the numerical solutions for all the values of k we have considered. Similarly, a comparison

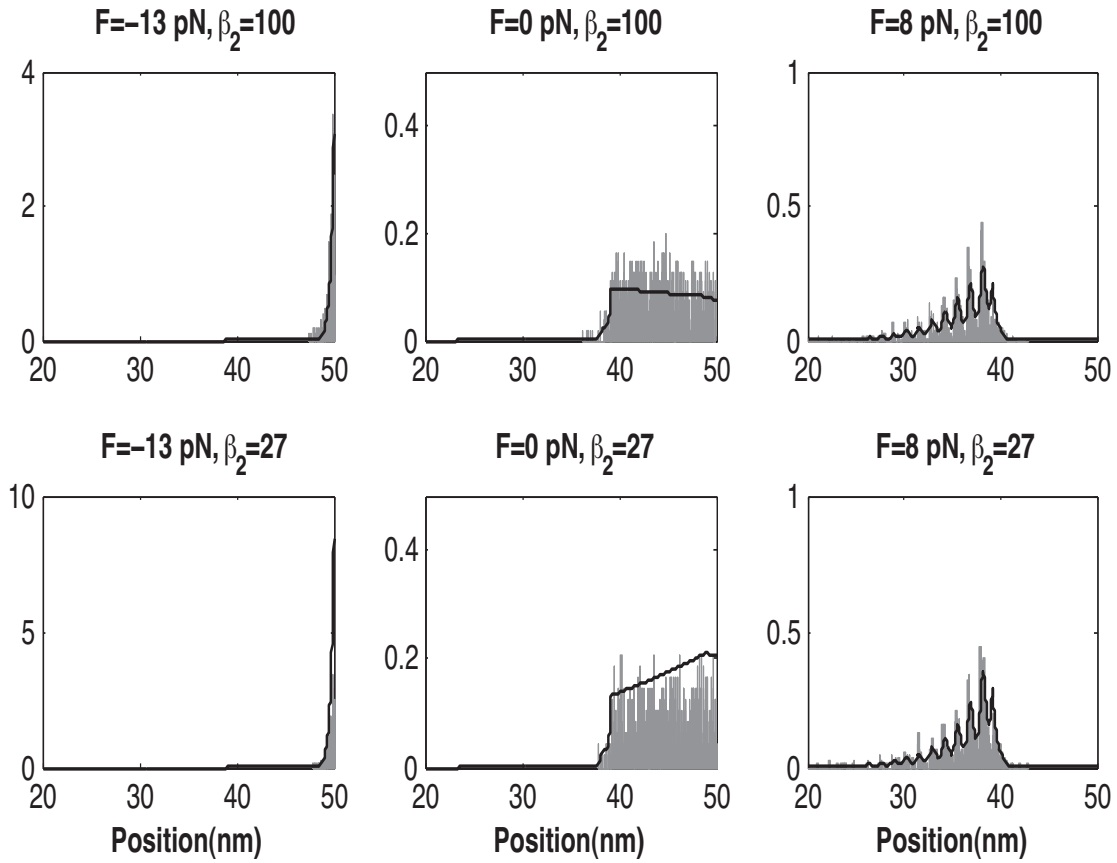

Figure 2.15. Off-register well comparison of the numerical versus the analytical steady-state distributions for the diffusive approximation of the steady-state probability density function for varying loads, F, and $k = 0.001$.

between the averaged solution in eq. (2.56) and the solution in eq. (2.55) in Figure 2.16B shows that the averaged solution is in good agreement with the asymptotic solution and is thus an excellent fast approximation for the force-velocity relation.

In summary, in this section we have calculated analytical expressions for the force-velocity relation for the off-register motor. The solutions obtained are much simpler than the solutions for the in-register well. A distinguishing characteristic in the off-register well case is that the unit barrier amplitudes do not affect the analytic and numeric solutions as opposed to the in-register case, where the value of k significantly affects motor behavior. Therefore, the analytic solutions we obtained in this section are not only strikingly simple but also useful for a much wider range of parameters than in the in-register well case.

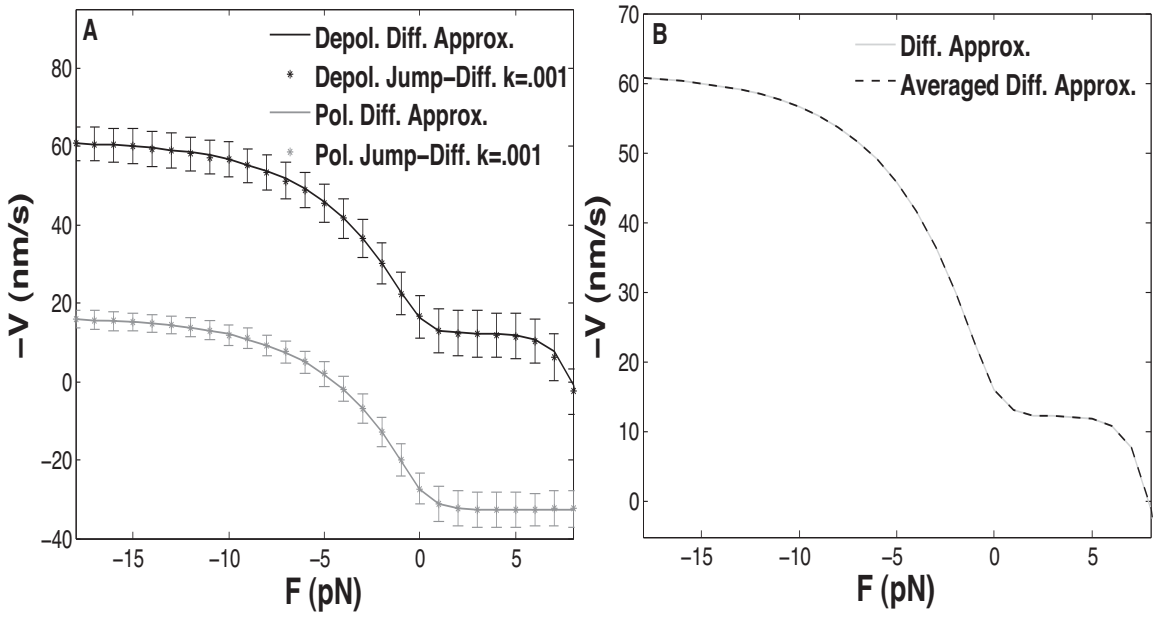

Figure 2.16. **A**. Off-register well load-velocity relationship comparison between the diffusive approximation $v_0(x)$ and the Monte Carlo simulations for $k = .001$ for a depolymerizing and polymerizing motor of the off-register well. For the numerical simulations, bars represent standard deviations from the mean. **B**. Load-velocity relationship comparison between the diffusive approximation load-velocity relationship as given in eq. (2.55) and the averaged velocity in eq. (2.56).

2.5 Conclusions

Understanding the mechanisms underlying the attachment of chromosomes to microtubules presents various challenges due to the dynamic nature of the attached microtubules. Even though many components of this attachment site have been identified, there is no clear understanding of how these components combine with one another to create a motor that can robustly pull significant loads with velocities that depend on the rates of the attached microtubule tip.

In this chapter we have proposed a mathematical model for kinetochore motors. With our model, we can study the effect of the strength of Kt-MT binding on motor velocities as well as the effects of variations in the polymerization/depolymerization rates of the attached kMT. We have also explored two cases for the model: a) the in-register case in which the Kt binder period is an integer multiple of the MT binding site spacing, b) the off-register case in which the binder period is not an integer multiple of binding site spacing. For the in-register scenario we saw that for weak binding with low activation barriers the Kt model can be

reduced to a simple model where closed form expressions for the velocity-force relationship can be obtained. We observed two modes for motor movement: 1) a slippery mode, in which less load could be sustained and the motor moved with velocities that obeyed the balance of kMT rates and, 2) a sticky mode, in which the motor becomes almost static; however the threshold for breaking loads increases. In the slippery mode, motors respond with velocities which are mostly insensitive to loads, since load variation for this motor results in coupler repositioning on the MT lattice, which preserves constant velocities as long as the new equilibrium position allows for the net rate of polymerization/depolymerization to remain constant. We also showed that variations in the kMT depolymerization rate for low unit activation in binding produce shifts in the force-velocity relationship, which depending on the balance of kMT rates can lead to a direction change for the motor. This last feature is particularly important for our motor in the larger chromosome movement context.

In the off-register case we saw many of the characteristics observed for the in-register well. The main difference in this model scenario is the motor's reaction to variations in the unit activation barrier. Whereas the in-register case penalized the increased overlap between the coupler and the polymer, the off-register case penalty in free energy is much smaller. As a result in the off-register case the motor only displays the slippery mode with no slow down as the unit activation barrier energy increases. This finding pointed us to the scenario that if the linkers are not highly organized, there could be an advantage in motor velocities since slow down would require high amounts of energy. Another advantage of the off-register well model is that analytic solutions can be obtained and result into surprisingly simple expressions that produce very good approximations for all the values of the unit activation barriers explored. The analytical approach is extremely valuable for this model both for the in-register and off-register case since numerical simulations are time consuming. Given the current biological data, it is unclear which linker distribution case is operating at the Kt/MT interface. However, if the linkers are not organized into a higher order structure that would impose the same period for the binders as the MT lattice, we suspect that the off-register motor case is a more appropriate kinetochore motor model. In this last scenario, we predict that changes in the Kt binding strength to kMTs caused by the phosphorylation of Ndc80 by Aurora B kinase would have to involve a large energy exchange in order to cause a Kt motor to stall.

Furthermore, in our study we also incorporated polymerization ratchet effects that arise from the MT polymer pushing on the kinetochore plate. We saw that such effects are

important when predicting the motility of kinetochores especially when the motor is subject to large pushing forces.

In conclusion, biased diffusion mechanisms coupled with spatial variations in kMT trip rates produce force-velocity relations which are distinctively nonlinear and are directly dependent upon Kt binding affinities to the MT lattice and the balance of kMT growth/shortening rates. Our kinetochore motor is another example of a motility mechanism which uses the chemical energy of polymerization/depolymerization and the energy of polymer binding to bias thermal motion.

2.6 References

[1] I. M. Cheeseman and A. Desai, *Molecular architecture of the kinetochore-microtubule interface*, Nat. Rev. Mol. Cell Biol., 9 (2008), pp. 33–46.

[2] C. Ciferri, A. Musacchio, and A. Petrovic, *The Ndc80 complex: hub of kinetochore activity*, FEBS Lett., 581 (2007), pp. 2862–2869.

[3] C. W. Gardiner, *Handbook of stochastic methods for physics, chemistry and the natural sciences*, vol. 13 of Synergetics, Springer-Verlag, Berlin, third ed., 2004.

[4] E. L. Grishchuk and J. R. McIntosh, *Microtubule depolymerization can drive poleward chromosome motion in fission yeast*, EMBO J., 25 (2006), pp. 4404–4408.

[5] T. L. Hill, *Theoretical problems related to the attachment of microtubules to kinetochores*, Proc. Natl. Acad. Sci. USA, 82 (1985), pp. 4404–4408.

[6] A. P. Joglekar, K. S. Bloom, and E. D. Salmon, *Mechanisms of force generation by end-on kinetochore-microtubule attachments*, Curr. Opin. Cell Biol., 22 (2009), pp. 1–11.

[7] A. P. Joglekar and A. J. Hunt, *Simple mechanistic model for directional instability during mitotic chromosome movement*, Biophys J., 83 (2002), pp. 42–58.

[8] J. P. Keener, *Principles of applied mathematics*, Westview Press, Cambridge, MA, transformation and approximation revised ed., 2000.

[9] J. R. McIntosh, E. L. Grishchuk, M. K. Morphew, A. K. Efremov, K. Zhudenkov, V. A. Volkov, I. M. Cheeseman, A. Desai, D. N. Mastronarde, and F. I. Ataullakhanov, *Fibrils connect microtubule tips with kinetochores: a mechanism to couple tubulin dynamics to chromosome motion*, Cell, 135 (2008), pp. 322–333.

[10] T. J. Mitchison and E. D. Salmon, *Poleward kinetochore fiber movement occurs during both metaphase and anaphase-a in newt lung cell mitosis*, J. Cell Biol., 119 (1992), pp. 569–582.

[11] I. M. Molodtsov, E. L. Grischchuk, A. K. Efremov, J. R. McIntosh, and F. I. Ataullakhonov, *Force production by depolymerizing microtubules: a theoretical study*, Proc. Natl. Acad. Sci. USA, 102 (2005), pp. 4353–4358.

[12] R. Nicklas, *The forces that move chromosomes in mitosis*, Annu. Rev. Biophys. Biophys. Chem., 17 (1988), pp. 431–449.

[13] C. S. Peskin, G. M. Odell, and G. F. Oster, *Cellular motions and thermal fluctuations: the brownian ratchet*, Biophys. J., 65 (1993), pp. 316–324.

[14] A. F. Powers, A. D. Franck, D. R. Gestaut, J. Cooper, B. Gracyzk, R. R. Wei, L. Wordeman, T. N. Davis, and C. L. Asbury, *The Ndc80 kinetochore complex forms load-bearing attachments to dynamic microtubule tips via biased diffusion*, Cell, 136 (2009), pp. 865–875.

[15] B. Shtylla and J. P. Keener, *A mechanomolecular model for the movement of chromosomes during mitosis driven by a minimal kinetochore bicyclic cascade*, J. Theor. Biol., 263 (2010), pp. 455–470.

[16] R. V. Skibbens, V. P. Skeen, and E. D. Salmon, *Directional instability of kinetochore motility during chromosome congression and segregation in mitotic newt lung cells: a push pull mechanism*, J. Cell Biol., 122 (1993), pp. 859–875.

[17] L. Wordeman and J. R. Cooper, *The diffusive interaction of microtubule binding proteins*, Curr. Opin. in Cell Biol., 21 (2009), pp. 68–73.

CHAPTER 3

CHROMOSOME MOVEMENT DURING MITOSIS[1]

During mitosis, chromosomes use a complex network of dynamic microtubules to find the cell equator in preparation for division signals. The roles of cellular chemical signals in mechanisms driving mitotic chromosomal movements are not well understood. In this chapter, we propose a mathematical model of this process which incorporates a molecular scale model of kinetochore-microtubule interactions into a negative feedback loop between spindle forces and local kinetochore biochemical reactions. This system allows kinetochore biochemical reactions to control and coordinate chromosome movement, thus providing a direct connection between mechanical signals and mitosis chemical species. Our feedback control model can recreate chromosome movement from prometaphase to anaphase in good agreement with experimental data.

3.1 Introduction

The movement of chromosomes to the cell equator is one of the most striking mitotic events. Chromosome motility is facilitated by the mitotic spindle, which consists of a complex network of microtubules that nucleate from two poles. The spindle machinery essentially lays out a system of tracks on which chromosomes move. Mechanical linkage between chromosomes and microtubules is provided by proteinaceous structures called kinetochores [3]. Depending on its attachment to the spindle, a chromosome can be in one of two states: monooriented if tethered to microtubules from only one pole, or bioriented if connected to microtubules from both poles.

In many vertebrate cells, monooriented and bioriented chromosomes show oscillatory movements classified as "directional instability" [29]. Oscillatory motility is characterized by periods of motion at approximately constant speeds marked by abrupt switches between

[1]Reprinted from J. Theor. Biol., 263, B. Shtylla, J. P. Keener, A mechanomolecular model for the movement of chromosomes during mitosis driven by a minimal kinetochore bicyclic cascade, pp. 455-470, Copyright (2010), with permission from Elsevier.

motion directed toward and away from a pole [26][29]. We refer to chromosome motion directed toward the closest pole to which it is tethered as poleward motion and motion away from the closest pole as antipoleward (AP) motion. Toward and away from pole movements have been shown to be primarily coupled to Kt associated microtubule (kMT) growth/shortening by tubulin addition/removal at the attachment site [17]. Typically a chromosome becomes first monooriented and travels toward the pole from which the kMT nucleated. Once close to this pole, it experiences directional instability awaiting connections from the opposing pole. After biorientation, motion preserves constant velocities with a bias toward the spindle equator controlled by the duration of poleward and antipoleward trips [29]. At the end of metaphase, chromosomes align at the cell equator and undergo further oscillations.

Poleward chromosome movement results from forces arising at kinetochores. In turn, kinetochore forces could originate from Kt coupling to depolymerizing microtubules or the pulling action of minus-end directed motor proteins. Several motor proteins such as dyneins, CENP-E are found at kinetochores [3]. Even though molecular motor enzymes are likely to contribute to kinetochore tethering to kMTs, their role in generating motion is questioned on the basis that molecular motor depletion in higher eukaryotes does not entirely hinder Kt/kMT interactions [13], and their activity is dispensable for chromosome motility in yeast [10][30]. Therefore it seems reasonable to expect chromosome poleward movement to depend on kinetochore coupling to kMT tip shortening rates.

Interactions between spindle MTs and chromosome arms could be sufficient for antipoleward motion provided that kinetochores are tethered to growing kMTs. Astral microtubules push chromosome arms away from the poles toward the spindle equator creating what are known as “polar ejection” forces [25][26]. The interactions between the spindle and chromosome arms at a given position depend on the density of microtubules there. For equal densities of microtubules emanating from each pole the polar ejection forces should balance half way, at the spindle equator. Therefore, polar ejection forces provide spatial cues which guide chromosomes to the cell equator.

Since movement seems to depend on the coordination of the forces exerted on kinetochores with kMT tip rates, a mechanism for local Kt control that incorporates force dependent kMT tip rate regulation could be sufficient to generate motion. Indeed, local motility control at kinetochores is supported by evidence that chromosomes in the same cell move autonomously with uncoordinated directional switches [26][29]. Also, tension arising

from stretching of sister kinetochores during oscillations has been implicated in controlling transitions from poleward to AP motion [29]. More importantly, there is evidence for a kinetochore force mediated regulatory mechanism based on experiments which have identified Kt associated force sensing proteins that also affect kMT polymerization/depolymerization rates [2][9][15][20][28]. The details of how such a biochemical-force regulatory machinery could work to control chromosome motility are not well understood.

A previous model by [6] studied how kinetochore force sensing affects chromosome motility in yeast where kinetochores only bind a single MT. This study, however, did not specify how kinetochores sustain attachment or address any explicit mechanisms that would integrate mechanical tension with velocity modulation at kinetochores. Recently [16] considered a chemical reaction mechanism for chromosome motility where velocity control was purely chemical with no explicit load dependence or variation in attachment numbers at each kinetochore. While kinetochores seem to operate on flat load velocity curves with velocities insensitive to load variations, any coupler motor would have to eventually adjust its response if loads became too large. We reasoned that these effects could be important in chromosome motility and thus sought to investigate them explicitly in a chromosome motility model.

In this chapter, we develop a model of chromosome movement where velocity is controlled by a negative feedback mechanism between spindle forces and kinetochore localized force dependent chemical reactions. For each chromosome attachment site, we use the Kt coupler model from Chapter 2 to describe the molecular mechanics of the Kt/MT connection. Then, we use the corresponding Kt coupler load-velocity relationships to predict system velocity in response to various Kt loads and kMT tip rates. The proposed feedback mechanism generates independent chromosome oscillations in the monooriented case, and predicts congression and further oscillations in the bioriented state, in good agreement with data.

3.2 Model

In this section we describe model assumptions and equations.

In Figure 3.1 is shown a diagram of a chromosome and of all the forces included in our model that affect its motion. We suppose that chromosome movement is in the horizontal direction along a one-dimensional axis starting from the left pole (at $x = 0$) to the right pole (at $x = L$).

Furthermore, we assume that the motion is viscous dominated (inertia can be neglected) so that

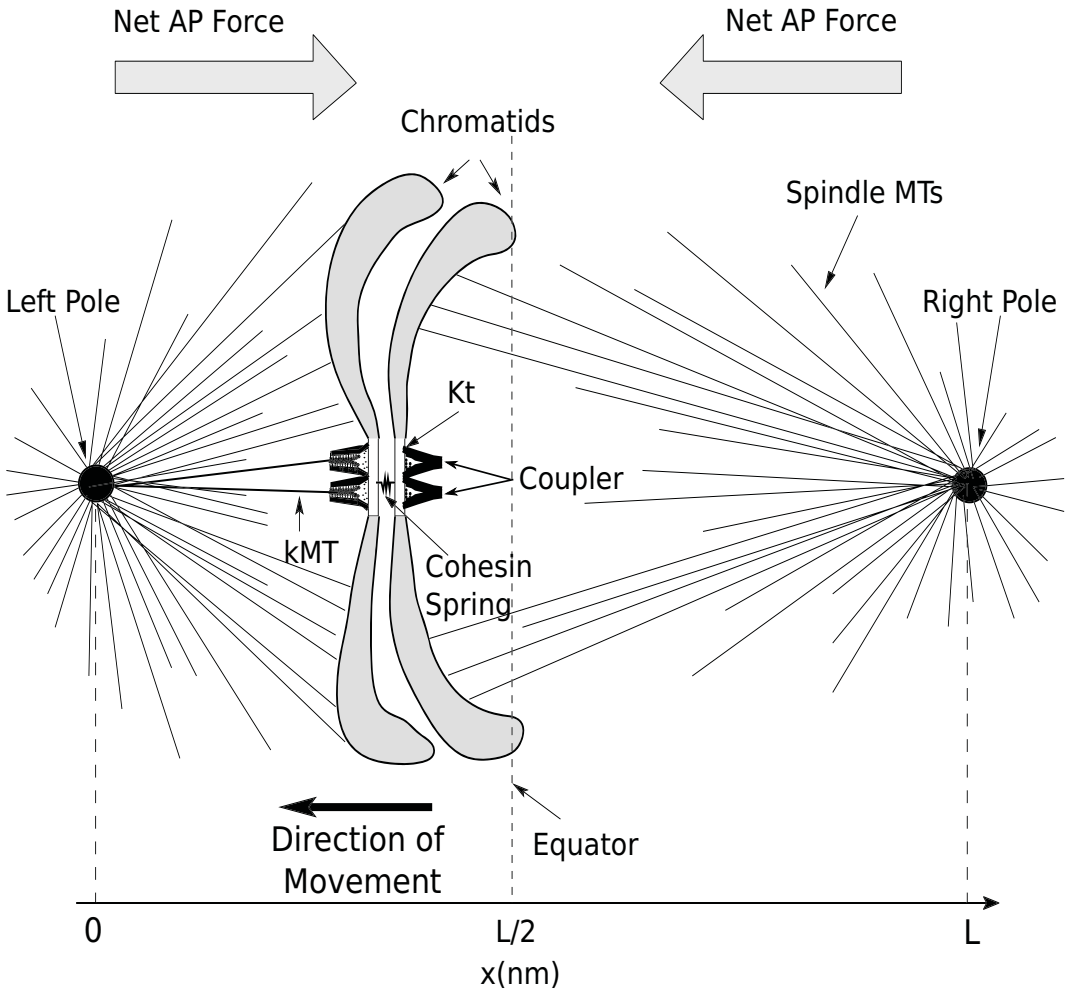

Figure 3.1. Diagram of model components. For ease of illustration we have increased the relative scale of a chromosome in the cell. Polar-ejection forces (shown as large arrows) arise when the chromatids interact with microtubules that nucleate from two poles. These forces are directed away from each pole and thus create a centering effect. Each kinetochore in our model is equipped with up to 20 couplers; for simplicity we have shown only two per sister kinetochore. Sister chromatids are connected by a spring that maintains proper separation. The net polar ejection and spring forces exerted on a chromosome are read by each connected Kt motor that in turn responds with forces and velocities from its load-velocity curve.

$$\nu \frac{dx_j}{dt} = \sum F, \tag{3.1}$$

where x_j is the x-coordinate position of a chromosome arm, ν is the viscosity, and $\sum F$ is the sum of all applied forces. Three types of forces are included in our model. These are: 1) polar ejection forces due to spindle MTs, 2) forces from each kinetochore molecular motor bound to a MT, and 3) forces coming from physical linkage with sister chromatids.

The individual forms for these forces are specified as follows. Polar ejection forces are assumed to arise when MTs interact with chromosome arms. Since these forces are thought to be microtubule density dependent we model their effect using an inverse square distribution law of the form $f_{ap}/x^2 = k_{ap}A_{cc}/x^2$ where A_{cc} is chromosome cross sectional area parallel to the equator and x is chromosome distance from the pole [12][25]. The parameter k_{ap} is a force density term which depends on the number of astral microtubules interacting with chromosome arms.

Kinetochore motor forces are calculated from load-velocity relationships which we derived in the previous chapter. We allow a Kt to bind several MTs, however each binding generates a force corresponding to a single molecular motor. The key motor model result (described below) is that when attached, a motor generates a load (or force) that depends on the motor velocity and the balance of kMT tip polymerization and depolymerization rates, identified by the depolymerization rate β_j.

Finally, cohesin complexes provide physical connection between sister chromatids [32] and are modeled by a linear center spring.

Thus, the positions of the chromatids are governed by the equations

$$\nu \frac{dx_L}{dt} = \frac{1}{2}\left(\frac{f_{ap}}{x_L^2} - \frac{f_{ap}}{(L-x_L)^2}\right) - \sum_i^m F_{sL,i}(-\frac{dx_L}{dt}, \beta_L(t)) + k_{\mathrm{f}}(x_R - x_L - L_k), \tag{3.2}$$

$$\nu \frac{dx_R}{dt} = \frac{1}{2}\left(\frac{f_{ap}}{x_R^2} - \frac{f_{ap}}{(L-x_R)^2}\right) + \sum_i^n F_{sR,i}(\frac{dx_R}{dt}, \beta_R(t)) - k_{\mathrm{f}}(x_R - x_L - L_k), \tag{3.3}$$

where x_j $(j = L, R)$ refers to the position of the chromatid facing the j^{th} pole (Figure 3.1) with n, m the total number of attached right and left kinetochore couplers respectively. $F_{sj,i}$ corresponds to the forces coming from i^{th} motor attached at kinetochore j, and L_k is the cohesin spring relaxed length. For simplicity we have split the anti-poleward forces on each sister chromatid in half.

The next important ingredient of the model are the Kt chemical reactions. We propose

that kinetochores contain a sensor species S which is activated at a force dependent rate subsequent to a microtubule binding a kinetochore. We assume that if S grows above a threshold value, it promotes the phosphorylation of a species A into Ap; if S decays below threshold a phosphatase takes Ap into A. Possible candidates for the sensor are components of the CPC complex and A could correspond to Aurora B (AurB), a kinetochore specific kinase. The members of the CPC complex are thought to first bind and activate AurB via force dependent phosphorylation and subsequently the kinase (auto)phosphorylates to its fully active state [2][27][28]. Since the activation of AurB is not yet completely understood we retain a simplified description where events are grouped into an activation and phosphorylation reaction. Next, the species Ap catalyzes in a threshold dependent way the phosphorylation of a mitotic kinesin, Mc. A candidate for Mc is the kinesin-13 MCAK which is a substrate of AurB at centromeres and is also the most powerful microtubule depolymerase known to date [5][9]. In line with the observation that phosphorylation of MCAK by AurB blocks its activity in vitro and in vivo [1][35] phosphorylated Mc (which we denote by Mcp) is inactive in our model. Figure 3.2 illustrates a wiring diagram for the kinetochore chemical reactions.

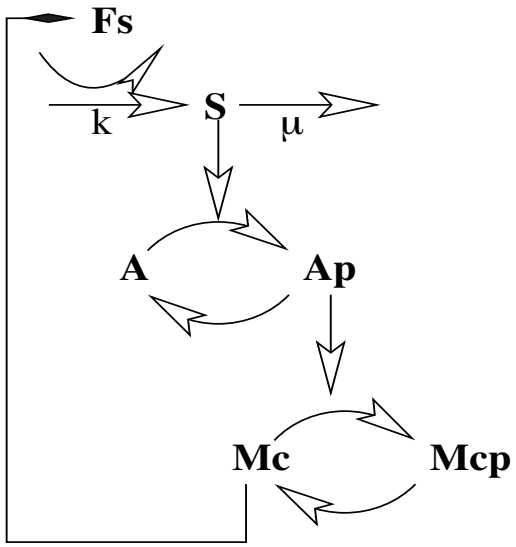

Figure 3.2. Reaction diagram of the negative feedback loop between Kt loads (F_s) and chemical species reactions. Kt loads increase sensor production (S), which in turn initiates a reversible two step phosphorylation cascade between the kinase (A) and kinesin (Mc).

In accordance with the above description, each kinetochore sensor species is activated at a load adaptive rate $k\sum_i F_{sj,i}(\frac{dx_j}{dt}, \beta_j(t))$, and decays with a constant rate μ,

$$\frac{dS_j}{dt} = k\sum_i F_{sj,i}(\frac{dx_j}{dt}, \beta_j(t)) - \mu S_j. \tag{3.4}$$

The two step phosphorylation cascade is modeled using Michaelis-Menten dynamics,

$$\frac{dAp_j}{dt} = \frac{k_A^+ S_j(A_{Tj} - Ap_j)}{K_A + A_{Tj} - Ap_j} - \frac{k_A^- Ap_j}{K_A + Ap_j}, \tag{3.5}$$

$$\frac{dMc_j}{dt} = \frac{-k_M^- Ap_j Mc_j}{K_M + Mc_j} + \frac{k_M^+(M_{Tj} - Mc_j)}{K_M + M_{Tj} - Mc_j}. \tag{3.6}$$

with $M_{Tj} = Mc_j + Mcp_j$, $A_{Tj} = A_j + Ap_j$, the total concentration of species Mc and A at kinetochore j. K_A, K_M are the Michaelis constants for the reactions. The rates k_A^-, k_M^+ characterize phosphatase kinetics whereas $\mathrm{k}_A^+\mathrm{S}_j$, $\mathrm{k}_M^-\mathrm{Ap}_j$ are chosen so that maximum kinase velocities are reached when S and Ap are at their highest values. A similar cascade has been shown to cause limit cycle behavior for the cyclin-cdc2 kinase mitotic oscillator in [7]. The key characteristic of this cascade is that Ap and Mc show zero-order ultrasensitivity (i.e., the reactions display sigmoidal switch-like signal-response curves) so that response increases continuously with signal strength and is fully reversible [8][31].

Further, we assume that the microtubule depolymerization rate β_j at a given kinetochore is related to the amount of Mc available through the linear relationship

$$\beta_j(t) = \frac{\beta_{max} - \beta_{min}}{M_{Tj}} Mc_j + \beta_{min}. \tag{3.7}$$

Notice that the depolymerization rate β_j feeds back into the motor forces through the $F_{sj,i}(\frac{dx_j}{dt}, \beta_j)$ term of eq. (3.2)-(3.3) to report chemical species levels into the force balance calculation. Thus, we have feedback between chemical reactions and kinetochore forces.

Finally, we note here that in general our model is a system of eight nonlinear differential equations, but when one sister kinetochore is not attached (monooriented case) this system reduces to 5 equations since one set of chemical equations has trivial solutions.

3.2.1 Load-velocity relationship for kinetochore motors

For the Kt motors in this model we use the in-register model discussed in Chapter 2. In this section we restate the key equations of the biased diffusion motor for the chromosome movement model. A diagram of the kinetochore motor components is shown in Figure 3.3.

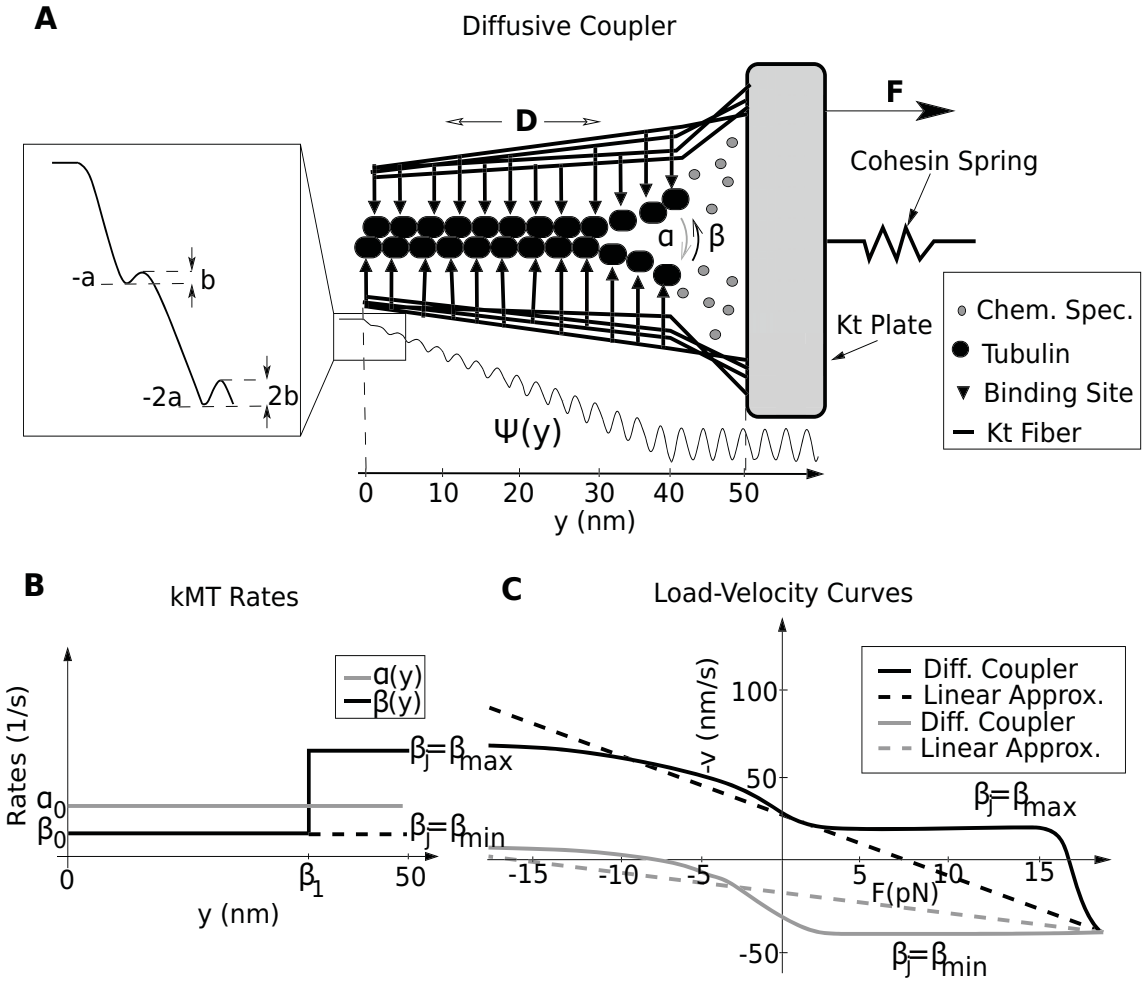

Figure 3.3. Diffusive coupler diagram. (A) Several weak kMT lattice binding sites diffuse on an inserted microtubule with a dynamic tip. The energy of binding is represented by a potential well function $\Psi(y)$ which creates a bias for increased overlap between the kinetochore filaments and the polymer. Motor loads (F) coming from polar ejection forces and the spring oppose the potential well bias for insertion. (B) The polymerization/depolymerization rates for the tip of an inserted MT are position dependent functions. The polymerizarion rate is constant whereas the depolymerization rate is a step function that varies from β_0 to β_j. β_j depends on the concentration of active MCAK at the kinetochore. (C) Load-velocity curves for the diffusive couplers and their respective linear approximation. For the diffusive motors load velocity curves for are mostly flat. The linear load-velicity curves have the same quantiative behavior as the nonlinear load-velocity curves when the rate β_j varies. The rate β_j for the linear curves was chosen to give a good fit to the nonlinear case; all other rate parameters are the same. In this plot $-v > 0$ denotes poleward or depolymerization-driven motion, whereas $-v < 0$ denotes antipoleward or polymerization-driven motion.

Horizontal displacement for the Kt motor is measured with respect to an internal motor frame of reference. The motor position variable, y, marks the distance between the polymer tip and the coupler end distal to the kinetochore plate. Thus, the position axis here starts at the coupler entry point ($y = 0$ nm) and extends to the Kt plate ($y = 50$ nm), as shown in Figure 3.3A. The reason for this new frame of reference is that motor dynamics are directly dependent on the amount of overlap between the polymer and the coupler and not the specific chromosome position in the cell.

To characterize the binding interactions between the coupler and the polymer, we use an explicit in-register energy landscape function, $\Psi(y)$. We suppose that each motor binder can weakly bind to a single monomer (i.e., there is a single binder binding site on each monomer). We position the binding sites so that when the polymer is fully inserted there are 65 occupied binding sites spread along 40 nm of the polymer. In agreement with [11] for an MT with 13 protofilaments with 8 nm long monomers, the binding sites are placed $\delta = 8/13$ nm apart on the y-axis. The components of the motor model are illustrated in Figure 3.3A. The assumptions used to construct the motor model are as follows.

Spindle forces acting on a chromosome as well as spring forces due to cohesins create mechanical stress on kinetochores producing load (F) on the motor. With our sign convention, $F > 0$ pushes on a kinetochore to oppose poleward motion or equivalently pulls the polymer outside the coupler, whereas $F < 0$ favors polymer insertion or poleward motion.

Finally, the tip of the inserted kMT polymer is dynamic and can grow or shorten with prescribed rates that vary with the position of the tip relative to the kinetochore. A plot of the rates is shown in Figure 3.3B. We assume that the depolymerase MCAK is enriched at the coupler end proximal to the kinetochore plate. Hence, we choose a depolymerization rate that depends on the position of the kMT tip relative to the motor (it varies from a basal value β_0 to a maximal value of β_j) and keep the polymerization rate constant (α_0), independent of tip position.

In the viscous-dominated limit, the motor system is described by the forward Chapman-Kolmogorov equation,

$$\begin{aligned}\frac{\partial p(y,t)}{\partial t} = &-\frac{1}{\nu}\frac{\partial}{\partial y}\Big[\big(-\Psi'(y) - F\big)\, p(y,t)\Big] + \alpha(y-\delta)p(y-\delta,t) + \beta(y+\delta)p(y+\delta,t) \\ &- (\alpha(y) + \beta(y))p(y,t) + D\frac{\partial^2}{\partial y^2}p(y,t),\end{aligned} \tag{3.8}$$

where $p(y,t)$ is the probability density function for y, the relative MT tip position. D is the kinetochore diffusion coefficient, ν is the effective kinetochore viscosity and $\alpha(y)$, $\beta(y)$

are position dependent polymerization and depolymerization rates for the kMT tip. Notice that eq. (3.8) includes jump terms coming from the addition or removal of monomers of size δ in addition to diffusion and drift.

For a given depolymerization rate β_j and reasonable loads, a motor sustains attachment to an MT. Since the polymer tip is constantly growing/shortening, attachment produces movement of the motor with respect to the x-axis. Notice, however, that so far, all the coupler equations have been written in terms of the relative position variable, y. Yet, in order to incorporate this motor into the cell we have to measure its movement with respect to the cell's frame of reference, x. The average velocity of an attached motor with respect to the x-axis is calculated as the sum of the average velocity of movement of the MT tip given by the balance between α and β, plus the average velocity of movement of the Kt relative to the kMT tip,

$$\begin{aligned} v(F,\beta_j) = \frac{d}{dt} < x_K >= \frac{d}{dt} < x_p > + \frac{d}{dt} < y >, \\ = \delta \int (\alpha(y) - \beta(y)) p(y,t) dy + \int y p_t(y,t) dy, \end{aligned} \tag{3.9}$$

where x_K, x_P are the Kt plate and MT polymer tip positions respectively in the x frame of reference.

For our chosen parameters, the attractive forces coming from the potential well create a metastable state in which the position of the tip relative to the coupler is fixed. This implies that at steady-state the coupler moves (relative to the x-axis) with an average velocity that equals the balance of kMT tip rates. If we let $p_s(y)$ be the corresponding steady-state probability density (which is obtained by solving eq. (3.8) with left hand side set to zero with appropriate boundary conditions), the velocity expression reduces to

$$v(F,\beta_j) = \delta \int (\alpha(y) - \beta(y)) p_s(y) dy. \tag{3.10}$$

We use eq. (3.10) to determine load-velocity curves for the motors. Two representative load-velocity curves are shown in Figure 3.3C (note that we plot $-v(F,\beta_j(t))$ in the y-axis of these graphs).

The key feature of the load-velocity curves is the wide range of loads for which the velocity is nearly constant. This arises due to the dependence of the steady-state distributions on the force term, F. In Figure 3.4, we show numerical solutions for steady-state distributions. The solutions are shown as normalized histograms representing the steady-state

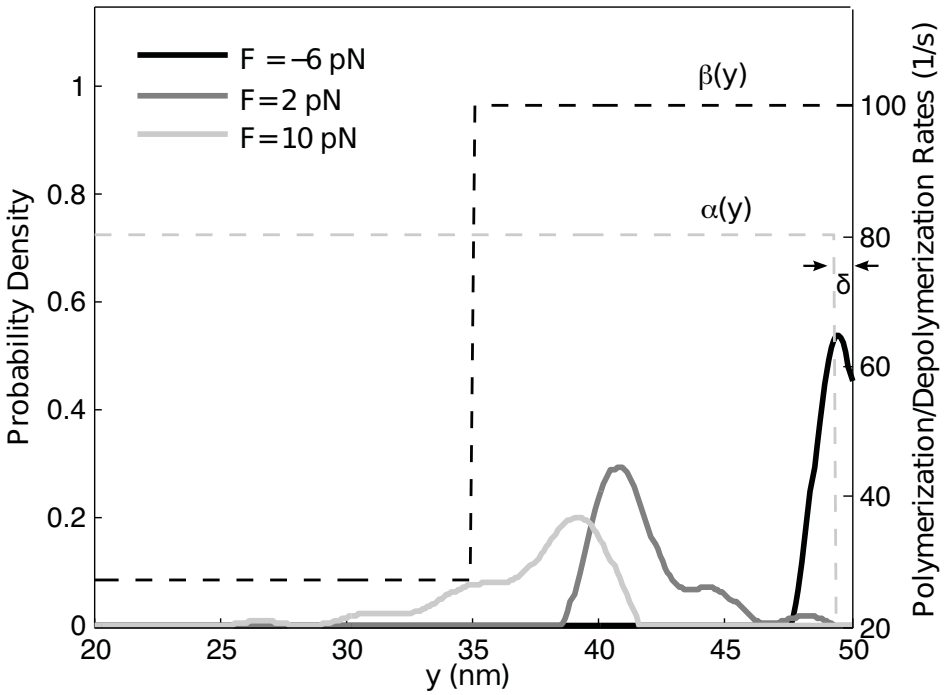

Figure 3.4. Steady-state distributions for various system loads, F, compared with kMT tip growth/shortening rates. For each force value, eq. (3.8) is solved numerically and the histograms (smoothed to eliminate micronscale details) are plotted (solid lines). For these simulations $\beta_j = 100\ \mathrm{s}^{-1}$, and the remaining parameters are the same as in Table 3.1. MT tip polymerization/depolymerization rate functions are shown with dashed lines.

distributions calculated for various amounts of load on the motor. For ease of visualization the microscopic corrugated well effects on the histograms have been filtered out to highlight the macroscopic behavior of the system when the value F is varied. Note from eq. (3.8) that the load term F can act directly to either enhance or diminish the well force effect $\Psi'(y)$ depending on its sign. Consequently, the steady-state distribution for the position of the polymer tip, $p_s(y)$ experiences shifts on the y-axis as a result of changes in the load on the motor. However, notice from Figure 3.3C and Figure 3.4 that the velocity does not change as long as the values of the tip rates in this shifted position remain unchanged. This is due to the fact that the velocity of this motor is determined by the balance of MT growth/shortening rates at the equilibrium tip position. Effectively, the coupler does not change its velocity unless the loads are such that the tip is in the regions where the balance of rates changes. Thus, as in [11], our model provides a mechanism by which the coupler responds to a wide range of loads with constant velocities.

Table 3.1. Parameter Values

Parameter	Description	Value
L	Cell diameter	40 μm [29]
ν	Effective viscous drag coefficient	6 pNs/μm [12]
k	Sensor response rate to load	.02 nM/pNs (estimated)
μ	Sensor decay rate	.5 s^{-1}(estimated)
$k_M^- = k_A^+$	Maximum kinase reaction velocity	.1 s^{-1} [31]
$k_M^+ = k_A^-$	Maximum phosphatase reaction velocity	.2 nM/s [31]
$K_A = K_M$	Michaelis rate constants	.01 nM [7]
L_k	Cohesin spring relaxed length	1000 nm [33]
k_f	Cohesin spring coefficient	.1 pN/nm [12]
α_0	Rate of tubulin subunit addition	80 s^{-1} [12]
β_0	Basal rate of tubulin subunit removal	27 s^{-1} [12]
β_{max}	Max. rate of removal of tubulin	130 s^{-1} (estimated)
β_{min}	Min. rate of removal of tubulin	27 s^{-1} (estimated)
a	Free energy of binding	2.6 k_BT [11]
b	Unit activation barrier	.01 k_BT [24]
D	Coupler diffusion coefficient	690 nm/s^2 [11]
F_{max}	Linear load-velocity curve force factor	18 pN (estimated)

In Figure 3.4 observe that the polymerization rate has to drop to zero when the distance between the polymer tip and the Kt plate is less than δ, since monomers cannot be added unless there is enough space to do so. This imposes a transition to higher motor depolymerization velocities in the load-velocity plot as the polymer is pushed with more force ($F < 0$) against the plate. This is because it is harder for the MT to add monomers against a large pushing load; however depolymerization still proceeds unaffected (see Figure 3.3C). Therefore, in this force regime the motor effectively responds like a polymerization ratchet in agreement with the results of [23]. On the other hand, when the pulling forces ($F > 0$) are significant, parts of the steady-state distributions localize in regions where the polymerization rate is greater than the depolymerization rate. This produces a decline in depolymerization velocities in the load-velocity curves when $\beta_j > \alpha_0$ since in eq. (3.10) there is a contribution in the velocity integral for regions where $\alpha(y) > \beta(y)$. Of course, if the pulling loads increase too much the motor breaks down with the polymer pulled out of the motor. Thus the pulling force range in the velocity calculation must be restricted accordingly.

Finally, we note that the expression in eq. (3.10) cannot be evaluated to find explicit relationships between motor velocity v , the rate β_j and load F. Furthermore, for equations (3.2)-(3.3), we need the load as a function of velocity and β_j, and these equations are implicit rather than explicit equations for chromosome velocity. We can greatly simplify the analysis of our model by replacing the diffusive motor load-velocity curves coming from solutions of (3.8)-(3.10) with explicit relationships that retain key characteristics of the motor. Thus, in addition to solving the full model (numerically) we also explore the behavior of the model when the motor load-velocity relationships are given by the linear equation,

$$F_{sj,i}(v_j, \beta_j) = \frac{2F_{\max}}{\delta(\beta_0 - \beta_j - \alpha_0)} \left(v_j - \frac{\delta(\beta_j + \beta_0 - \alpha_0)}{2} \right). \tag{3.11}$$

A comparison between the load velocity curves of the biased diffusion couplers and the linear equation (3.11) is shown in Figure 3.3C. Notice that the linear curves show the same qualitative behavior as the numerically determined diffusive coupler curves for β_j between $\beta_{\min}$ and $\beta_{\max}$.

3.3 Results

We numerically solved the model equations to track chromosome positions and chemical species levels as functions of time. For the simulations, local kinetochore species concentra-

tions were scaled by S_θ and normalized S_θ=M_{Tj}=$A_{Tj} = 1$. Kinetic and binding parameter values were either taken directly from the literature or estimated from experimental data (see Appendix). A complete list of model parameters is shown in Table 3.1. For the simulations of the system with linear load velocity curves the variables were rescaled and the results are presented in terms of $\chi_j = x_j/L$, $s_j = S_j/S_{\max}$, $a_j = Ap_j/A_T$, $m_j = Mc_j/M_T$, $\tau = t/T$.

3.3.1 Monooriented chromosome oscillations

We first calculated solutions for kinetochores equipped with up to 20 attachments at each kinetochore as suggested by data from newt lung cells [29], then we repeated our calculations with the linear load-velocity curves and analyzed model behavior.

The plots in Figure 3.5 display model solutions for the position of each sister chromatid, sensor, load per motor, and kinase/kinesin levels as a function of time. For these solutions only the left kinetochore is allowed to attach motors to kMTs, i.e., the chromosome is monooriented.

In Figure 3.5A we show the simulated motion of a chromosome with the left chromatid positioned initially at $x = 15$ μm. The left kinetochore is allowed to establish $1 - 2$ new attachments every 100 s. Independent of the initial chromosome position, the model predicts an initial approach to the pole and then movement with very regular poleward and antipoleward excursions with speeds ≈ 1.8 μm/min in each direction (amplitude ≈ 2 μm, period ≈ 3 min) matching experimental observations in newt lung cells [29].

The characteristic constant velocity poleward and antipoleward excursions seen in our simulations are a consequence of the flatness of the load velocity curves on which kinetochore diffusive couplers operate. A load increase results in a shift in the maximal probability for the position of the tip inside the coupler. However, if kMT dynamic rates in this shifted position are unchanged chromosome velocity remains constant. On the other hand, if the depolymerization rate (β_j) is altered, coupler load-velocity curves shift so chromosome velocities change. In our case since Mc controls the depolymerization rate β_j and it quickly switches between either zero or fully active levels, the couplers essentially operate on two load-velocity curves: one where the depolymerization rate is at its highest (depolymerizing movement) and the other where the depolymerization rate is at its basal level (polymerizing movement), see Figure 3.3C.

In Figure 3.5C we plot the load felt by each attached left Kt motor as a function of time. The addition of new attachments redistributes loads by lowering the burden on each coupler. However, this does not affect motion as long as load variations remain within

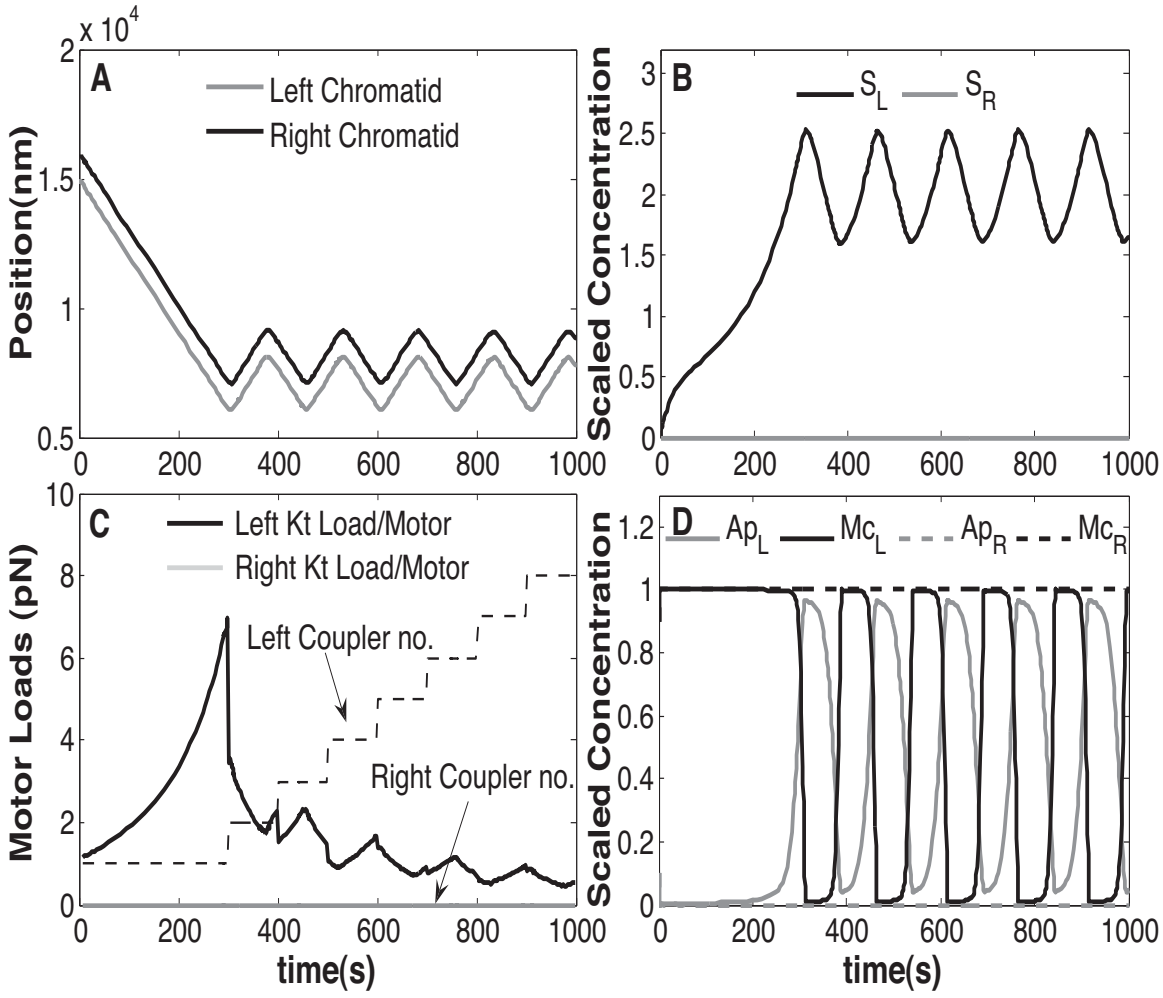

Figure 3.5. Monooriented chromosome directional instability. (A) Chromatid positions are controlled by respective feedback loops. The left pole is located at $x = 0$. The initial conditions for sister chromatids are: $x_L = 15$ μm; $x_R = 16$ μm; S_L=S_R=0; Ap_L=Ap_R=0.1; Mc_L=Mc_R=0.9. (B and D) Chemical species levels during chromosome oscillations. (C) Motor numbers and loads per motor at each Kt.

the flat region of the load-velocity curves. This implies that all motors respond with the same velocities despite individual load variations. Furthermore, since new attachments do not affect total load (and thus the local chemical reactions), the model predicts regular monooriented oscillations that are insensitive to the number of attachments at a kinetochore.

As can be seen from the sensor species concentrations plotted in Figure 3.5B, "directional instability" for monooriented chromosomes is a direct byproduct of sensor species oscillations. Sensor species oscillations occur due to the change in the balance of forces

as the chromosome changes position. The oscillations in sensor levels turn on or off the bicyclic cascade switch, as shown in Figure 3.5D. If a kinetochore moves to a location where the load it feels increases, then the sensor reaches its threshold value S_θ faster. Once above threshold, S levels force A to fully activate by mediating its phosphorylation into Ap which subsequently turns off the depolymerase Mc. The time necessary for Ap to build up and Mc to shut down is the time allocated for direction switch in our model. Consequently, the kinetic parameters for kinases and phosphatases are chosen to match the sharp chromosome directional changes ($\approx$ 6s [29]). When Mc is inactive the Kt diffusive couplers are in polymerizing state driving antipoleward motion, which causes the couplers to feel less load, S decays below S_θ and the phosphorylation cascade switch is reversed so that monooriented directional instability is established.

It should be noted that the reaction cascade we propose here exhibits threshold dependent switching behavior. Oscillations are not sustained if Ap and Mc activation curves lack the necessary zero order ultrasensitivity, which is controlled by K_m values as predicted in [8]. In the Appendix, we plot chromatid positions for different values of phosphorylation reaction kinetic parameters. The model predicts monooriented chromosome oscillations for a wide range of parameter values provided there are sufficiently sharp thresholds in the activation of the kinase and kinesin species. It should be noted that it is likely that more steps are involved in the cascade than our minimal representation. Increasing the number of cascade steps could produce sharper thresholds in activation since sensitivity is amplified in subsequent cycles [8] resulting in a possible increase of oscillation robustness.

For the system with linear load-velocity curves we obtain similar monooriented oscillations. In the Appendix, we plot system solutions for the position and kinetochore chemical levels of a monoriented chromosome with linear load-velocity curves. The system produces monooriented oscillations independent of the initial chromosome position, with some slight differences in movement arising from the shape of the load-velocity curves. As expected, velocities are not constant, this is especially noticeable in the initial left pole approach while motor loads increase. The variation of velocity becomes apparent when the sensor production rate is slightly decreased, as shown in the Appendix supplementary figures. Also, in contrast to the diffusive coupler motors, for the system with linear load-velocity curves the addition of new connections affects the shape of monooriented oscillations since motor load variation imposes changes in velocity. Clearly, the diffusive coupler model is a much more adequate model for the coupling mechanism, although the linear load-velocity

approximation retains qualitative model behavior for the monooriented case.

In conclusion, our model suggests that monooriented oscillations could be the result of a local kinetochore load sensor driving fast switch-like phosphorylation cascades.

3.3.2 Congression of bioriented chromosomes

In Figure 3.6 we show the model solutions for which the right kinetochore is allowed to accumulate attachments so that the chromosome becomes bioriented.

In Figure 3.6A is shown the simulated motion of a chromosome which is initially monoori-

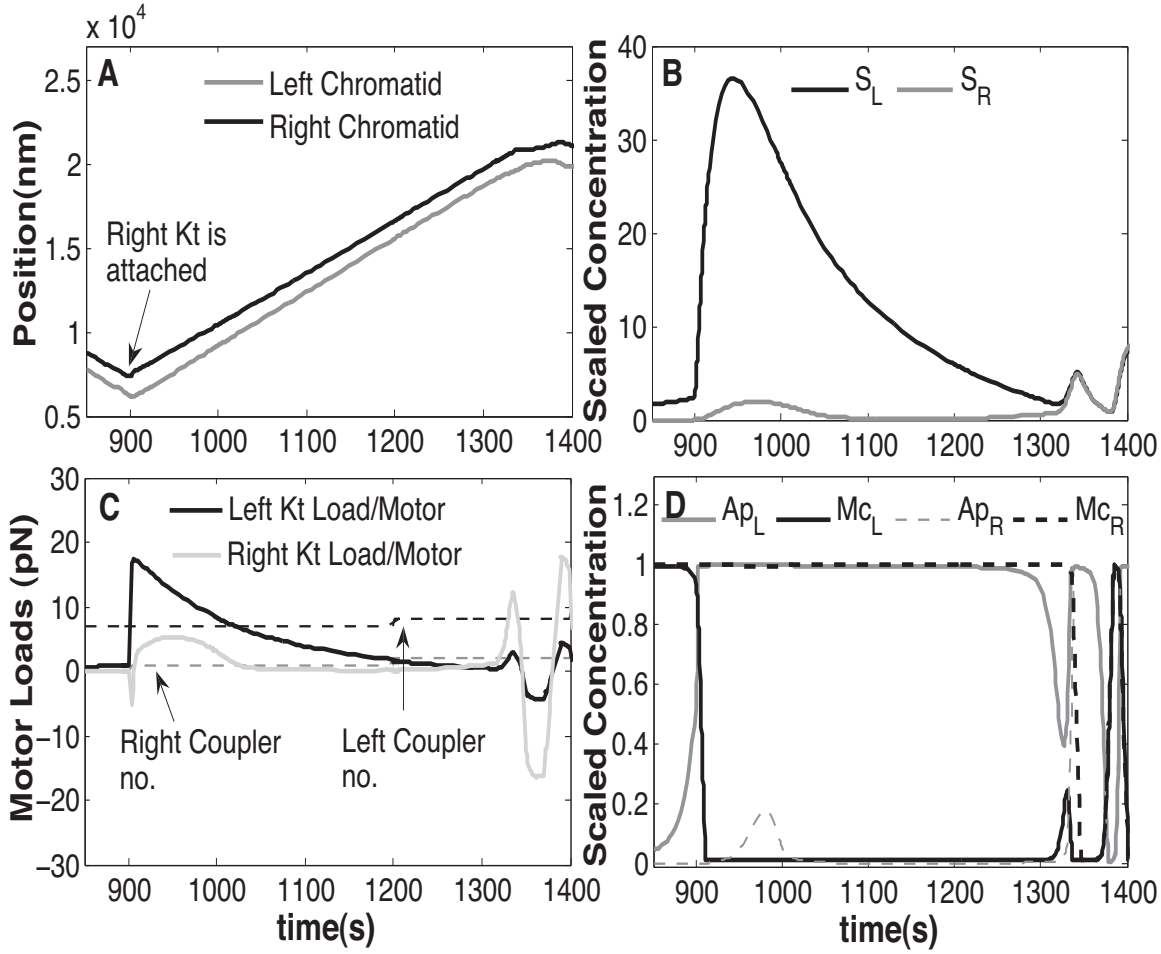

Figure 3.6. Bioriented congression. (A) The position of a chromosome which becomes bioriented at $t = 900$ s. For the polar ejection forces, f_{ap} is increased to allow for congression rates seen in [29]. Despite unequal attachment numbers, a leading Kt is established and congression is achieved. (B and D) Chemical species levels during chromosome oscillations. (C) Motor numbers and loads per motor at each Kt.

ented (7 left couplers attached) and becomes bioriented at $t = 900$ s when one right kinetochore coupler is engaged. Observe that the chromosome immediately changes direction and follows the right (leading) kinetochore with persistent motion away from the pole covering distances of ≈ 10 μm in a few minutes, in accordance with experimental observations in [29].

A comparison between sister kinetochore positions and chemical levels (Figure 3.6B, 3.6D) shows that the movement of sister chromatids follows the evolution of their respective chemical reactions. At the onset of biorientation, coupler motors at each sister kinetochore feel forces in opposing directions. The right kinetochore motor experiences a strong ejection gradient which pushes the kMT tips inside the coupler so that the right coupler responds with right pole directed (poleward) motion. The left couplers, on the other hand, feel large opposing AP loads which result in antipoleward velocities slightly smaller in magnitude than right coupler velocities. This difference produces immediate stretch on the center spring which increases the spring forces on both motors. However, only the left motors feel a significant pulling load and sensor increase since the AP gradient absorbs the spring force effects on the right coupler, as seen in Figure 3.6C. After the initial spring force spike, if the AP force gradient remains strong then right kinetochore motors continue to respond with poleward velocities, whereas the left kinetochore motors keep high sensor levels due to high loads. Consequently, both motors move with almost the same magnitude velocities toward the equator according to load velocity relationships. It is important to highlight here that congression in our model is insensitive to the amounts of trailing kinetochore sensor at the time of biorientation (figures not shown).

In fact, the distance travelled by a congressing bioriented chromosome depends on the strength of the ejection forces. In the Appendix, we show model solutions for high and low levels of polar ejection force gradients. We observe that for very weak AP forces a bioriented chromosome experiences oscillations close to the poles, essentially failing to congress. This is because the trailing kinetochore does not feel enough load to keep S from going below threshold and it attempts poleward trips at the onset of congression. However, once ejection forces build up, AP movement persists allowing for fast equator approach, as seen in experiments. This implies that the AP gradient strength directs congression by controlling the length of antipoleward trips and not velocity differences, in good agreement with observations in [29].

A comparison of attached motor numbers on each sister chromatid from Figure 3.6C

shows that congression is achieved despite the trailing kinetochore having far more motors attached than the leading one. Our simulations show that for the same values of the AP gradient, increasing the number of trailing kinetochore attachments does not significantly affect congression. More attachments on the trailing kinetochore produce more initial resistance to congression followed by sharp spring responses. However, if the AP forces can quickly counteract spring forces and keep sensor levels sufficiently high the trailing kinetochore moves antipoleward and congression progresses independent of the number of attachments. Therefore, the model suggests that the AP gradient is necessary and sufficient to assign a leading kinetochore independent of attachment numbers.

Interestingly, chemical species reactions show that sister kinetochores have very different levels of phosphorylated Mc during congression as seen in Figure 3.6D. Our simulations show a situation where the leading kinetochore always has all Mc active (unphosphorylated) whereas the trailing one has little active Mc (all phosphorylated) as it approaches the equator. This model behavior is particularly interesting since experiments have shown that Aurora B inexplicably phosphorylates MCAK asymmetrically across centromeres showing an accumulation of active MCAK at the leading kinetochore during congression [1][14]. It has been proposed that congression could be mediated by asymmetries in active MCAK levels [1][9]. Nonetheless, there is to date no clear mechanistic explanation as to why such differences in MCAK activity levels across kinetochores may occur. Our model predicts that asymmetries could be the result of inequalities in the dynamics of kinetochore chemical reactions caused by AP induced load differences across sister kinetochores.

Substitution of the load-velocity curves with linear functions does not change system behavior significantly during congression. In the Appendix, we show the simulated chromatid motion and respective chemical species levels of a chromosome that becomes bioriented at $\tau = 60$. Even though a chromosome congresses to the equator, linear load-velocity curves can cause early onset of right kinetochore congression opposing trips. This arises due to the fact that in the linear load-velocity curve case, direction reversal is achieved for different loads as compared to the nonlinear case (i.e., different x-intercept for each curve in Figure 3.3C). Thus, when AP forces weaken closer to the equator, smaller amounts of resistive spring forces cause the right motors to reverse into polymerizing motion than in the nonlinear case. In summary, the shape of the load-velocity curves affects the speed of congression through its triggering of resistive poleward trips during equatorial approach.

3.3.3 Bioriented chromosome oscillations

In Figure 3.7A, 3.7C and Figure 3.8A, 3.8C are shown model solutions for times after the initial congression has occurred.

Once a bioriented chromosome moves close to the equator the AP force gradient weakens and center spring forces become significant. Because of the load feedback response, as a chromosome gets closer to the equator, the motors prolong the congression-opposing states during which they test the AP gradient. Bioriented oscillations take place only if the

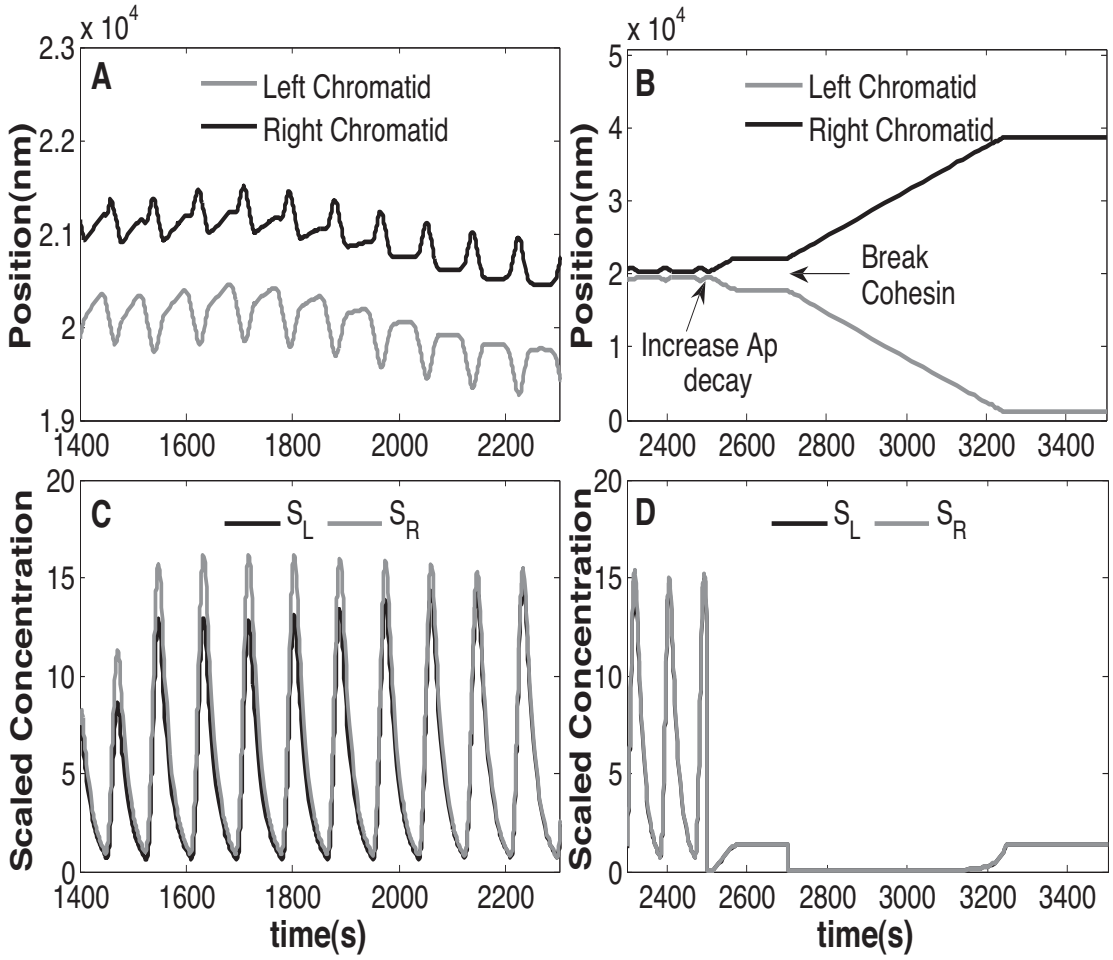

Figure 3.7. Bioriented chromosome oscillations and anaphase transition. (A and B) After congression chromosome oscillations are sustained at the equator when the sensor is properly localized. (C and D) Sensor species levels during oscillations and after sensor and spring removal. In panel B, D reaction parameters change as follows: 1) $t = 2500$ s sensor decay rate increases from $\mu = .05$ s^{-1} to $\mu = 5$ s^{-1} and oscillations cease with the chromosome stretched and precisely centered. 2) $t = 2700$ s the cohesin spring is removed with $k_f = 0$ allowing for chromosome segregation.

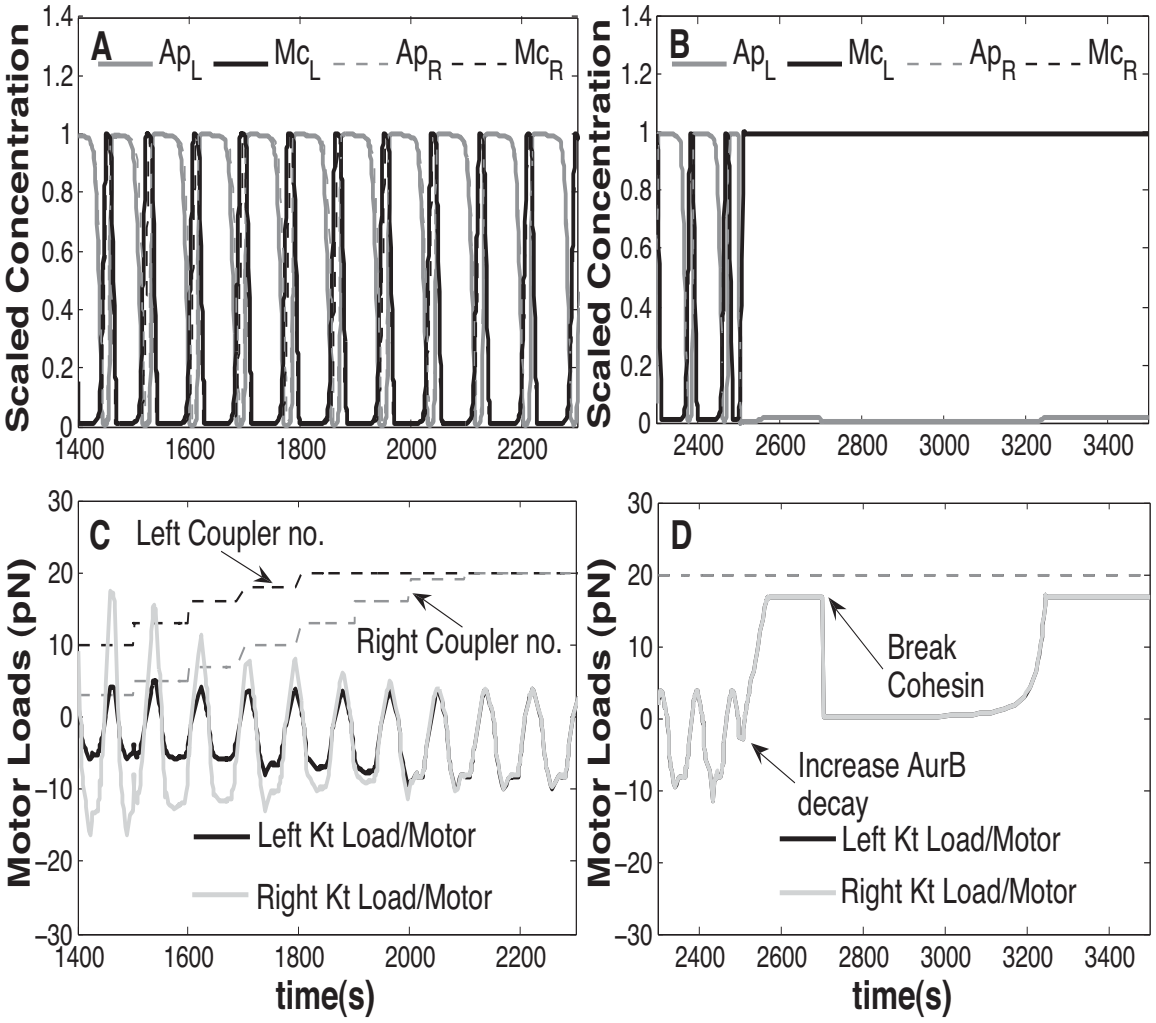

Figure 3.8. Bioriented chromosome oscillations and anaphase transition. (A and B) Chemical species levels during chromosome oscillations at the equator. (C and D) Loads per motor and attached motor numbers for each Kt. In panel B, D reaction parameters change as follows: 1) $t = 2500$ s sensor decay rate increases from $\mu = .05$ s^{-1} to $\mu = 5$ s^{-1} and oscillations cease with the chromosome stretched and precisely centered. 2) $t = 2700$ s the cohesin spring is removed with $k_f = 0$ allowing for chromosome segregation.

AP gradient is weak enough for the motors to directly oppose each other so that both kinetochore sensors increase above threshold (intra-Kt tension takes over spatial cues). Sensors fully synchronize at the equator where there is no AP gradient bias, as seen in Figure 3.7C. Bioriented oscillations tend to be in-phase when there is a significant difference in the numbers of couplers engaged at each kinetochore, shown in Figure 3.7A. These in-phase movements are due to the difference in loads as seen in Figure 3.8C and subsequently the coupler velocity response of each sister chromatid. If the number of attached motors at each kinetochore is the same they all pick equal speeds for equal loads. So, as the differences in velocities decrease, kinetochores are forced into out-of-phase trips driven by sensor synchronization at the equator followed by periods of no movement where both kinetochores are polymerizing slowly against the center spring (neutral). In our simulations, the maximal amplitude of oscillations for bioriented in-phase and out-of-phase oscillations is ≈ 1 μm and the period is $\approx 1 - 1.5$ min. The amplitudes of these oscillations are smaller than the ones reported in [29], this is due to our choice of kMT polymerization and depolymerization rates. With higher kMT tip rates the amplitudes increase to closer match experimental observations.

In Figure 3.9 system solutions are displayed for a bioriented chromosome at the equator with linear load-velocity curve motors. The feedback mechanism in this case produces nearly identical bioriented oscillations, shown in Figure 3.9A, as simulations in Figure 3.7A for the fully nonlinear coupler.

In conclusion, our model predicts oscillations around the cell equator for bioriented chromosomes. The phase relationship between sister kinetochores seems to depend on the number of attachments established on each kinetochore. Unequal numbers of attachments produce in-phase oscillations similar to the ones seen in experiments. For equal numbers of attachments phases of no motion are seen, similar to those seen in experiments during bioriented oscillations but not during monooriented oscillations in newt lung cells [29]. Unequal numbers of attachments on sister kinetochores produce oscillations centered slightly away from the equator. However, when a chromosome steers too far from the equator AP centering cues become stronger than intra-centromeric tension which decreases sensor synchrony and causes quick trip interruptions that bias position toward the equator. This implies that attachment number variation can slightly offset centering until the chemical reactions can build a response to the AP gradient that points the chromosome back to the equator. Nonetheless, once the attachment numbers become nearly equal on each side, the

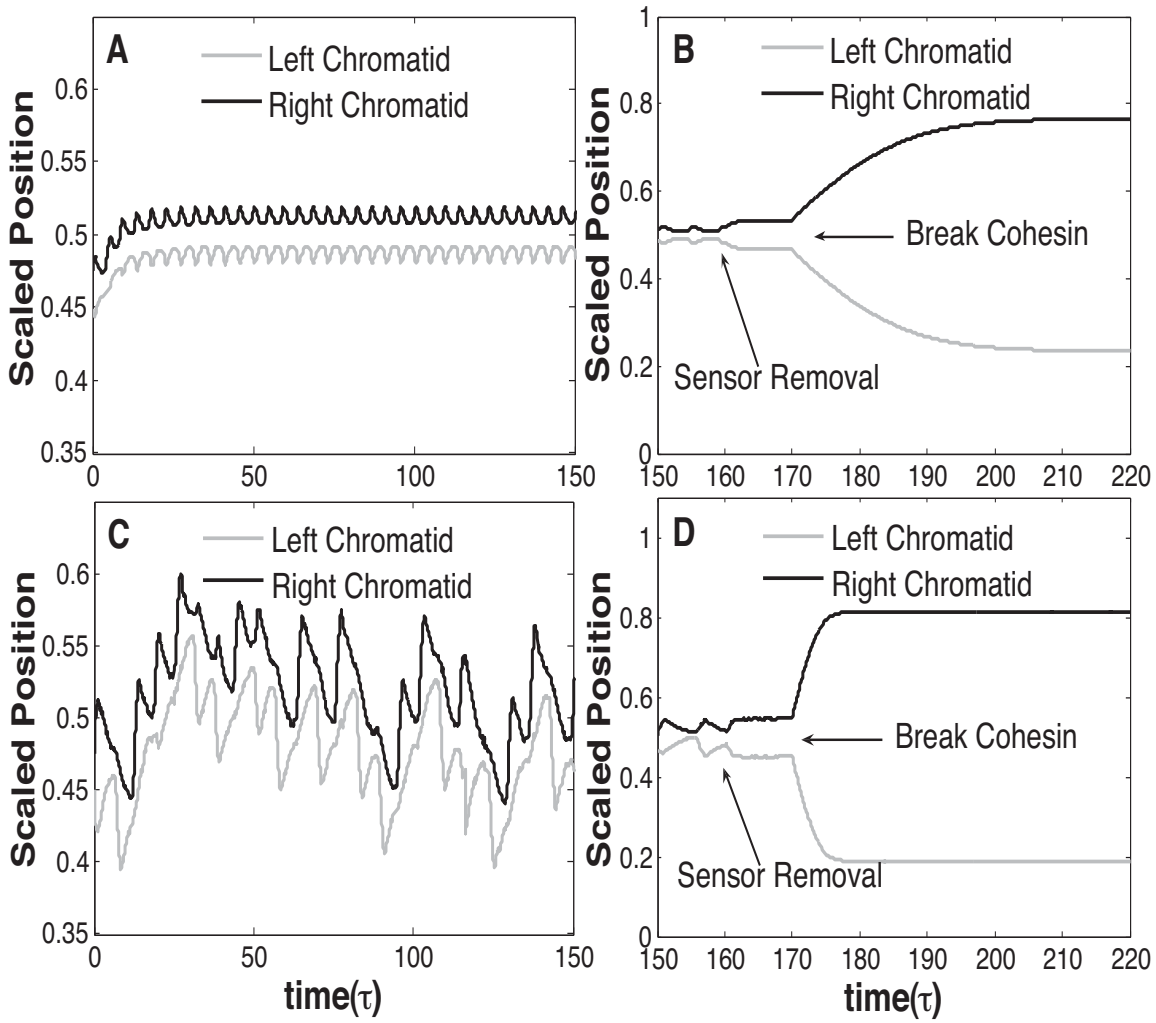

Figure 3.9. Bioriented chromosome oscillations and cellular noise effects for the system with linear load-velocity equations. (A and C) Bioriented chromosome oscillations are sustained at the equator when the sensor is properly localized. Each kinetochore has 20 attachments with initial conditions χ_L=.45; χ_R=.475; s_L=s_R=0; a_L=a_R=0.1; m_L=m_R=0.9. In panel C noise is introduced in the system and the depolymerization rate $\beta_{\max}$ is increased to allow for higher amplitude oscillations. (B and D) System response to feedback breakdown and spring removal. Reaction parameters change as follows: 1) $\tau = 160$, the nondimensional parameter k_1=$k_4 k F_{max}/\mu^2 = 14.4$ is reduced to $k_1 = 0.000144$ and oscillations cease with the chromosome stretched and precisely centered even when the system experiences random velocity variations. 2) $\tau = 170$ the cohesin spring is removed by setting the parameter $\gamma_4 = k_f/(\nu\mu) = 0$ allowing for chromosome segregation.

chromosome always returns to oscillating around the equator independent of the strength of the polar ejection gradient.

3.3.4 Metaphase/anaphase transition

So far we have discussed model results with the assumption that the chemical species included in the feedback remain localized at kinetochores. However, if the sensor species is interpreted as part of the chromosome passenger complex (CPC) then we should take into account that the position of this complex varies depending on the particular stage of cell division [27]. Since we integrate the action of this chemical species in movement control, we can use our model to test whether variation in species localization agrees with movement phenotypes observed in mitotic cells.

Once all chromosomes are properly aligned at the equator, AurB-INCENP relocates from centromeres to the spindle midzone microtubules due to Cyclin B degradation upon anaphase-start signal release [19]. We can investigate the effects of this relocation in our model by allowing for quick sensor removal, i.e., by increasing the decay rate μ. In Figure 3.7B, 3.7D anf Figure 3.8B, 3.8D we show model solutions extended after equatorial alignment as a function of time while model parameters are varied sequentially. In Figure 3.7B we show a plot of the position of each chromatid where at time $t = 2500$ s the sensor decay rate is significantly increased. Accordingly, oscillations stop and the chromosome is precisely positioned at the equator with high centromeric stretch. This behavior is explained by Figure 3.7D, 3.8B that show sensor levels below threshold and low kinase activity. The kinetochores thus pull against the polar ejection gradient until their couplers reach their stall loads. Thus, fast removal of sensor predicts a stretched conformation as a precursor to anaphase pole migration. However, as can be seen in Figure 3.10 where we have plotted solutions of the system with moderate μ rate, if removal is not very fast the system experiences oscillations with high centromeric stretching. In cells depleted of centromeric MCAK both stretch and oscillations were observed at the onset of anaphase [14]. We predict that both these experimental observations could be the result of different levels of feedback disassembly at kinetochores.

The final step for transition from metaphase to anaphase requires the protease separase to cleave a cohesin subunit allowing for sister chromatid separation [32]. There is evidence that transition into anaphase poleward movement might not only entail the breaking of the linking cohesins but also proper modulation of kinetochore chemical reactions. The reintroduction of Cyclin B in cohesin cleaved chromosomes can cause AurB-INCENP to

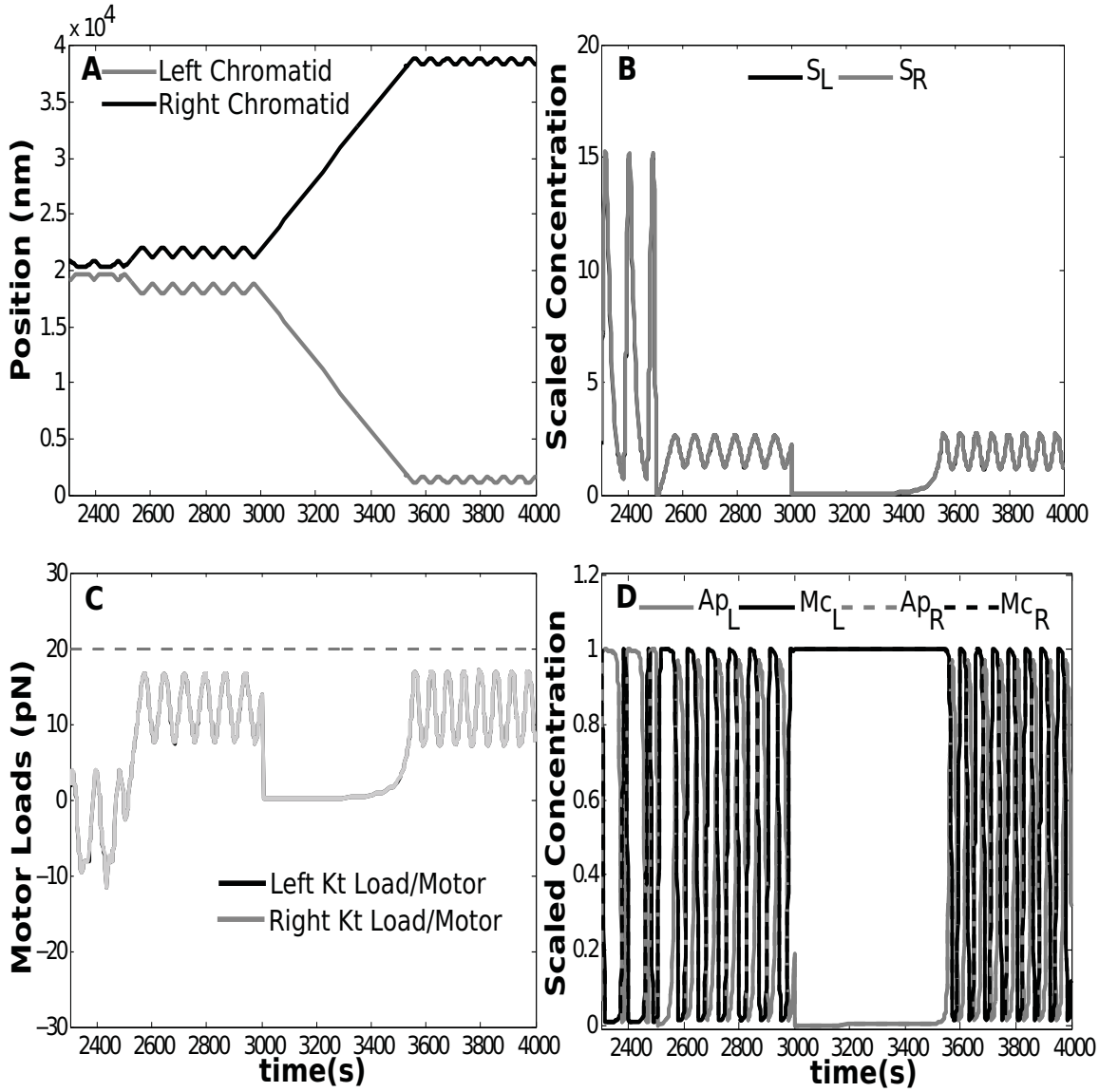

Figure 3.10. Bioriented chromosome oscillations at the equator for slow sensor relocation. (A) Chromosome position. (B and D) Chemical species levels at each kinetochore. (C) Load per motor and motor attachment numbers at each kinetochore. The reaction parameters change as follows: 1) at $t = 2500$ s sensor decay rate increases from $\mu = .05$ s^{-1} to $\mu = 2.5$ s^{-1} and oscillations persist with the chromsome stretched and precisely centered. 2) at $t = 3000$ s the cohesin spring is removed with $k_f = 0$ allowing for chromosome segregation.

not relocalize producing interesting chromosome movement phenotypes such as oscillations around a pseudometaphase plate [22]. Further, experiments that vary Cyclin B doses in cells show that a separated chromatid can either oscillate or experience stand-still behavior at different locations in the cell depending on polar-ejection strength [34]. Both experiments seem to indicate that kinetochore reactions (more specifically AurB removal) control anaphase movement phenotypes. We can easily test whether our model captures these experimental observations.

In Figure 3.7B we show the movement of a bioriented chromosome after cohesin removal ($k_f = 0$) at time $t = 2700$ s. Notice that poleward movement is sustained upon separation and reaction disassembly. However, if the sensor is not quickly removed oscillations occur due to the feedback response to load. In Figure 3.10 we have plotted the movement of a chromosome that undergoes separation when the removal of the sensor is slow; close to the poles oscillations persist. Our model produces both stand still and oscillatory movement at the equator for separated chromatids if the polar ejection forces are kept strong (figures not shown). If the feedback is partially operating after separation, oscillations persist close to the pole for weak polar ejection forces, or at a pseudometaphase plate if the force gradient is strong. If the removal of the sensor is complete then the chromatid loses oscillatory behavior and moves to a new equilibrium position where the motors stall, which can be either close to the pole or the equator depending upon the strength of the polar forces. Therefore, our results indicate that anaphase transition for chromosomes is not purely a force balance problem. Indeed, our model predicts that persistent anaphase poleward movement has a strong chemical component, which when interpreted as feedback disassembly, agrees well with experimental observations.

The relocation of the sensor produces the same stretching effects for the system with linear load-velocity equations as for the nonlinear load-velocity curves and finally the removal of the spring causes persistent poleward trips. In panel B of Figure 3.9, model parameters are changed so that at $\tau = 160$ there is faster sensor removal and at $\tau = 170$ the cohesin spring is removed. Just as in the nonlinear load-velocity curve motor case, if the sensor is not removed quickly enough the chromatids oscillate close to their respective poles after segregating (figure not shown).

In conclusion, the shape of the load-velocity curve does not significantly change the behavior of the negative feedback system. As long as the couplers can move with velocities that depend upon kMT tip rates, the negative biochemical feedback mechanism produces monooriented oscillations, congression, bioriented oscillations and proper segregation.

3.3.5 Feedback response to noise

Cells are noisy environments so a more realistic model of chromosome movement has to take into account some stochastic effects. Since the linearized system retained all the features of the implicit nonlinear model, we can easily explore the effects of noise on the system by perturbing the velocity equations (eq. (3.10)) with Gaussian distributed noise terms $\xi_i(t)$ (see Appendix). In Figure 3.9C, which shows the position of the chromatids of a bioriented chromosome, we see that the addition of noise causes the appearance of more in-phase oscillations at the equator. This is due to the the random variation of sensor values which can delay the phosphorylation switch response forcing kinetochores into in-phase movements. The noise induced in-phase oscillations are in very good agreement with observations in newt lung cells [29].

It is important to note that noise does not affect the precise centering of a chromosome at the equator after sensor relocation. This can be seen from the solutions plotted in Figure 3.9D where sequential parameter variation produces solutions which are very similar to those of the system without noise in Figure 3.9B. This implies that our biochemical feedback is robust to noise and an appropriate control mechanism in noisy cellular environments.

3.3.6 Feedback is robust to parameter variation

The response of the negative feedback mechanism depends on the value of a few key kinetic parameters. These parameter values however have not been experimentally measured so it is important to explore system robustness to parameter variations. Since the linearized system retains qualitative behavior of the full model we can use it to explore the robustness of the feedback and its dynamic properties.

In this section we investigate the behavior of our system under variations of the dimensionless parameters: $k_1 = k_A^+ k F_{\max}/\mu^2$, $K_1 = K_A/A_T = K_M/M_T$. These two parameters were chosen since they directly control monooriented and bioriented oscillations as follows: 1) the parameter k_1 encodes the strength of position cues into the feedback so its variation should affect system behavior, 2) the value of K_1 affects the delay in the feedback coming from kinase/kinesin switch and consequently controls the onset of oscillations.

In Figure 3.11 we have plotted the bifurcation diagrams of a monooriented chromosome (only one attachment at the left Kt) with respect to the parameters k_1 and K_1. Oscillations are sensitive to kinase/kinesin switch sharpness since a periodic branch appears for a small range of K_1, as seen in Figure 3.11B. However, once the value of K_1 is less than $K_{1\text{crit}}$ the system produces stable periodic solutions for a wide range of $k_1 > k_{1\text{crit}}$, Figure 3.11A.

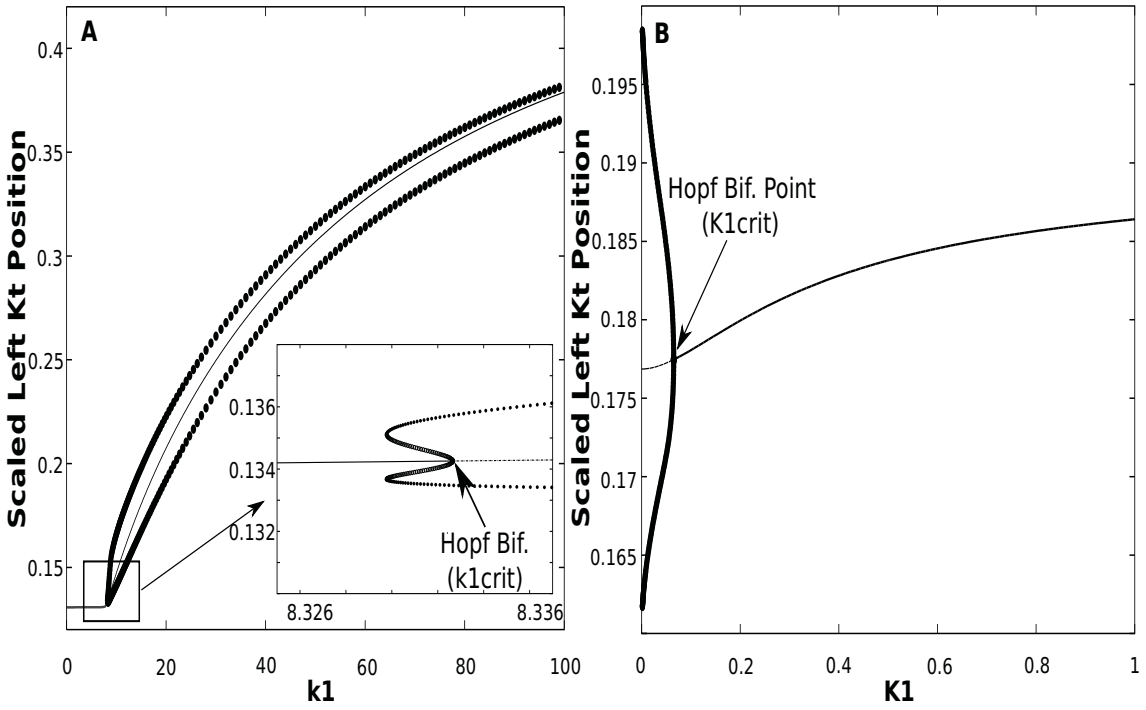

Figure 3.11. Bifurcation diagrams for a monooriented chromosome with linear load-velocity curves. Solid line depicts stable steady-states solutions whereas dashed line represents unstable steady-state solutions. Filled circles represent stable periodic solutions whereas open circles represent unstable periodic solutions. (A) Steady-state response of the left chromatid position, χ_L as a function of the parameter k_1. Inset. For a small interval of parameter k_1 values, close to the Hopf bifurcation point, the system experiences hysteresis. (B) Steady-state response of χ_L as a function of the parameter K_1.

Clearly, as k_1 increases the system becomes more sensitive to spatial cues and a monooriented chromosome will tend to oscillate closer to the equator. If the system is made extremely sensitive then any amount of AP gradient will cause even a monooriented chromosome to oscillate at the equator (the periodic branch asymptotes to χ=0.5 in Figure 3.11A). Thus, the model predicts that if too much sensor (AurB) is recruited at an attached kinetochore, a monooriented chromosome can be forced to the equator without the need for biorientation. Also observe in Figure 3.11 (inset) that around the Hopf bifurcation at $k_{1\text{crit}}$ the system experiences a brief hysterisis. This arises due to the nonlinearities in the feedback mechanism.

In Figure 3.12 we show the bifurcation diagram of a bioriented chromosome which has one motor attached at each kinetochore with respect to the variables k_1, K_1. Sister

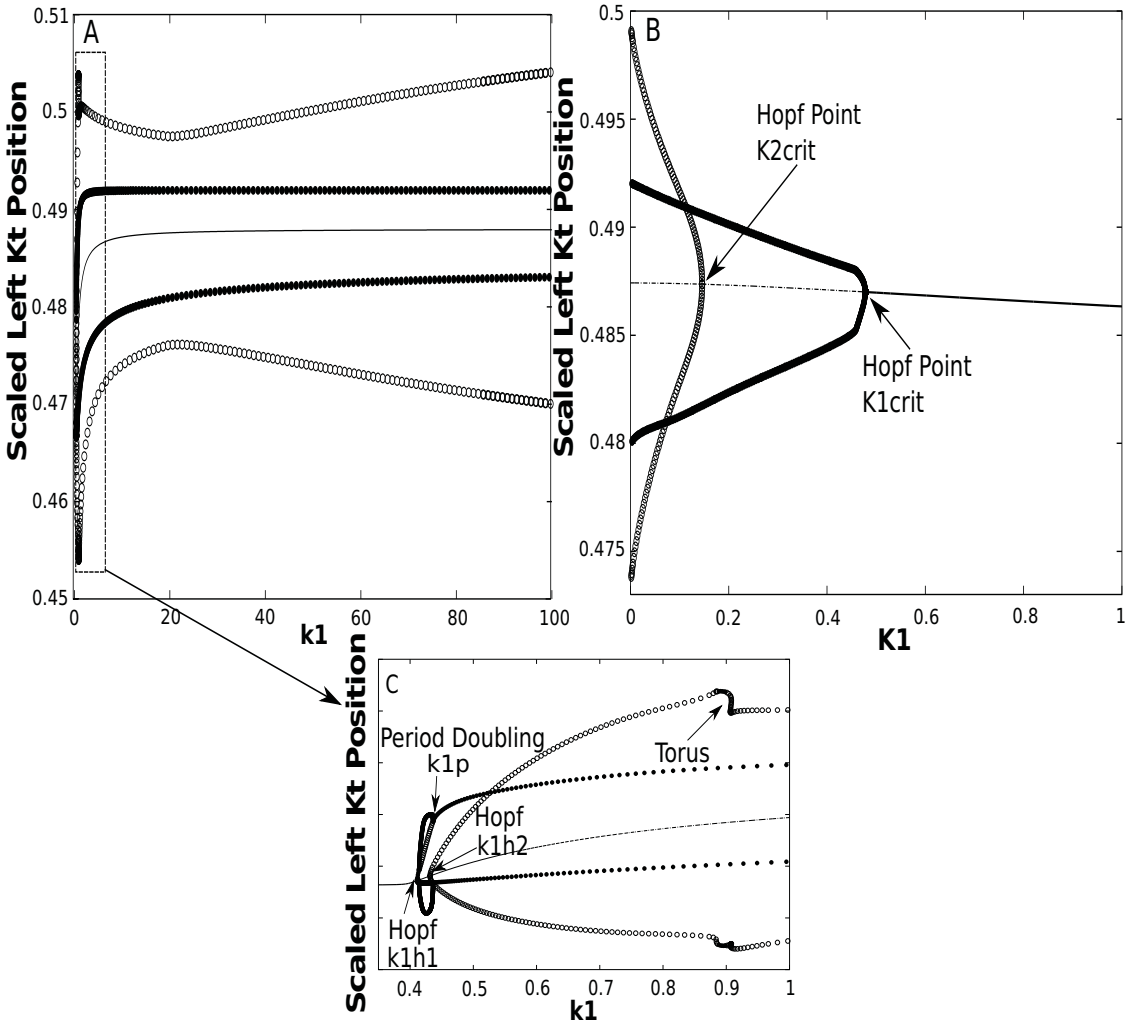

Figure 3.12. Bifurcation diagrams for the bioriented case with linear load-velocity curves. Solid line depicts stable steady-states, dashed line represents unstable steady-states. Filled circles represent stable periodic solutions whereas open circles represent unstable periodic solutions. To simplify the diagram we have shown the position of only the left chromatid, χ_L since the right kinetochore shows identical dynamics with positions shifted to the right due to spring separation. (A) Steady-state response of the left kinetochore position, χ_L as a function of the parameter k_1. (B) Steady-state response of χ_L as a function of the parameter K_1.

chromatid coupling with linear springs introduces more complex dynamics in the system. The variation of feedback sensitivity in Figure 3.12C generates two Hopf bifurcation points and a period doubling bifurcation for small values of k_1. The doubling of the period for $k_{1h1} < k_1 < k_{1p}$ indicates that if the system is fairly insensitive to spatial cues, it can take longer for a chromatid to complete an oscillation until it stops oscillating if k_1 is too small. The stable steady-state branch for $k_1 < k_{1\mathrm{h1}}$ shows that each kinetochore settles in a stretched position as the feedback is disassembled. The unstable periodic branch that appears for this system ($k_1 > k_{1h2}$, Figure 3.12A, 3.12C) shows interesting dynamic properties; however such behavior is due to the nonlinearity of the system and it is of no biological consequence due to lack of stability. Variation of K_1 in Figure 3.12B shows two periodic branches in the bioriented case; however, since the second branch is not stable, it does not affect chromosome oscillation dynamics at the equator. Note that the oscillatory domain with respect to the parameter K_1 has expanded compared to the monooriented system. We conclude by noting that bifurcation analysis indicates that monooriented and bioriented oscillations are robust to parameter variations once the kinase/kinesin switch is sufficiently sharp.

3.4 Discussion

During mitosis both mechanical forces and chemical signals are implicated in the accurate division of chromosomes. Mechanical forces directing congression arise from polar ejection forces that increase loads on sister chromatids when poles are approached. Several kinases localized at kinetochores are thought to read load information and change their activation states via phosphorylation reactions. Finally, substrates of kinetochore kinases can alter attached kMT tip dynamics, which in turn modulates Kt velocities.

In this chapter we propose a feedback control mechanism which integrates mechanical and chemical signals at kinetochores to recreate chromosomal movement. Even though there could be several Kt kinases that phosphorylate/dephosphorylate in a force dependent manner, we model motility by reducing all possible interactions into three simple reactions: a mechanical load reader species that activates/deactivates in response to loads, a kinase that experiences (auto)phosphorylation in response to sensor activation, and a kMT tip rate altering species that is regulated by the kinase. Chemical species levels are introduced into a diffusive coupler model, which yields a molecular scale treatment of kMT tip dynamics coupling to chromosomal velocities. The well-observed CPC-Aurora B-MCAK system could be the most direct representation of a possible complex network of load-sensing and kMT

tip rate modulation species. With parameters estimated from mitosis experiments, our simple network predicts many experimentally observed features of vertebrate chromosomal movement for both monooriented and bioriented states. The system shows robustness to parameter variation as well as cellular noise effects.

Previous theoretical models have successfully captured different aspects of chromosome motility in various organisms. The models of [12] for newt lung cells and [4] for *Drosophila* embryos are based on a force balance mechanism for chromosome motility. In our study, we sought to combine these mechanical force effects with local kinetochore reactions. Indeed, a force balance mechanism might be sufficient to generate oscillatory behavior; however, a kinetochore biochemical feedback mechanism might be necessary to assure robust monooriented oscillations, equatorial alignment and proper transition between different mitotic stages.

The limit cycle behavior produced by our model is different from the response produced by a biochemical feedback control mechanism recently proposed in [16]. We suspect that these differences are more likely to occur due to the introduction of load dependence on velocities rather than biochemical feedback topology differences. Consequently, we predict that the introduction of kinetochore motors in a biochemical feedback model can significantly affect chromosome motility.

If the biochemical feedback control we propose here indeed controls mitotic motion then the question about its functional significance naturally arises. Many proteins that localize at kinetochores are part of the spindle assembly checkpoint (SAC), a complex quality control network that blocks anaphase until all chromosomes are properly attached [21][27]. There is evidence that Aurora B either directly or through the CPC affects mitotic spindle checkpoint proteins which build a tension sensitive SAC signal [18][27]. In our model, at the onset of biorientation each kinetochore has different levels of the kinase A, but when the chromosome is fully centered, bioriented sister kinetochore sensors become fully synchronized. It could be that the presence of a feedback mechanism with kinases like AurB allows for a chemical signal build up to indicate that a specific chromosome is ready for separation. How such a signal can be transduced from chromosomes and how tension modulates it is not well known [21][27]. It would be interesting to investigate possible integration of chromosomal movement control with SAC dynamics.

3.5 References

[1] P. D. Andrews, Y. Ovechkina, N. Morrice, M. Wagenbach, K. Duncan, L. Wordeman, and J. R. Swedlow, *Aurora B regulates MCAK at the mitotic centromere*, Dev. Cell, 6 (2004), pp. 253–268.

[2] M. A. Bolton, W. Lan, S. E. Powers, M. L. McCleland, J. Kuang, and P. T. Stukenberg, *Aurora B kinase exists in a complex with survivin and INCENP and its kinase activity is stimulated by survivin binding and phosphorylation*, Mol. Biol. Cell, 12 (2002), pp. 3064–3077.

[3] I. M. Cheeseman and A. Desai, *Molecular architecture of the kinetochore-microtubule interface*, Nat. Rev. Mol. Cell Biol., 9 (2008), pp. 33–46.

[4] G. Civelekoglu-Scholey, D. J. Sharp, A. Mogilner, and J. M. Scholey, *Model of chromosome motility in Drosophila embryos: adaptation of a general mechanism for rapid mitosis*, Biophys. J., 90 (2008), pp. 3966–3982.

[5] S. C. Ems-McClung, K. M. Hertzer, X. Zhang, M. W. Miller, and C. Walczak, *The interplay of the N- and C-terminal domains of MCAK control microtubule depolymerization activity and spindle assembly*, Mol. Biol. Cell, 18 (2007), pp. 282–294.

[6] M. K. Gardner, C. G. Pearson, B. L. Sprague, T. R. Zarzar, K. Bloom, E. D. Salmon, and D. J. Odde, *Tension-dependent regulation of microtubule dynamics at kinetochores can explain metaphase congression in yeast*, Mol. Biol. Cell, 16 (2005), pp. 3764–3775.

[7] A. Goldbeter, *A minimal cascade model for the mitotic oscillator involving cyclin and Cdc2 kinase*, Proc. Natl. Acad. Sci. USA, 88 (1991), pp. 9107–9111.

[8] A. Goldbeter and D. Koshland, *An amplified sensitivity arising from covalent modification in biological systems*, Proc. Natl. Acad. Sci. USA, 78 (1981), pp. 6840–6844.

[9] G. J. Gorbsky, *Mitosis: MCAK under the aura of Aurora B*, Curr. Biol., 14 (2004), pp. 346–348.

[10] E. L. Grishchuk and J. R. McIntosh, *Microtubule depolymerization can drive poleward chromosome motion in fission yeast*, EMBO J., 25 (2006), pp. 4888–4896.

[11] T. L. Hill, *Theoretical problems related to the attachment of microtubules to kinetochores*, Proc. Natl. Acad. Sci. USA, 82 (1985), pp. 4404–4408.

[12] A. P. Joglekar and A. J. Hunt, *Simple mechanistic model for directional instability during mitotic chromosome movement*, Biophys. J., 83 (2002), pp. 42–58.

[13] T. M. Kapoor, M. A. Lampson, P. Hergert, L. Cameron, D. Cimini, E. D. Salmon, B. F. McEwen, and A. Khodjakov, *Chromosomes can congress to the metaphase plate before biorientation*, Science, 311 (2006), pp. 388–391.

[14] S. L. Kline-Smith, A. Khodjakov, P. Hergert, and C. Walczak, *Depletion of centromeric MCAK leads to chromosome congression and segregation defects due to improper kinetochore attachments*, Mol. Biol. Cell, 15 (2004), pp. 1146–1159.

[15] M. A. Lampson, K. Renduchitala, A. Khodjakov, and T. M. Kapoor, *Correcting improper chromosome-spindle attachments during cell division*, Nat. Cell Biol., 6 (2004), pp. 232–237.

[16] J. Liu, A. Desai, J. N. Onuchic, and T. Hwa, *An integrated mechanobiochemical feedback mechanism describes chromosome motility from prometaphase to anaphase in mitosis*, Proc. Natl. Acad. Sci. USA, 105 (2008), pp. 13752–13757.

[17] T. J. Mitchison and E. D. Salmon, *Poleward kinetochore fiber movement occurs during both metaphase and anaphase-a in newt lung cell mitosis*, J. Cell Biol., 119 (1992), pp. 569–582.

[18] C. J. Morrow, A. Tighe, V. L. Johnson, M. I. F. Scott, C. Ditchfield, and S. S. Taylor, *Bub1 and Aurora B cooperate to maintain BubR1-mediated inhibition of APC/C-Cdc20*, J. Cell Sci., 118 (2005), pp. 3639–3652.

[19] M. Murata-Hori and a.-L. W. M. Tatsuka, *Probing the dynamics and functions of Aurora B kinase in living cells during mitosis and cytokinesis*, Mol. Biol. Cell, 13 (2002), pp. 1099–1108.

[20] M. Murata-Hori and Y. Wang, *The kinase activity of Aurora B is required for kinetochore-microtubule interactions during mitosis*, Curr. Biol., 12 (2002), pp. 894–899.

[21] A. Musacchio and E. D. Salmon, *The spindle-assembly checkpoint in space and time*, Nat. Rev. Mol. Cell Biol., 8 (2007), pp. 379–393.

[22] D. H. Parry, G. R. X. Hickson, and P. H. O'Farrell, *Cyclin B destruction triggers changes in kinetochore behavior essential for successful anaphase*, Curr. Biol., 13 (2003), pp. 647–653.

[23] C. S. Peskin, G. M. Odell, and G. F. Oster, *Cellular motions and thermal fluctuations: the brownian ratchet*, Biophys. J., 65 (1993), pp. 316–324.

[24] A. F. Powers, A. D. Franck, D. R. Gestaut, J. Cooper, B. Gracyzk, R. R. Wei, L. Wordeman, T. N. Davis, and C. L. Asbury, *The Ndc80 kinetochore complex forms load-bearing attachments to dynamic microtubule tips via biased diffusion*, Cell, 136 (2009), pp. 865–875.

[25] C. L. Rieder, E. A. Davison, L. C. W. Jensen, L. Cassimeris, and E. D. Salmon, *Oscillatory movements of monooriented chromosomes and their position relative to the spindle pole result from ejection properties of the aster and half spindle*, J. Cell Biol., 103 (1986), pp. 581–591.

[26] C. L. Rieder and E. D. Salmon, *Motile kinetochores and polar ejection forces dictate chromosome position on the vertebrate mitotic spindle*, J. Cell Biol., 124 (1994), pp. 223–233.

[27] S. Ruchaud, M. Carmena, and W. C. Earnshaw, *Chromosomal passengers: conducting cell division*, Nat. Rev. Mol. Cell Biol., 8 (2007), pp. 798–812.

[28] S. Sandall, F. Severin, I. X. McLeod, J. R. Y. III, K. Oegema, A. Hyman, and A. Desai, *A Bir1-Sli15 complex connects centromeres to microtubules and is required to sense kinetochore tension*, Cell, 127 (2006), pp. 1179–1191.

[29] R. V. Skibbens, V. P. Skeen, and E. D. Salmon, *Directional instability of kinetochore motility during chromosome congression and segregation in mitotic newt lung cells: a push pull mechanism*, J. Cell Biol., 122 (1993), pp. 859–875.

[30] K. Tanaka, E. Kitamura, Y. Kitamura, and T. U. Tanaka, *Molecular mechanisms of microtubule-dependent kinetochore transport toward spindle poles*, J. Cell Biol., 178 (2007), pp. 269–281.

[31] J. J. Tyson, K. C. Chen, and B. Novak, *Sniffers, buzzers, toggles and blinkers: dynamics of regulatory and signaling pathways in the cell*, Curr. Opin. Cell Biol., 15 (2003), pp. 221–231.

[32] F. Uhlmann, *Secured cutting: controlling separase at the metaphase to anaphase transition*, EMBO Rep., 2 (2001), pp. 487–492.

[33] J. C. Waters, R. V. Skibbens, and E. D. Salmon, *Oscillating mitotic newt lung cell kinetochores are, on average, under tension and rarely push*, J. Cell Sci., 109 (1996), pp. 2823–2831.

[34] F. Wolf, C. Wandke, N. Isenberg, and S. Geley, *Dose-dependent effects of stable Cyclin B1 on progression through mitosis in human cells*, EMBO J., 25 (2006), pp. 2802–2813.

[35] L. Wordeman, M. Wagenbach, and G. von Dassow, *MCAK facilitates chromosome movement by promoting kinetochore microtubule turnover*, J. Cell Biol., 179 (2007), pp. 869–879.

CHAPTER 4

CHROMOSOME SEGREGATION IN BACTERIA

Caulobacter crescendus uses the dynamic interactions between ParA and ParB proteins to segregate its circular chromosome. Deletion of the proteins that are involved in the control of ParA monomer dynamics in the cytoplasm, such as TipN, leads to loss of unidirectional chromosome movement. It is not clear from experiments what mechanisms generate and control chromosome movement in these bacterial cells. In this chapter, we develop two mathematical models of the movement of the circular chromosome of *C. crescendus* during division. In the first model, posed as a set of stochastic differential equations (SDE), we propose that a simple biased diffusion mechanism for ParB/ParA interactions can reproduce the observed patterns of ParB and ParA localization in the cell. The second mathematical model, posed as a set of nonlinear partial differential equations, is a continuous treatment of the problem where we use results from the SDE model to describe ParB/ParA interactions and we also track ParA monomer dynamics in the cytoplasm. For both models, we show that if ParB complexes bind weakly and nonspecifically to ParA filaments, then they can closely track and move with the edge of a shrinking ParA filament bundle. Results from both models indicate that unidirectional chromosome movement is obtained when ParB complexes have a passive role in depolymerizing ParA filaments. Finally, we show that tight control of ParA filament dynamics is essential for proper segregation, and we test two mechanisms of TipN action in cells. Our model results are in agreement with experimental observations.

4.1 Introduction

Cell division in bacteria has not received much attention due to their perceived simplicity. Imagined as random bags of DNA, it was not clear whether bacterial cells actively moved their DNA during division. Recent experimental observations, however, indicate that active mechanisms similar to the mitotic spindle are operating in these cells.

Caulobacter crescendus has a single densely packed circular chromosome that spans the entire length of the cell. While the chromosome is replicating, *C. crescendus* uses a dedicated apparatus to move and segregate chromosome copies into the daughter cells. The two key components necessary for segregation are the proteins ParA and ParB. Similar to actin, ParA monomers first bind ATP and then assemble into dimers that are recruited into growing ParA filaments [1][3]. *In vivo* observations in *C. crescendus* indicate that ParAs are assembled into narrow linear structures (or bundles) oriented along the long axis of the cell. ParBs interact with ParAs through their N-terminal ends and also stimulate ATP hydrolysis causing the ParA filaments to depolymerize. The ParA/ParB system has been shown to be important in chromosome segregation in a few bacterial systems. In *C. crescendus*, the chromosome region bound by ParB translocates to the opposite side of the cell following a strictly unidirectional path [3][5]. Further, the position of moving ParBs in the cell has been observed to correlate with the retracting ParA bundle edges, indicating that the ParA network is somehow pulling ParB [5]. The mechanics of this coupled ParB/ParA movement are not well understood.

Proteins that localize at the cell poles have been implicated in the control of chromosome movement of *C. crescendus* [5]. One such protein is TipN, which localizes at the new pole and has been shown to be essential for unidirectional ParB movement during segregation. In $\triangle$tipN cells, the movement of ParB frequently changes direction and pauses [3][5]. Simultaneously, when TipN is missing, ParA filaments appear close to the old pole, in contrast with the wild type ParA network patterns [5]. There is evidence that there are direct interactions between ParA monomers and TipN [3]. TipN/ParA interactions are also corroborated by the accumulations of ParA proteins at the new pole in wild type cells. It is not clear how proteins that localize at one end of the cell, such as TipN, can affect the movement of ParB proteins that are located several microns away [3][5].

The connections between the spatiotemporal localization of ParA in dividing cells and the mechanisms of ParB segregation are not well understood. The movement of the *C. crescendus* chromosome has not been previously modeled. However a somewhat similar mechanism has been examined in *E. coli*, where a Par network works to move plasmids. Experimental observations in [1] indicate that ParA dynamics and plasmid movements are tightly correlated as plasmids oscillate in dividing cells. The ParA filaments in this bacterium are positioned in between the plasmids, which experience frequent switching in direction as they are pushed to the two cell halves. Plasmid movement dynamics were

explored with computational modeling for the first time by [4]. In the computational model proposed, proper plasmid localization could only be obtained if ParB detachment rates were made to be ParA filament length-dependent. This assumption is puzzling and not well motivated. Here we aim to develop a mathematical model for the underlying Par/chromosome interactions in the *C. crescendus* bacterium, and then we compare our results to plasmid segregation in *E. coli*.

We explore two questions in this chapter: 1) What are the underlying mechanisms that facilitate ParB motility in *C. crescendus*?, 2) How is the direction of ParB movement controlled in a dividing cell? Two mathematical models are constructed to answer the above questions. First, we develop a stochastic differential equation model that studies the mechanics of ParA/ParB interactions, which we simulate numerically using Monte Carlo simulations. Next, we develop a continuous model where partial differential equations are use to follow ParA/ParB interactions along with ParA monomer dynamics in the cytoplasm.

4.2 Model assumptions

In this section, we present the assumptions for both models of ParB/ParA mediated movement examined in this chapter.

Model components are shown in Figure 4.1. ParA is assumed to assemble into a bundle of linear filaments, or polymers. A ParA bundle of filaments extends from the new pole ($x = L$) to the vicinity of the old pole ($x = 0$), as depicted in Figure 4.1. Due to the structure of ParA bundles, ParA monomer removal or addition is only allowed at ParA filament tips. Further, once ParB has made initial contact with the bundle, all ParA polymers are assumed to depolymerize independently of ParB with a natural depolymerization rate β_0 [4]. Similarly, new ParA dimers can be added to the bundle with rate α. For the purposes of our work, we assume that a ParB complex under consideration has made initial contact with the ParA polymers; i.e., we do not model ParA assembly before it reaches the ParB complex of the replicated chromosome.

ParB is envisioned as a complex composed of a dense array of binders that can associate with ParA. The ParB binders have binding affinity for the ParA filament lattices, with no additional preference for specific ParA binding sites. Based on experimental evidence, we envision a ParB complex to wrap around the ParA bundle in order to maximize contacts with ParA filaments [1]. ParB interacts with ParA filaments and stimulates ParA ATP-ase activity, which results in the detachment of ParA from filaments [1]. Thus, we assume that ParB can bind and then depolymerize a ParA filament with rate β. The energetics of the

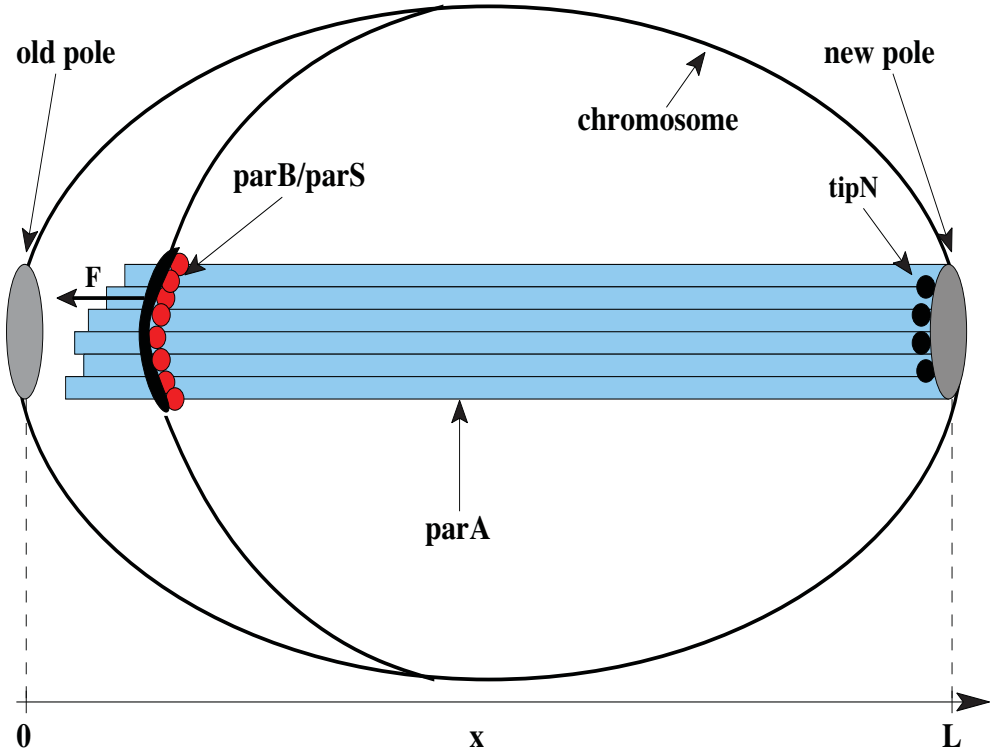

Figure 4.1. A diagram of the *C. crescendus* segregation apparatus. ParA assembles into linear filaments in the cell prior to making contact with a copy of the ParB complex of the replicating chromosome. ParB has binding affinity for the ParA filaments but also stimulates ATP hydrolysis of ParA dimers, which leads to depolymerization of ParA filaments. TipN proteins localize at the new pole and also interact with ParA monomers in the cytoplasm. In wild type cells, the ParB complex pulls the replicated copy of the chromosome from the old pole to the new pole without reversing direction.

ParA/ParB binding interactions are described by an explicit free energy function, Ψ. We specify Ψ for each model in the following sections.

ParB cannot move freely in the cell since it is attached to a chromosome copy through the parS site, as depicted in Figure 4.1. Since the size of the replicating chromosome is considerable, ParB movement is resisted by structures found in the cytoplasm. Accordingly, similar to kinetochores, the ParB complex is envisioned to be attached to a constant load F, which opposes movement. Also, in agreement with our kinetochore model, a ParB complex that is bound to the ParA bundle is supposed to undergo diffusion on the ParA filament lattices. Thermal effects must be taken into account here, since the ParB complex binds the ParA filaments nonspecifically.

The common parameters for the models are listed in Table 4.1. The effective drag

Table 4.1. Parameter Values

Parameter	Description	Value
L	Cell length	3 μm [5]
L_B	ParB length	.15 μm [5]
δ_m	ParA monomer/dimer length	10 nm
ν_B	ParB effective drag coeff.	.06 pNs/μm
ν_A	ParA effective drag coeff.	2×10^{-4} pNs/μm
D_B	ParB diffusion coeff.	0.069 μm^2/s
D_A	ParA diffusion coeff.	21 μm^2/s
F	ParB load	1 pN

coefficient for the ParB complex, ν_B, is calculated based on the Stokes drag coefficient formula $\nu_B = 6\pi\eta R_B$, with cytoplasmic viscosity $\eta = 2$ mPas and $R_B = 1.5$ μm, the radius of the sphere representing the ParB complex and the chromosome. Similarly, the drag coefficient for ParA dimers and monomers is $\nu_A = 6\pi\eta R_A$ with $R_A = 5$ nm. The diffusion coefficients are calculated from the Einstein relation, $D = k_B T/\nu$. The rest of the parameters are specified when we describe each model below.

4.3 Discrete model for ParB motors

In this section we develop a simple stochastic differential equation (SDE) model that addresses how a growing or retracting ParA bundle of filaments can move a ParB complex (or motor). In Figure 4.2 we show a diagram of the discrete model setup. The assumptions made to construct this model are as follows.

We represent a *C. crescendus* cell by a rectangular lattice with length L and width proportional to the number of ParA filaments present in the cell. The ParB complex is projected onto the ParA bundle in Figure 4.2, because we are assuming that ParB wraps around the bundle to maximize contact with ParA filaments. The SDE model equations

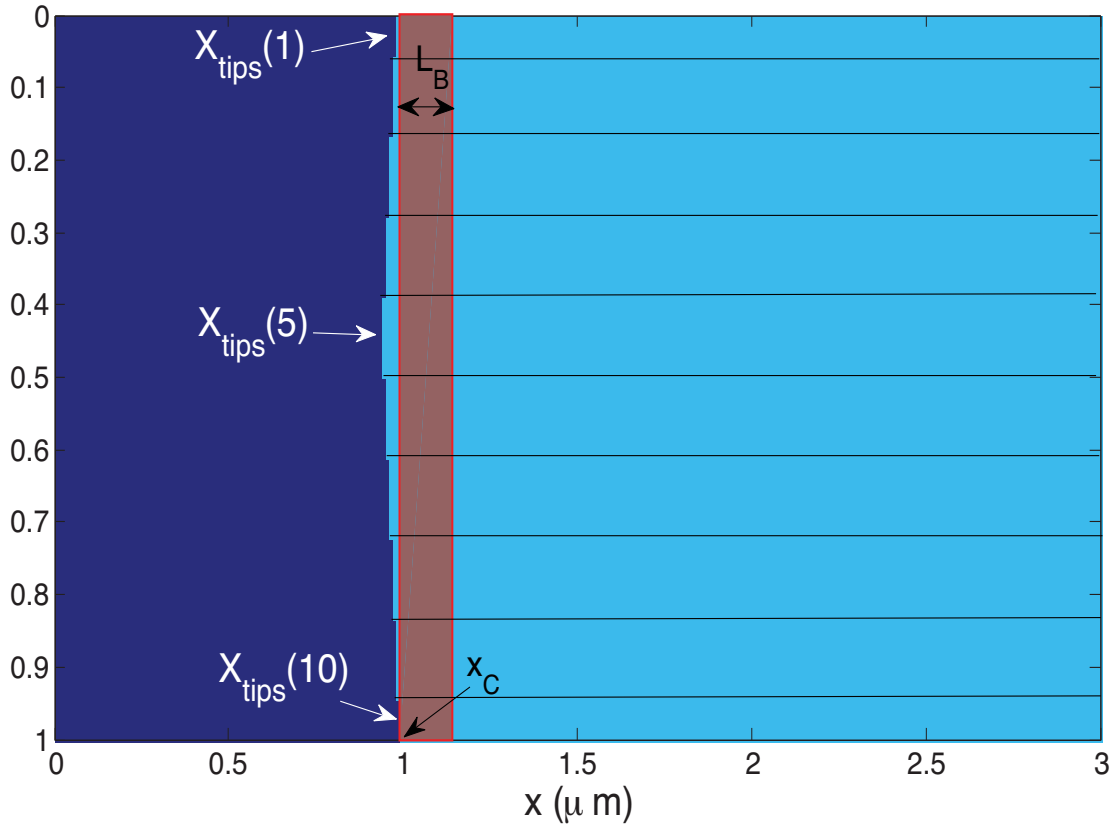

Figure 4.2. A diagram of the *C. crescendus* discrete model setup. The cell is envisioned as a rectangular lattice with length $L = 3$ μm. Multiple ParA filaments (light blue) are aligned next to one another. The ParB complex (red) binds the ParA filaments but also cleaves ParA monomers from the filament ends.

track the longitudinal or x-axis displacement of the ParB complex and ParA bundle tips.

ParB displacement on the x-axis is controlled by two forces in this model. A white noise forcing term due to thermal fluctuations of ParB, and a deterministic force that arises due binding between ParB binders and ParA filaments. Binding between ParB and ParA is energetically favored. Thus, a decrease in the system free energy is achieved when more ParB binders make contact with ParA filaments. Since ParB is supposed to be densely packed with binders, we ignore the position of specific ParB binders relative to the ParA bundle. Instead, the binding force on the complex can be calculated if we know how much overlap there is between ParB and ParA filaments. For the overlap between ParB and ParA, we must know the configuration of the ParA bundle at any given time. Thus, for each ParA polymer i in the bundle, we keep track of the position of individual filament tips, $x_{\text{tips}}(i)$ and we also track the position of the ParB complex denoted by x_c, see Figure 4.2. The total

overlap between ParB and ParA filaments, $A(x_c, x_{\text{tips}}(i))$ is calculated as

$$A(x_c, x_{\text{tips}}(i)) = \sum_i^n \max(\min(x_c + L_B - x_{\text{tips}}(i), L_B), 0), \tag{4.1}$$

where n is the total number of ParA polymers in the bundle. Note that by construction A has units of length.

The tip positions in Figure 4.2, which depicts the model configuration at $t = 0$, are arranged to replicate a ParA filament density that gradually increases as x increases. Hence, $x_{\text{tips}}(5)$ is positioned to be the tip closest to the old pole and $x_{\text{tips}}(10)$ is located the farthest distance from old pole. This arrangement generates a transition in tip densities from low at $x_{\text{tips}}(5)$ to high at $x_{\text{tips}}(10)$, creating what we refer to as ParA bundle edge. Note that as the distance between these extremal ParA tip positions increases, the ParA bundle edges lose their sharpness.

From our binding assumptions we deduce that if A increases, then the ParB system free energy decreases, since more ParB binders can make contact with the filaments. However, the size of the ParB complex is necessarily finite, and the ParB binders will eventually be all occupied. Given the definition of the overlap variable A in eq. (4.1), saturation of binders takes place when $A = A^* = nL_B$. Consequently, if $A \geq A^*$ the ParB system does not experience a decrease in free energy, i.e., there is no bias for ParB to increase the overlap with ParA. In accordance, the system free energy will produce a bias for more overlap in this model as long as $0 < A < nL_B$.

In view of our assumptions for binding, we construct a potential well function $\Psi(A)$,

$$\Psi(A) = \begin{cases} -aA & 0 < A < A^* \\ -aA^* & A \geq A^*. \end{cases} \tag{4.2}$$

The binding force $\Psi'(A)$ reads,

$$\Psi'(A) = \begin{cases} -a \sum_i^n \chi_{[x_c, x_c + L_B]}(x_{\text{tips}}(i)) & 0 < A < A^* \\ 0 & \text{otherwise.} \end{cases} \tag{4.3}$$

The parameter a is measured in pN and it represents the parB binding energy per unit length. The function $\chi_{[x_c, x_c+L_B]}$ is an indicator function defined as

$$\chi_{[x_c, x_c+L_B]} = \begin{cases} 1 & x_{\text{tips}}(i) \in [x_c, x_c + L_B] \\ 0 & \text{otherwise.} \end{cases} \tag{4.4}$$

Observe that the binding force term $\Psi'(A)$ is dependent on the density of filament tips present in the overlap at a given time. Thus, if the total density of tips in the overlap increases, then the ParB complex should feel more force in response.

The total binding energy felt by a fully attached ParB complex in this model is given by anL_b. The energetics of ParB/ParA binding interactions are currently not known, so we estimate the value of the parameter a. For our the discrete model simulations we use $a = 1$ pN. In *C. crescendus* cells a ParB complex is estimated to have around 500 binders [2] which gives us .7 k_BT of binding energy per binder. Due to the large number of ParB binders, the binding force values per binder are chosen to be smaller than the kinetochore binder energies used in the previous chapters, where each binder experienced a binding energy of 2.6 k_BT for association with the MT lattice.

With the above assumptions in hand, we are now ready to write the model equations. The Langevin equations for the ParB and ParA tip locations read

$$dx_c = \frac{1}{\nu_b}(-\Psi'(A) - F)dt + \sqrt{2D_B}dW_t, \tag{4.5}$$

$$dx_{\text{tips}}(i) = \delta_m dN_{\beta_0}(i,t) + \chi_{[x_c,x_c+L_B]}\delta_m dN_\beta(i,t) - \delta_m dN_\alpha(i,t), \tag{4.6}$$

where $N_\alpha(i,t)$, $N_\beta(i,t)$ and $N_{\beta_0}(i,t)$ are independent homogenous Poisson processes for each tip i, with amplitudes δ_m and ParA polymerization/depolymerization rates α, β, and β_0. We assume, for the rest of this chapter, that ParA dimer addition/removal rates have constant values; W_t is standard white noise, applied to the ParB complex.

Note that the model is composed of $n + 1$ equations in total. At the boundaries $x = 0$ and $x = L$, x_c is reflected and then fixed to $x_c = 0$ and $x_c - L_B$ to represent the capture of the ParB complex by PopZ at the cell poles. Further, we highlight that for this first model we have made some simplifying assumptions. Specifically, we have assumed that ParA monomers are abundant and well mixed in the cytoplasm so that the polymerization rate is not ParA monomer dependent. Further, the dimerization reaction of ParA in solution is assumed to be rapid compared to polymer growth, and we also ignore any TipN sequestration effects on ParA monomer concentration in the cytoplasm. The contributions from ParA monomer diffusion, ParA dimerization, and TipN sequestration are examined in the continuous model, which we discuss later in this chapter.

4.3.1 Discrete model results

The model equations given by eq. (4.5) - (4.6) are simulated numerically. In Figure 4.3 we show two typical solution trajectories for x_c and $x_{\text{tips}}(1)$, when the ParA filaments are

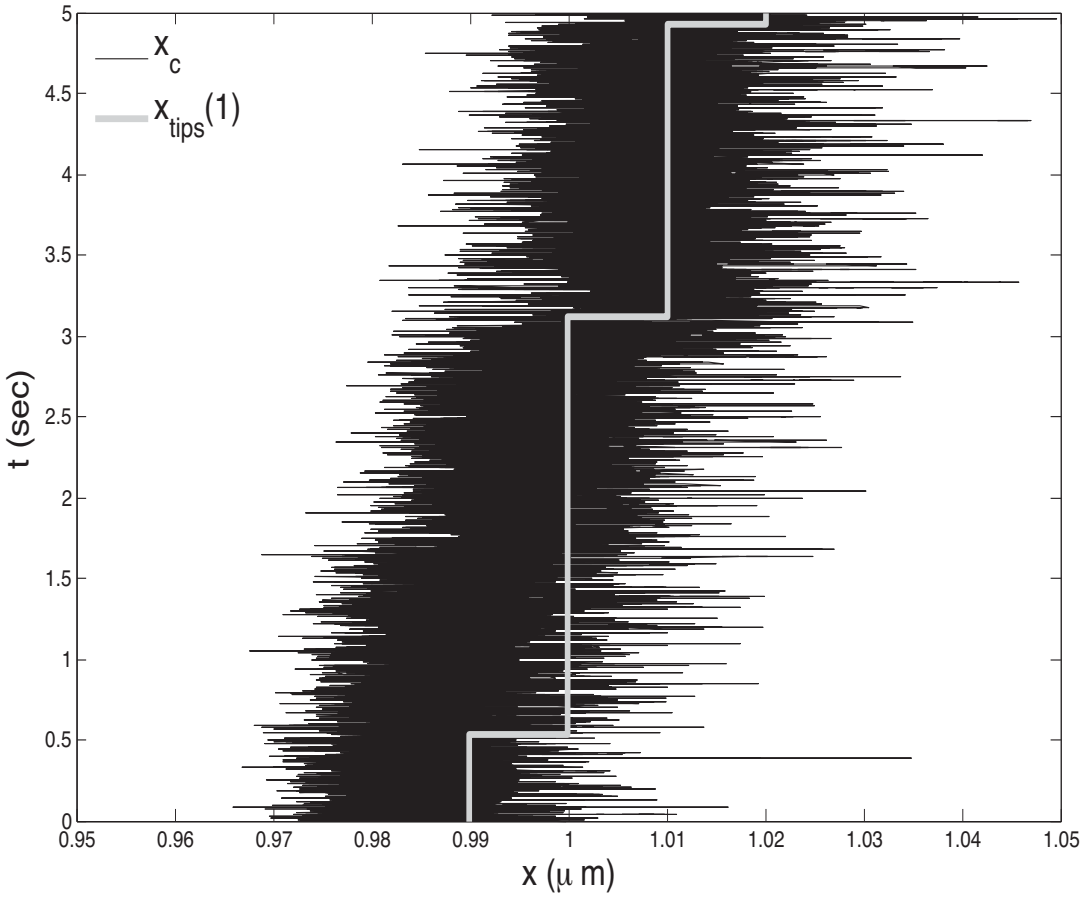

Figure 4.3. Solution trajectories for x_c and $x_{\text{tips}}(1)$. The ParB position, x_c experiences noise and drift toward the new pole because $A < A^*$ due to at least $x_{\text{tips}}(1)$ being found in the overlap. The tip $x_{\text{tips}}(1)$ experiences Poisson jumps of size δ_m. The simulation parameters are $\beta_0 = .5\ \text{s}^{-1}$, $\beta = .5\ \text{s}^{-1}$ and $\alpha = 0\ \text{s}^{-1}$.

depolymerizing ($\alpha = 0$).

As can be seen from the plot in Figure 4.3, the solution trajectory for x_c experiences both white noise and a binding force which guides the complex toward the new pole. For the trajectories shown in Figure 4.3, we observe that at least one ParA bundle filament ($\text{x}_{\text{tips}}(1)$) is located between x_c and $x_c + L_B$, which indicates that all the ParB binding sites are not saturated and $A < A^*$. Hence, the Ψ' forcing term biases the motion of x_c toward the new pole to increase the overlap. On the other hand, the tip position $x_{\text{tips}}(1)$ experiences jumps in position due to the Poisson noise terms in the tip Langevin equations. Since the polymerization rate is set to zero for this simulation, only depolymerization jumps occur and the tip moves closer to the new pole as monomers are cleaved.

Next, we simulate multiple solution trajectories ($N = 500$) for x_c and $x_{\text{tips}}(i)$ for different combinations of ParB depolymerization and ParA polymerization/depolymerization rates. In Figure 4.4 we show histograms for ParB positions, x_c with $\beta_0 = .5\ \text{s}^{-1}$, $\beta = .05\ \text{s}^{-1}$, and $\alpha = 0\ \text{s}^{-1}$. From the histograms in Figure 4.4, we observe that as time progresses the peaks of the ParB distributions shift toward the new pole, indicating that on average the binding drift term in eq. (4.5) is pushing the complex to increase overlap with ParA filaments. On the other hand, we also notice a decrease in the peaks and an increase in the tails of the

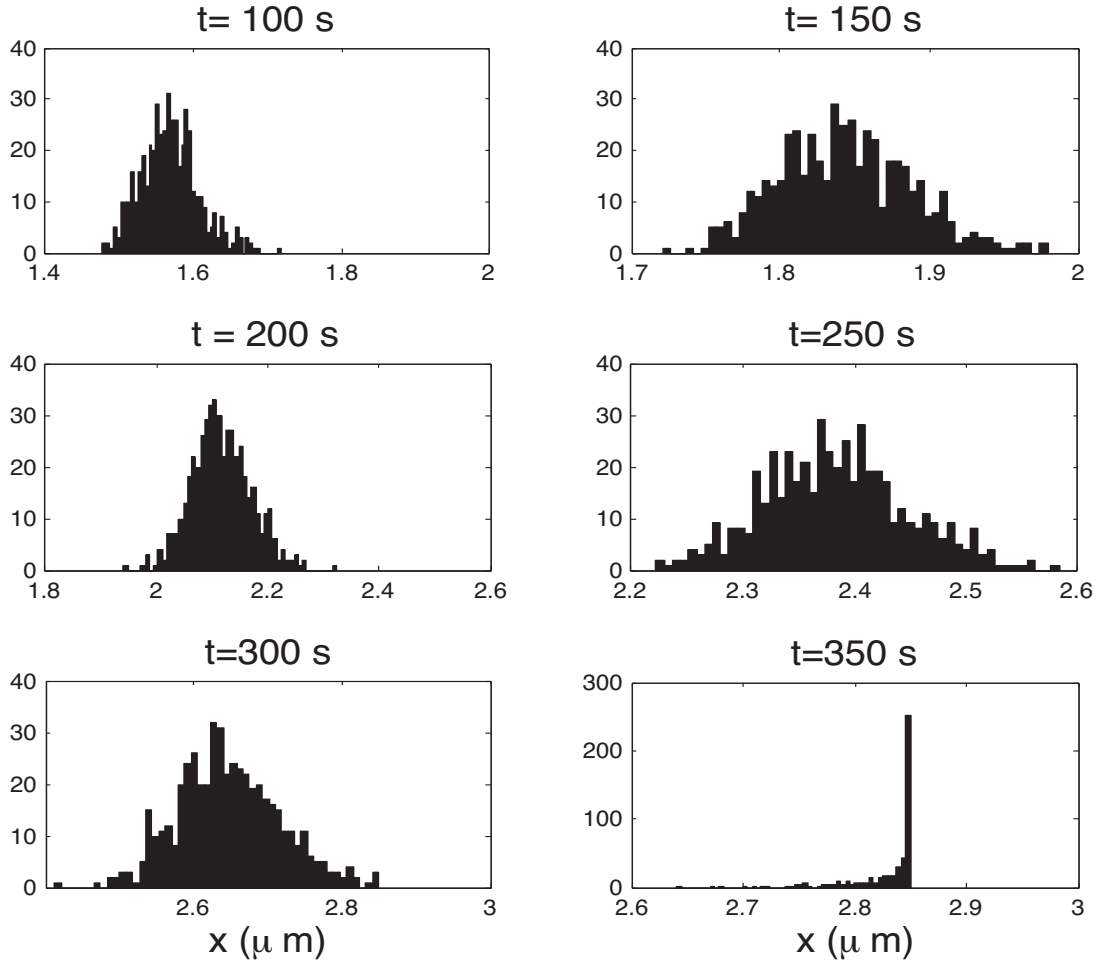

Figure 4.4. Histograms of ParB positions for a depolymerizing ParA bundle. Each histogram is generated from 500 solution paths of eqs. (4.5)-(4.6). When ParA bundles depolymerize with $\beta << \beta_0$, the histograms for ParB positions shift on the x-axis toward the new pole pushed by the binding force Ψ'. Over time, the histograms show smaller peaks and growing tails, indicating higher variability in ParB positions. The simulation parameters are $\beta_0 = .5\ \text{s}^{-1}$, $\beta = .05\ \text{s}^{-1}$, and $\alpha = 0\ \text{s}^{-1}$.

distributions, which indicates that over time there is higher variability in ParB positions in the cell. We can get a better idea about the behavior of our model if we plot the average positions for both ParB and two representative ParA tips.

In Figure 4.5, we show the average values for x_c and ParA tips, $x_{\text{tips}}(10), x_{\text{tips}}(5)$ obtained from simulations with $\beta_0 = .5\ \text{s}^{-1}$, $\beta = .05\ \text{s}^{-1}$, and $\alpha = 0\ \text{s}^{-1}$.

The plot of position averages in Figure 4.5 indicates that the ParA tips and the ParB complex closely track one another as they both approach the new pole. Because ParB advances toward the new pole during these simulations, we deduce that the overlap is staying on average under A^* and the binding drift in the x_c equation pushes firmly in the direction of the new pole. Eventually the ParB complex finds the new pole and the

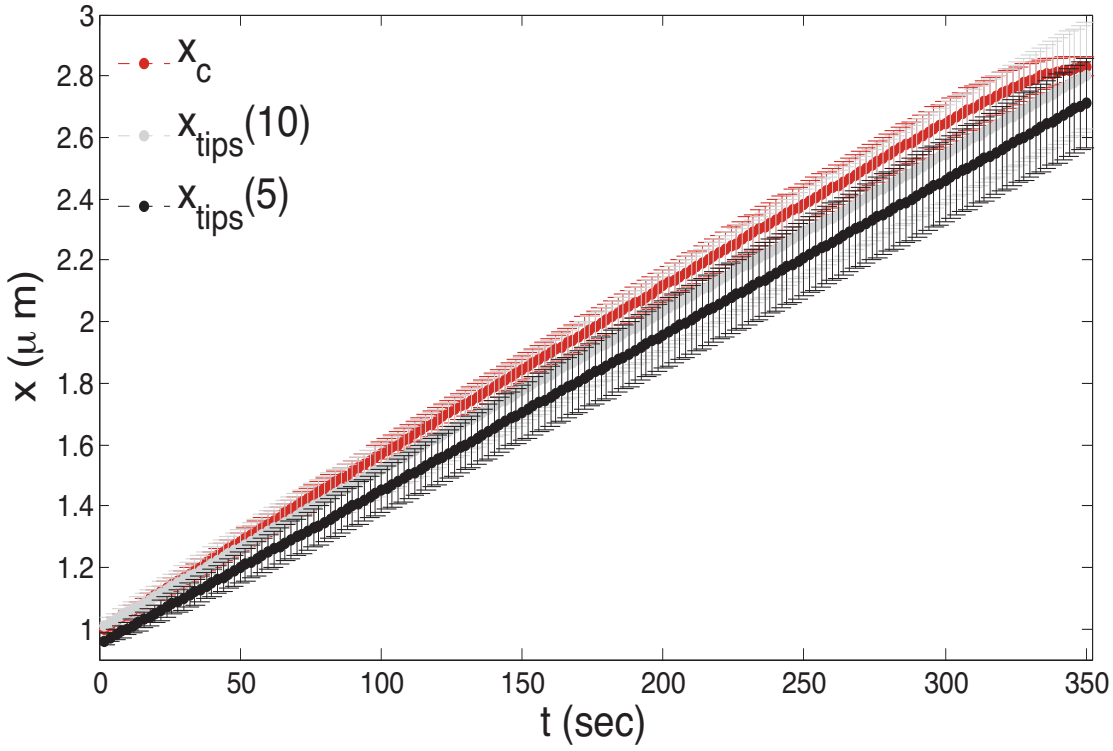

Figure 4.5. Average x_c, $x_{\text{tips}}(5)$, and $x_{\text{tips}}(10)$ versus time for $\beta << \beta_0$. Each point in the plot is obtained by averaging the data from 500 solution trajectories of eqs. (4.5)-(4.6). The bars mark standard deviation. When $\beta << \beta_0$, ParB distributions move toward the new pole along with $x_{\text{tips}}(5)$ and $x_{\text{tips}}(10)$. The distance between average extremal tip positions increases over time indicating that ParA bundle edges lose their sharpness. For all three solution trajectories plotted, the distributions have increasing tails as marked by the increasing standard deviations. The simulation parameters are $\beta_0 = .5\ \text{s}^{-1}$, $\beta = .05\ \text{s}^{-1}$, and $\alpha = 0\ \text{s}^{-1}$.

distributions tighten around $3 - L_B$, as can be seen from the histograms plotted in Figure 4.4.

In Figure 4.5 we see that the distance between the average positions for $x_{\text{tips}}(10)$ and $x_{\text{tips}}(5)$ increases over time, which indicates that ParA edges lose sharpness. This property can be understood if we refer back to our binding well function Ψ. As soon as ParB latches on to the ParA bundle, the binding energy well Ψ pushes x_c to maximize overlap to A^*, thus forcing the ParB complex to sit slightly ahead of the tips in order to fill as many binding sites as possible. This ParB position with respect to the ParA bundle unavoidably leaves some ParA tips out of the ParB overlap. The tip positions located the closest to ParB, such as $x_{tips}(10)$, consequently experience $\beta + \beta_0$ jump rates as opposed to β_0 for the tips that are left behind by ParB, such as $x_{tips}(5)$. The difference in depolymerization rates for the ParA tips creates a situation where there is a bias for tips moving away from one another over time (spreading out).

The change in tip arrangement on the ParA bundle feeds back into the movement of ParB in two ways. First, as the tips spread out, the region for which $A < A^*$ on the ParA bundle edge has increased, thus ParB can inch further forward toward the new pole. Second, the spreading of the tips on the ParA bundle lowers tip densities at a position x on the bundle so the number of tips and consequently Ψ' decreases. Therefore, diffusion slowly takes over other forces in eq. (4.5), increasing the variance of ParB positions sitting on the ParA bundle, shown by the increasing ParB standard deviations in Figure 4.5. Larger tails in the ParB distributions cause more variation in depolymerization rates on the ParA bundle filaments, which in turn results in increased variation in the positions of the ParA tips. In conclusion, in this model, over time ParB binder and ParA tip distributions become less focused, and the standard deviations increase for both x_c and $x_{\text{tips}}(i)$.

From the numerical model solutions thus far, we have learned that ParA filament configuration and ParB movement are tightly connected due to the dependence of the ParB binding term on the overlap A. Since we postulated that the spreading of the ParA bundle edge depends on the difference between β_0 and $\beta + \beta_0$, we expect that as β becomes larger while β_0 is fixed, some ParA tips will move faster ahead of the bundle toward the new pole due to the higher ParB depolymerization rate. Also, the ParB distributions will feel diffusion effects earlier in the simulations as Ψ' in the drift term declines in response to faster spreading of ParA filament tips. In order to test our hypothesis, we solve our model when β is increased as β_0 is kept fixed.

In Figure 4.6, we repeat our simulations when the depolymerization rate β is increased.

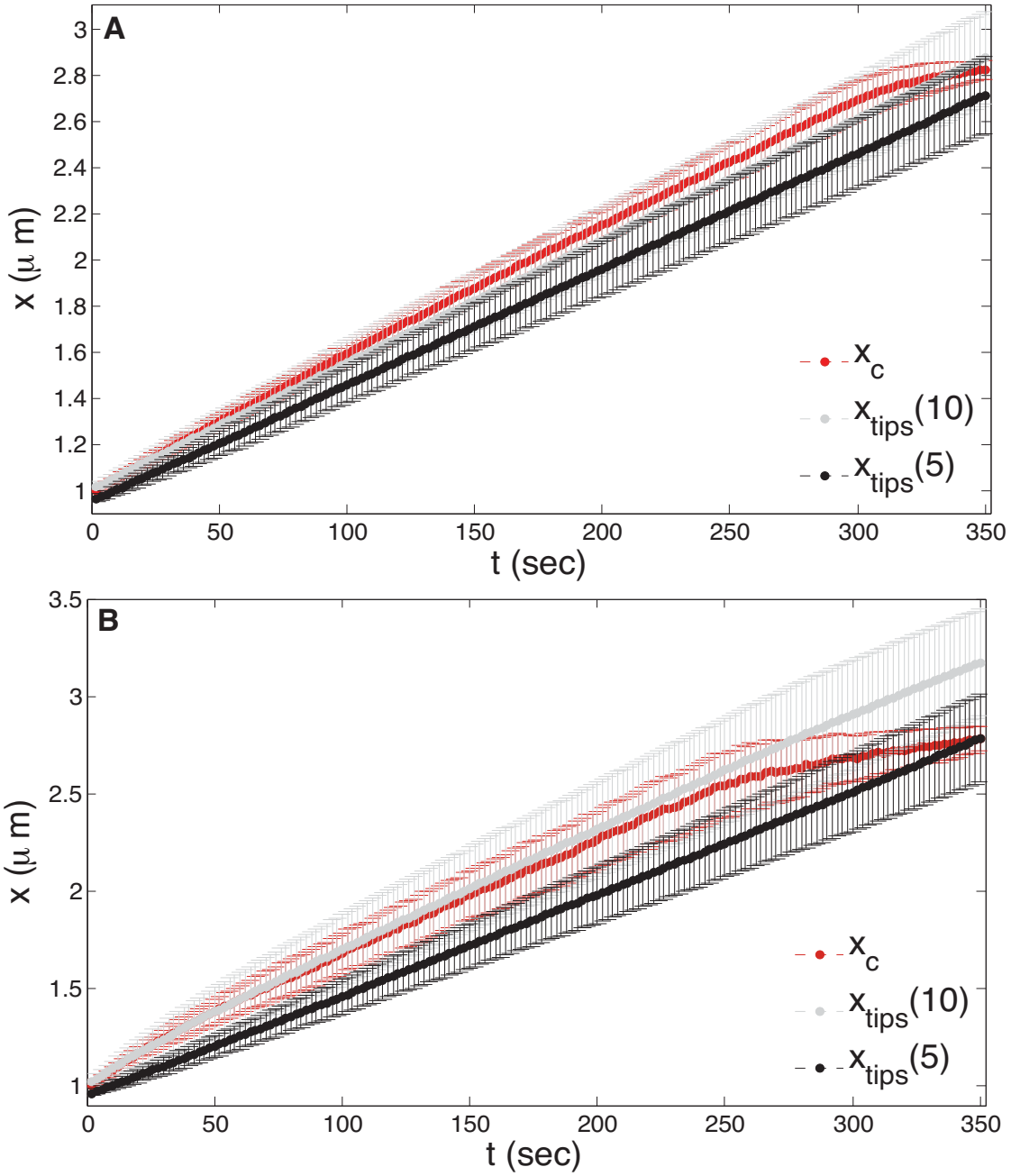

Figure 4.6. Average x_c, $x_{\text{tips}}(5)$, and $x_{\text{tips}}(10)$ versus time for a depolymerizing ParA bundle. Each point in the plot is obtained by averaging the data from 500 solution trajectories of eqs. (4.5)-(4.6). The bars mark standard deviation. The parameters are $\beta_0 = .5$ s^{-1}, and $\alpha = 0$ s^{-1}. A. For $\beta = .1 < \beta_0 = .5$, ParB distributions move toward the new pole along with $x_{\text{tips}}(5)$ and $x_{\text{tips}}(10)$ as the distance between average extremal tip positions increases over time. B. For $\beta = .5 = \beta_0 = .5$, the distance between average extremal tip positions increases very quickly and ParB experiences erratic motion.

From the average position plots for x_c and $x_{\text{tips}}(10)$, $x_{\text{tips}}(5)$ in Figure 4.6A and Figure 4.6B, we see that as we increase the ParB depolymerization rate, β, both the ParB positions and the ParA tip distributions have significantly larger tails. This is due to the higher ParB depolymerization rate which depolymerizes tips that are closest to the new pole faster leaving many trailing ParA tips behind. This is indicated by the fast increase in the distance between the average $x_{\text{tips}}(5)$ and $x_{\text{tips}}(10)$ followed by large standard deviations for $x_{\text{tips}}(10), x_{\text{tips}}(5)$ in Figure 4.6A and Figure 4.6B. On the other hand, as the ParA tips relocate, ParB distributions also quickly become more variable and experience erratic motion ahead of the ParA bundle edge, particularly when $\beta = \beta_0$. These results are telling us that when $\beta \approx \beta_0$, the ParB complex unavoidably leaves some ParA filaments behind as it erratically moves to the new pole. This mode of ParB movement is not in agreement with experimental observations which show that ParB positions strongly correlate with the position of the edge of a retracting ParA bundle.

Furthermore, it is clear from Figure 4.6B that ParBs reach the new pole on average faster when $\beta = \beta_0$. This slight change in velocities is due to the fact that for higher β ParBs spread more quickly ahead of the ParA bundle edge, which creates a faster average movement of the complex toward the new pole. We must remark however that from multiple simulations with various β_0, we saw that the velocities of ParB movement toward the new pole directly correspond to the magnitude of β_0. This is to be expected since x_c is driven by the presence of ParA at a position x.

Finally, we test the dependence of the ParB positions on ParA bundle dynamics by simulating the model when the ParA bundle is in a polymerizing state with $\alpha > \beta_0, \beta$. The case when ParA is growing is important to study because ParA filaments have been shown to have a natural tendency to polymerize if there are monomers available, as discussed in Chapter 1. A plot of the average positions for ParB and ParA tips when ParA is polymerizing is shown in Figure 4.7.

As can be seen from the plot in Figure 4.7A, when $\alpha > \beta + \beta_0$ the ParA filaments grow toward the old pole despite ParB binding and depolymerization. Since the polymerization rate is faster than depolymerization, the ParB binders become quickly saturated ($A = A^*$) so the x_c movement is solely controlled by the balance between F and thermal motion, which quickly creates large tails in ParB distributions and ParA tip distributions. However, the load F operates to oppose the motion of ParB toward the complex, so as the ParA bundle grows, the ParB complex is eventually pushed to the ParA edge due to the load. As a result, we see that when the ParA bundle is polymerizing the ParB complex will follow,

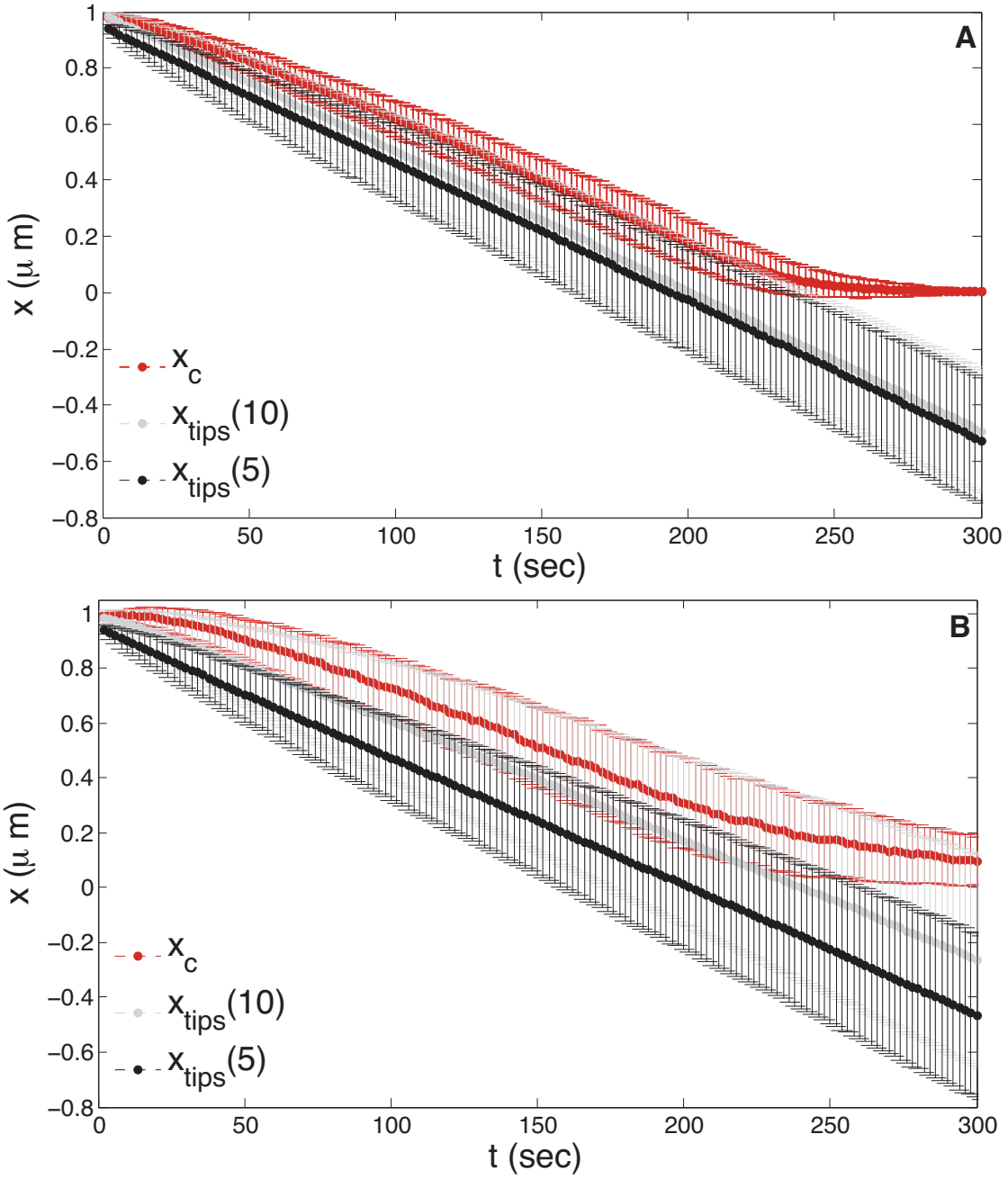

Figure 4.7. Average x_c, $x_{\text{tips}}(5)$, and $x_{\text{tips}}(10)$ versus time for a polymerizing ParA bundle. Each point in the plot is obtained by averaging the data from 500 solution trajectories of eqs. (4.5)-(4.6). The bars mark standard deviation. The parameters are $\beta_0 = .5\ \text{s}^{-1}$, $\alpha = 1\ \text{s}^{-1}$. A. For $\beta = .05\ \text{s}^{-1}$, ParA tips grow quickly, saturating the ParB binders, which pushes the complex to the growing ParA edge. The distance between average extremal tip positions remains constant because the ParA tips are uniformly growing. Diffusion relocates ParBs causing x_c to have quickly increasing tails. B. For $\beta = .5\ \text{s}^{-1}$, some ParA tips grow toward the old pole while the tips proximal to the new pole are left behind with the ParB binders.

thus further confirming that ParB movement is directly dependent upon ParA polymer dynamics.

In Figure 4.7B we plot model solutions when $\alpha = \beta + \beta_0$. In this case the total depolymerization rate of ParA tips that overlap with ParB matches the ParA polymerization rate. For the ParA tips which are in contact with ParB there is no net movement due to polymerization/depolymerization because $\alpha = \beta + \beta_0$. However, the ParB complex, driven by $\Psi(A)$, will try to relocate on the bundle in order to increase A. This ParB motion will undoubtedly leave some ParA tips behind, which start growing as soon as they lose overlap. In Figure 4.7B we see that indeed the distance between $x_{\text{tips}}(5)$ and $x_{\text{tips}}(10)$ is much larger when $\alpha = \beta + \beta_0$ in Figure 4.7B. This large gap in tip positions is reflected in a quick spreading of PaB distributions over the ParA polymer lattices as the complex struggles to push toward the new pole by holding on to a few tips with large A. As a result of the erratic ParB motion, the polymerization rate α will overcome depolymerization, slowly moving the tips and the ParB complex to the old pole.

The ParB movement seen in this model when $\alpha > \beta_0$ gives us an idea as to what happens when ParA polymerization rates are not tightly controlled. ParB segregation to the new pole directly depends on how fast ParA grows or shrinks. More specifically, when ParAs manage to grow toward the old pole, ParB fails to segregate the chromosome to the new pole. Because the pool of monomers in this discrete model is assumed to be large enough to warrant polymerization independent of the amount of ParA monomers in solution, we see that if given enough monomers the ParA tips will grow pulling ParB to the old pole. Since the pool of ParA monomers in bacterial cells is constant [5] the growth of polymers shown in this discrete model is not a physiologically relevant property. However, the simulations with $\alpha > 0$ give us an opportunity to correlate ParB movement with ParA filament dynamics. From our model results we expect that the observed erratic motion with poleward trips of ParB when $\alpha > \beta_0$ along with ParA filaments appearing behind ParB will be a prevailing feature of movement when ParA is allowed to freely polymerize. Indeed, in $\triangle$tipN experiments ParA polymers grow behind ParB and ParB shows stalled and frequent backward movement [5]. Our model results seem to indicate that chromosome movement can be controlled in the cell by modulating the ParA polymerization/depolymerization rate balance. Proteins which interact with ParA monomers in the cell, such as TipN, would thus be a natural candidate for ParB movement control. In the next section we will explore mechanisms by which TipN can operate in *C. crescendus* cells.

In conclusion, our model has reproduced some key characteristics of ParB/ParA in-

teractions that are seen in *C. crescendus* cells. We have shown that if the ParB/ParA binding forces are formulated such that they bias ParB diffusion to maximize the amount of ParB/ParA overlap, a chromosome will track both a polymerizing and depolymerizing ParA bundle with velocities that closely match ParA rates. Thus, we have proposed a simple mechanism where weak binding due to multiple ParB binder interactions biases diffusion in order to keep the ParB complex on the edge of a retracting polymer bundle. We also saw that if the rates at which ParB depolymerizes the bundle are comparable to the natural ParA depolymerization rates, the ParA bundle will have significant tails as the ParB complex erratically approaches the new pole. This kind of behavior is not in agreement with experiments which show that the ParA bundle has small retracting tails as ParB segregates the chromosome in the cell. Thus, from this first simple model we predict that fast ParB depolymerization is not necessary to drive chromosome motility in *C. crescendus*. Instead, the dynamics of ParA polymerization/depolymerization and biased diffusion are sufficient to reproduce the desired motility. This model result is very similar to our kinetochore model result in which weak binding and microtubule depolymerization were sufficient to drive motility.

4.4 Continuous model for chromosome segregation in *C. crescendus*

In this section, we use some of the results from the discrete model for ParB/ParA interactions in order to develop a continuous model which tracks the complete segregation apparatus of *C. crescendus*. We start by listing assumptions that are specific to the continuous model.

A *C. crescendus* cell is assumed to be a cylinder of length L. Since ParB experiences little motion along the width of the cylinder and the ParA bundles also localize along the length of the cell, we ignore any ParB movement or ParA dynamics along the width of the cell. Thus, for this model we keep track of ParB location and ParA concentrations along the x-axis which starts at the old pole ($x = 0$) and ends at the new pole ($x = L$), as depicted in Figure 4.1.

The ParA bundle has varying filament densities along the cell, which must be properly projected on the x-axis. In this model we track the ParA bundle filament cross sectional density denoted by $A(x)$ (note that $A(x)$ here is different from the overlap $A(x)$ described in the previous model). So, the function $A(x)$ gives the total number of ParA filaments found in the *C. crescendus* cell cross section at position x. For the rest of this discussion we redefine

$A(x) = A(x)/A_0$, where A_0 is the maximal number of filaments that can make up a bundle cross section in the cell at $t = 0$ (i.e., A_0 marks the initial ParA bundle thickness). From physical considerations we initialize the ParA bundle density with a saturating function as depicted in Figure 4.8A.

We are now ready to formulate the binding energy well function, Ψ. As before, each ParB binder element is assumed to have affinity for a ParA bundle filament. Thus, for a ParB binder/filament interaction we assume that there is a free energy drop of $-a$. However, at a position x, ParB encounters and interacts with multiple filaments so that the total energy is given by $-aA(x)$. It follows that the energy of binding at a position x is described by the unit energy function $\psi(x) = -aA(x)$, which describes the energy of ParB/ParA binding at a cell cross section. The function ψ is shown in Figure 4.8B.

Qualitatively, the unit energy function of a ParB binder interacting with a ParA filament, $\psi(x)$ is very similar to the unit energy functional we assumed for kinetochore binders interacting with a microtubule. In contrast to the energy function for kinetochores, for the $\psi(x)$ presented here we have not distinguished among specific binding sites on the ParA lattice. This is because we are assuming that ParB has nonspecific affinity for the bundle

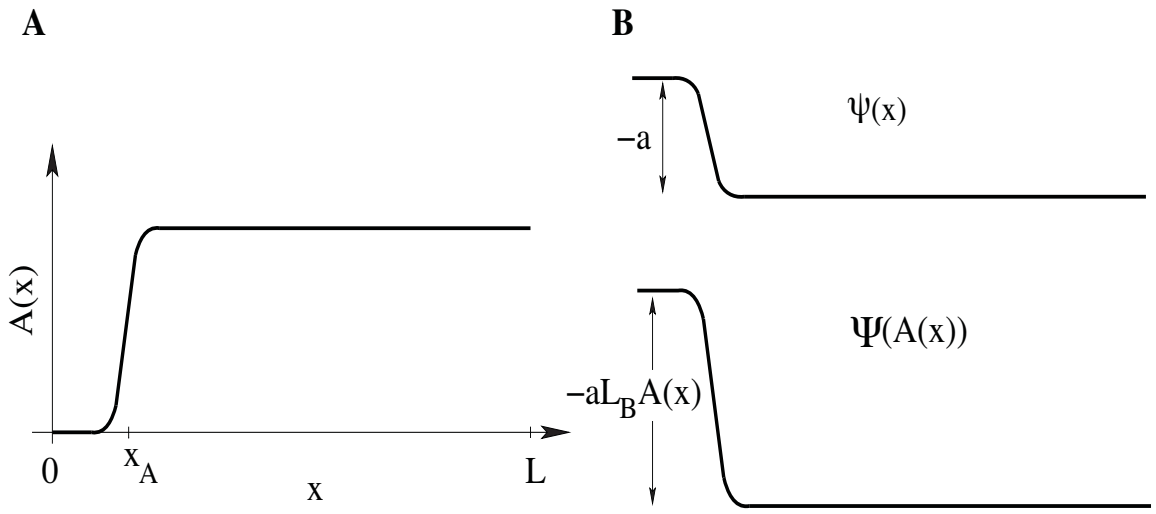

Figure 4.8. $A(x)$ and a diagram of the ParB binding energy function, $\Psi(A)$. A. The function $A(x)$ represents the cross sectional density of the ParA bundle. For our simulations we set $x_A = 0.5$ μm. B. When a ParB binder associates with a ParA filament the system free energy decreases by $-a$. The total amount of energy is dependent upon the total number of filaments that a ParB complex can bind so $\Psi = -aL_B A(x)$ is a function of ParA bundle filament density.

filaments.

The total energy of binding of the ParB complex is calculated as the sum of all the unit energy functions over the length L_B of the ParB complex. So we write

$$\Psi = \int_{x-L_B}^{x} \psi(x)dx, \tag{4.7}$$

$$= -a \int_{x-L_B}^{x} A(x)dx. \tag{4.8}$$

Note that in the above calculation there is an inherent assumption that ParB binders are sufficiently dense on the complex to warrant integration. Also, x here marks the position of the front edge of the ParB complex (equivalent to $x_c + L_B$ in the discrete model). Since the length of the ParB complex is small compared to the length of the cell ($L_B << L$) we can further simplify eq. (4.8) to obtain

$$\Psi(A) = -aL_B A(x). \tag{4.9}$$

Observe that the expression in eq. (4.9) gives us a direct relationship between the cross sectional density of ParA bundle filaments and the energy of binding. Indeed, if the density of filaments in the bundle is increased, then the ParB complex will reach more filaments and the free energy is lowered accordingly. However, the total amount of energy arising from the binding interaction must be capped off since the binders on ParB will eventually be all occupied. In order to achieve this we construct a saturating function

$$K(A) = \begin{cases} A & 0 < A < A^* \\ A^* & A \geq A^*, \end{cases} \tag{4.10}$$

and the binding energy now reads

$$\Psi(A) = -aL_B K(A). \tag{4.11}$$

Note the similarity between $\Psi(A)$ given here (see Figure 4.8B) and the Ψ we derived for kinetochores in Chapter 2. Both energy functions, Ψ level off after the motor binders are fully occupied. However, for the *C. crescendus* case there are no individual ParA binding sites on the polymers, which removes the high frequency oscillations from the potential energy well. Also, the transition from the biased (decreasing) part of the well to the unbiased (flat) for *C. crescendus* is not directly dependent on position but instead on A^*, the cross sectional density. This is because the ParB motor is bound to multiple ParA filaments as

opposed to a single linear MT polymer for kinetochores. We choose $A^* = 1$, which saturates the ParB binders sites at A_0.

A note is in order about the binding force term $\Psi'(A)$. The binding force in this model is directly proportional to A_x. The term A_x is a measure of the density of exposed ParA filament tips along the x-axis. Thus, binding forces on the complex can increase if depolymerization of the ParA bundle is such that the exposed filament tip density increases. Recall that the binding force Ψ' for this model has the same tip density dependence as the discrete model binding force. We conclude the discussion of the binding energy function by defining $aL_B = 3$ pNμm for the binding energy, in order to match the forces from the discrete model described in the previous section.

ParA monomers are assumed to undergo an ATP-dependent dimerization reaction in solution. We track the concentration of monomers with $AM(x)$ and the concentration of dimers with $AD(x)$. In the equations for AM and A we must be careful to conserve total volume, so we set

$$\text{total bundle volume} = \text{total monomer volume} \tag{4.12}$$

$$\chi \int A(x)dx = V_m \int AM(x)dx \tag{4.13}$$

$$A = \delta_m AM, \tag{4.14}$$

with V_m the monomer volume and χ the filament cross sectional area.

Finally, TipN affects ParA dynamics in the cell by accumulating high ParA monomer concentrations at the new pole. It is not clear how TipN interacts with the ParA proteins so we explore two modes of TipN activity : 1) sequestration, 2) nucleation. For the first case, TipN is assumed to bind and thus remove ParA monomers from the cytoplasm so that they cannot return to the ParA bundle. This mode of TipN operation is based on the experimental observations of [5]. However, it has been very recently proposed that the TipN protein might not only capture the monomers but also facilitate a nucleation reaction at the new pole [3]. In this second scenario, once sequestered by TipN at the new pole, the monomers are allowed to recruit dimers from solution in order to nucleate polymers. A TipN nucleated polymer may undergo depolymerization if in contact with ParB, like the rest of the ParA bundle. TipN has been shown to be essential in order to maintain ParB directionality during cell division. Experimental evidence points that there might be a compensatory mechanism that mediates sequestration of monomers at the old pole when TipN is removed. The protein PopZ, which mediates the tethering of ParB to the poles and been shown to also directly interact with ParA monomers in a fashion that is very similar

to TipN [5]. Due to the similarity of PopZ with TipN we do not directly model its activity; however, we discuss our predictions for how this protein affects chromosome motion when we present model results.

Based on the above assumptions we write the following system of equations for interactions between ParA and ParB in a dividing *C. crescendus* cell:

$$\frac{1}{\delta_m}\frac{\partial A}{\partial t} = \alpha|A_x|AM - \beta_0|A_x| + \kappa_n k_{tip}(x)AM - \frac{\beta\gamma|A_x|}{K_a+|A_x|}\int_x^{x+L_B} p_B(x)dx, \tag{4.15}$$

$$\frac{\partial p_B}{\partial t} = -\frac{1}{\nu}\frac{\partial}{\partial x}\Big((-\Psi'(A)-F)p_B\Big) + D_B\frac{\partial^2 p_B}{\partial x^2}, \tag{4.16}$$

$$\frac{\partial AM}{\partial t} = -k_A AM^2 + \beta_0|A_x| - k_{tip}(x)AM + \frac{\beta\gamma|A_x|}{K_a+|A_x|}\int_x^{x+L_B} p_B(x)dx + D_A\frac{\partial^2 AM}{\partial x^2}, \tag{4.17}$$

$$\frac{\partial AD}{\partial t} = k_A AM^2 - \alpha|A_x|AD + D_A\frac{\partial^2 AD}{\partial x^2}. \tag{4.18}$$

In eq. (4.15), eq. (4.17) and eq. (4.18), the polymerization and depolymerization terms are multiplied by $|A_x|$ to enforce that monomer addition or removal at filament tips.

The location of ParB is tracked probabilistically with a Fokker-Planck equation in eq. (4.16), where p_B is the probability density function for locating the complex ParB at position x at time t. So, the depolymerization rate β is multiplied by the probability of finding ParB in position x. Further, since the total number of ParB binders is finite, the ParB depolymerization rate that arises due to ParB association with ParA is modeled with a saturating function of the form $\gamma\beta|A_x|/(K_a+|A_x|)$ (for simplicity, we normalize $\gamma = 1$ μM/μm).

The TipN protein is introduced in the model equations with the help of a position dependent polymerization rate function $k_{tip}(x) = \text{kTipN}\exp(-25(x-L)^2)$, which peaks at $x = L$ where TipN is found. The function $k_{tip}(x)$ is plotted in Figure 4.9.

Finally, for small L_B, the model equations can be further simplified to remove the integral terms in the ParB depolymerization rates as follows

$$\frac{1}{\delta_m}\frac{\partial A}{\partial t} = \alpha|A_x|AD - \beta_0|A_x| + \kappa_n k_{tip}(x)AM - \frac{\beta L_B|A_x|}{K_a+|A_x|}p_B, \tag{4.19}$$

$$\frac{\partial p_B}{\partial t} = -\frac{1}{\nu}\frac{\partial}{\partial x}\Big((-\Psi'(A)-F)p_B\Big) + D_B\frac{\partial^2 p_B}{\partial x^2}, \tag{4.20}$$

$$\frac{\partial AM}{\partial t} = -k_A AM^2 + \beta_0|A_x| - k_{tip}(x)AM + \frac{\beta L_B|A_x|}{K_a+|A_x|}p_B + D_A\frac{\partial^2 AM}{\partial x^2}, \tag{4.21}$$

$$\frac{\partial AD}{\partial t} = k_A AM^2 - \alpha|A_x|AD + D_A\frac{\partial^2 AD}{\partial x^2}. \tag{4.22}$$

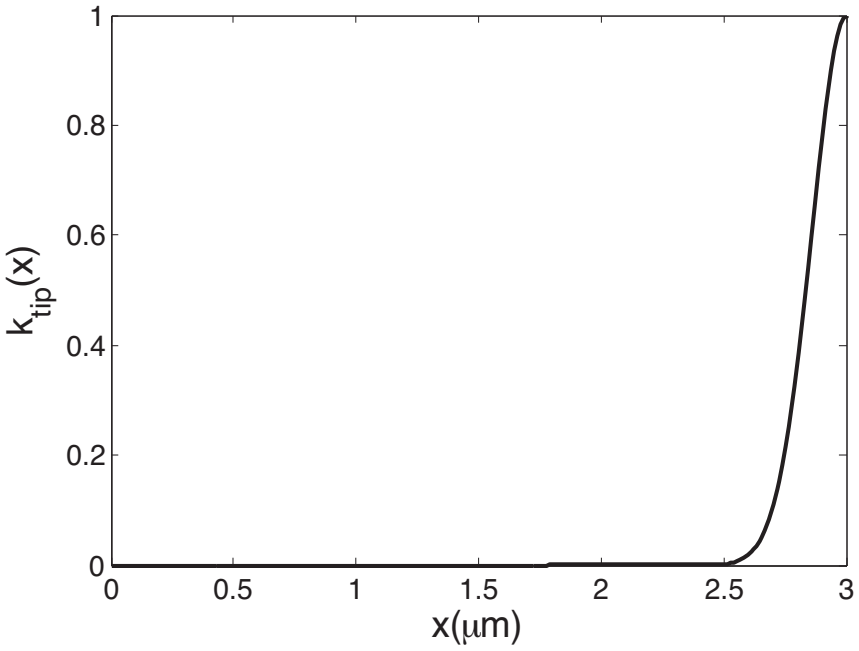

Figure 4.9. A plot of the function $k_{tip}(x)$. The sequestration function for TipN is given by $k_{tip}(x) = \text{kTipN}\exp(-25(x-L)^2)$. In this plot we have set kTipN= 1.

The term κ_n is set to zero when we consider the TipN sequestration model and otherwise set to one when we consider the TipN nucleation model. In the following sections we discuss results from numerical simulations of the model equations. For the simulations we use no-flux conditions for ParB, ParA monomers, and ParA dimers at the boundaries $x = 0, L$.

4.4.1 Chromosome segregation without polar ParA accumulation

In this section, we test the dependence of ParB movement on ParA bundle polymerization/depolymerization rates. Therefore, we ignore ParA monomer sequestration and ParA dimerization is assumed to be instantaneous, so that only ParA monomers are tracked in the cytoplasm. With these assumptions, the model equations read

$$\frac{1}{\delta_m}\frac{\partial A}{\partial t} = \alpha|A_x|AM - \beta_0|A_x| - \frac{\beta L_B|A_x|}{K_a + |A_x|}p_B, \tag{4.23}$$

$$\frac{\partial p_B}{\partial t} = -\frac{1}{\nu}\frac{\partial}{\partial x}\Big((-\Psi'(A) - F)p_B\Big) + D_B\frac{\partial^2 p_B}{\partial x^2}, \tag{4.24}$$

$$\frac{\partial AM}{\partial t} = -\alpha|A_x|AM + \beta_0|A_x| + \frac{\beta L_B|A_x|}{K_a + |A_x|}p_B + D_A\frac{\partial^2 AM}{\partial x^2}. \tag{4.25}$$

In Figure 4.10 we show model solutions for a depolymerizing ParA bundle ($\beta_0 = 0.5$ s^{-1}, $\alpha = 0$) and varying depolymerization rates, β for the ParB complex.

As can be seen from the plots for $p_B(x)$ and $A(x)$ in Figure 4.10A, when $\beta << \beta_0$, the ParB distributions closely follow the ParA bundle edge as it depolymerizes toward the new pole. The ParA bundle density, $A(x)$ shows almost wave-front movement with edges that slightly lose steepness over time. The reason for this smoothing effect is the same as in the discrete model. The ParB complex sits at the bottom of the Ψ well, which localizes close to $A(x) = 1$. The positioning of the ParB complex ahead of the ParA tips causes faster depolymerization close to $A = 1$, as compared to $A = 0$. This discrepancy in the depolymerization rates of the ParA bundle moves some ParA filament tips farther ahead of the bundle edge. The ParB complex distributions also experience stronger diffusion effects as $A(x)$ retracts, because as time progresses, A_x decreases causing a decline in the magnitude of Ψ'. This is shown by the smaller peaks and larger distribution tails of p_B as it approaches the new pole in Figure 4.10A. Note that due to the decline in p_B peaks as ParB approaches the new pole, high loads F will eventually cause the ParB complex to detach. We thus expect that for a depolymerizing ParA filament bundle interacting with a ParB complex, the likelihood of ParB detaching under load increases as the ParA bundle gets shorter. This prediction is in agreement with the experimental observations and assumptions of [4] in *E. coli* plasmids. However, here we present a mechanistic reasoning for why ParB detachment rates should increase for shorter ParA bundles. In *C. crescendus*, the increased detachment probability due to low ParA binding site densities at the new pole is remedied by PopZ, which has been shown to anchor ParB at the new pole to prevent movement reversals.

In panels B and C of Figure 4.10, we repeat our simulations with the same β_0, but with higher ParB depolymerization rates, β. These plots indicate that an increase in β causes the ParB complex to depolymerize the front edge of $A(x)$ faster, thus creating a faster overall decay in A_x over time. In response the ParB complexes experience stronger diffusive effects with the p_B distributions having lower peaks as compared to the distributions shown in panel A. The gentle linear indentations on the ParA bundle for panels B and C in Figure 4.10, are due to large differences in β_0 and $\beta + \beta_0$. When there is faster monomer removal by ParB, more tips are exposed ahead of the ParA bundle edge to which ParB can bind and depolymerize. In response, p_B will spread at the front of the ParA bundle to bind the tips that have been quickly shortened. Due to the small constant A_x, ParB will bind these sites with equal probability so the p_B distributions attain an almost box-like shape. This feature

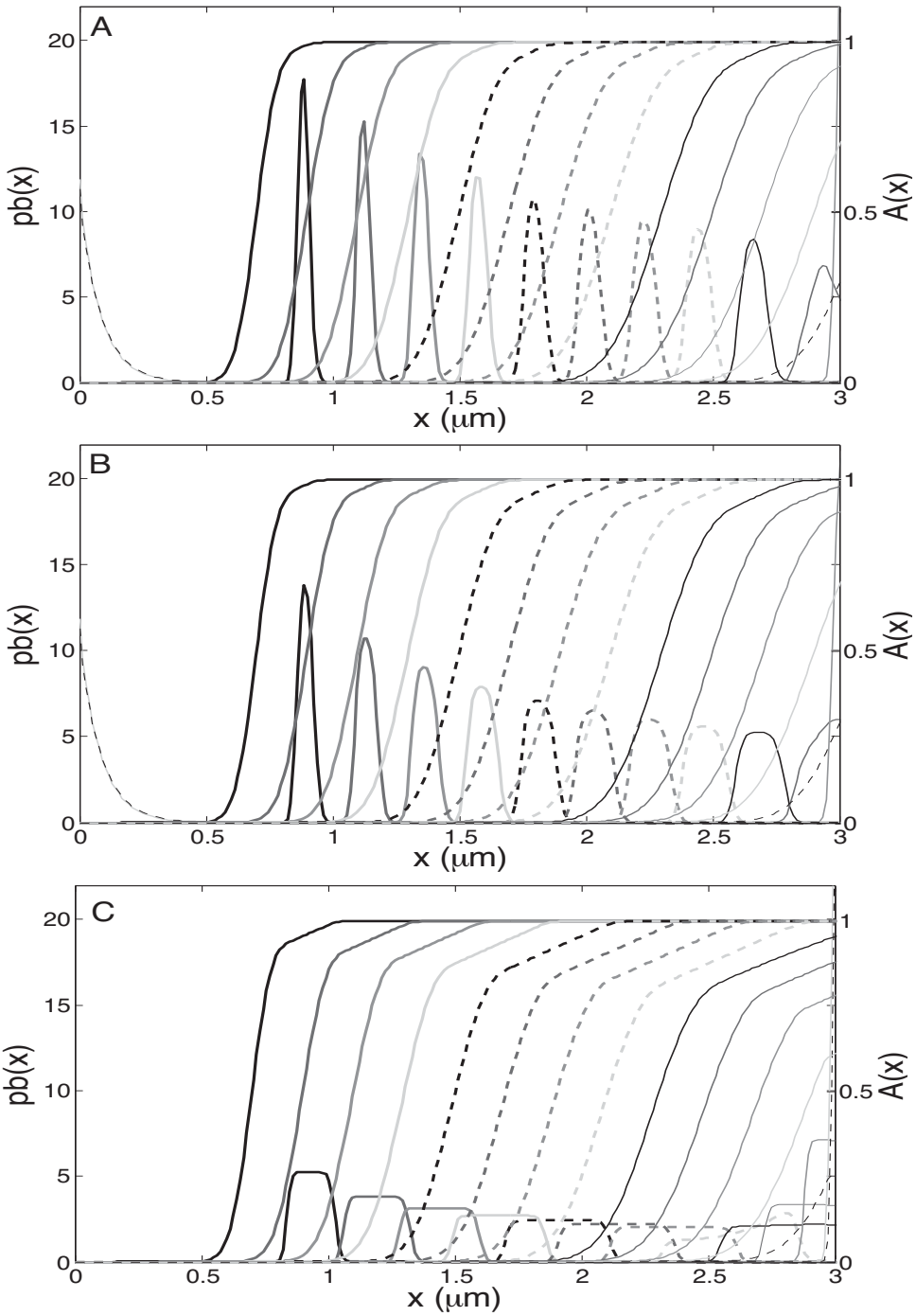

Figure 4.10. Plot of $p_B(x)$ and $A(x)$ for depolymerizing ParA bundles. Each solution is shown after $t = .67$ min for a total of 10 min. $\Psi(A)$ pushes ParB ahead of the ParA bundle edge. The parameters used are $\beta_0 = .5$ s^{-1} and $\alpha = 0$. A. $\beta = .05$. The ParB distributions follow the ParA bundle closely since $\beta < \beta_0$. B. $\beta = .1$. ParB distributions move slightly ahead of the ParA bundle edge. C. $\beta = .5$. ParB distributions move significantly ahead of the ParA bundle edge since the complex removes monomers with $\beta = \beta_0$.

is particularly prominent in panel C where the p_B peaks spread over .5 μm ahead of the ParA edge. The shape of the ParB distributions for $\beta = \beta_0$ indicates that ParB complexes have equal probabilities of moving closer to the new pole or away from the new pole, so that ParB complexes experience erratic motion as they segregate.

From the plots in Figure 4.10, we see that an increase in ParB rates works against the ParB complex. By quickly decaying the front edges of $A(x)$, ParB complexes can quickly advance toward the new pole without fully degrading the bundle which causes p_B to spread its peaks and diffuse out ahead of the ParA bundle edge. We therefore conclude from these simulations that a ParB complex composed of multiple binders can hold on and move with a depolymerizing ParA bundle edge, provided that the ParB depolymerization rates are small compared to β_0. In lieu of the experimental data, which show ParB closely trailing a depolymerizing ParA bundle with no movement reversals, we favor a scenario where ParB slowly depolymerizes the ParA filaments and waits for the natural depolymerization rate to move both the complex and the ParA bundle front. In this scenario ParB has a passive depolymerization role. The results obtained thus far are in complete agreement with our discrete model results.

Next, we repeat our simulations in the case when the ParA filaments are allowed to polymerize with $\alpha > \beta_0$, i.e when the ParA bundle is in polymerization mode. This scenario is important to consider since from experiments it is seen that if free ParA monomers are around, then ParA filaments will tend to grow. Thus, in a wild type cell we expect $\alpha \neq 0$. Simulation results for polymerizing ParA bundles are shown in Figure 4.11.

As can be seen from Figure 4.11A, when $\beta << \beta_0$, the ParA bundle initially moves closer to the new pole until the monomer pool is large enough to allow for polymerization of the ParA bundle filaments. Then, the ParA bundle experiences growth toward the old pole with tips close to $A = 0$ growing the fastest due to no overlap with ParB. This ParA growth causes a fast decay in A_x and a subsequent spreading of p_B distributions due to diffusion. The end result is that ParB complexes with slow ParB depolymerization rates first move toward the new pole, then experience a significant slow down (almost stalling) followed by higher probabilities for toward and away movement from the new pole. In this case, it is clear that the natural depolymerization rate β_0 cannot rescue ParB from slowly depleting the concentration for ParA filament tips that it can bind to. The ParB complex thus fails to segregate. If given enough time, the ParA edge will decay and significantly decrease A_x, so the ParB distributions detach and move close to the old pole under the load, F. Next, from the simulation results in Figure 4.11B and 4.11C, we conclude that ParBs fail

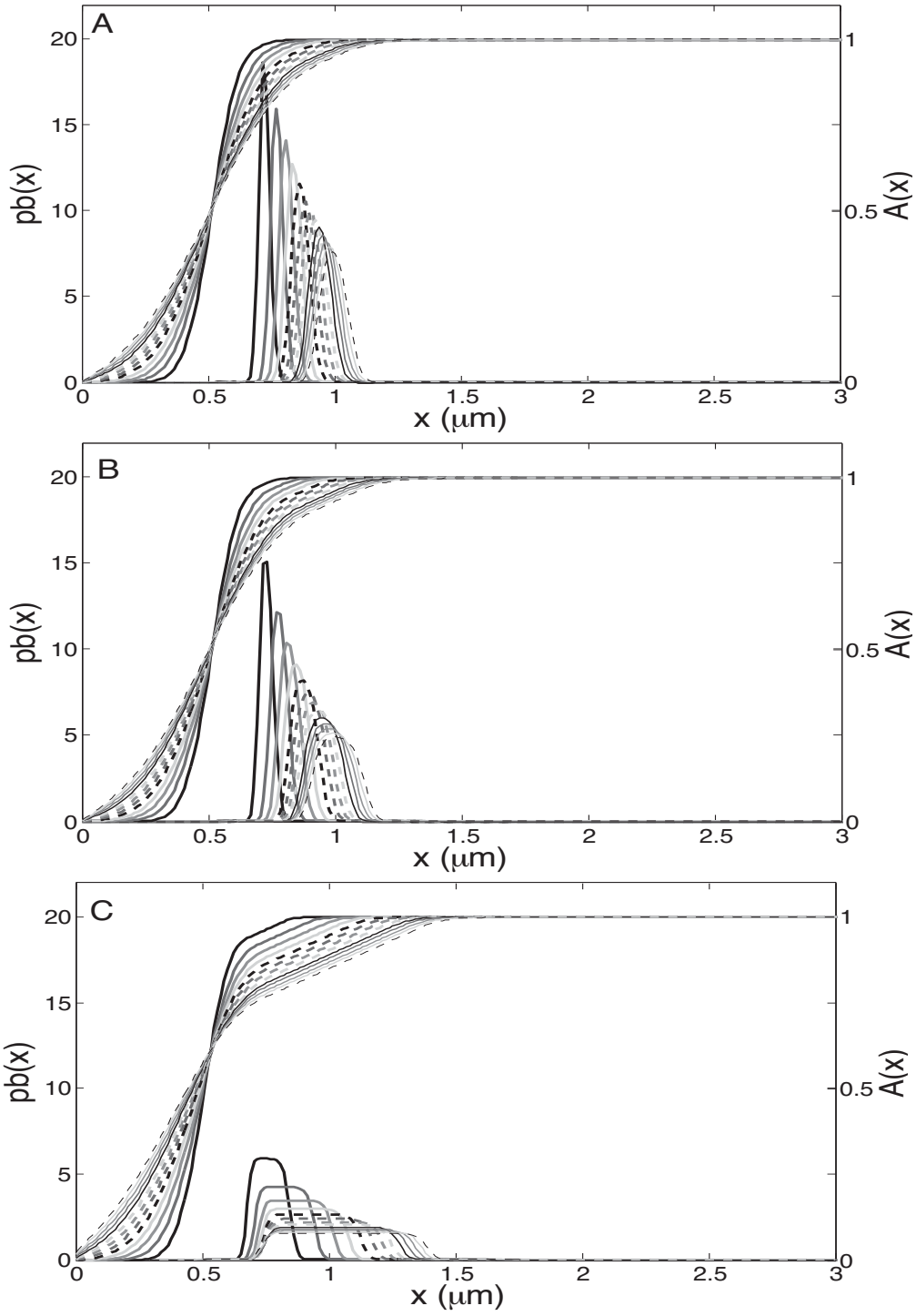

Figure 4.11. Plot of $p_B(x)$ and $A(x)$ for polymerizing ParA bundles. Each solution is shown after $t = .67$ min for a total of 10 min. The ParB complexes slow down after an initial new pole approach. The parameters used are $\beta_0 = .5$ s^{-1} and $\alpha = 1$ s^{-1} μM^{-1}. A. $\beta = .05$. ParB distributions initially follow the ParA bundle closely and then slow down. B. $\beta = .1$. The ParB fail to segregate despite higher β. C. $\beta = .5$. ParB distributions localize ahead of the ParA bundle edge, but also fail to segregate.

to segregate if ParA monomers are quickly returned to the bundle independent on how fast ParB depolymerizes. The main difference for higher β is that the p_B distributions spread out further and faster in the cell indicating that the ParB complexes experience highly erratic motion closer to the new pole. It is important to highlight that in all simulation results presented in Figure 4.11, we see that ParA polymers will always appear between the old pole and the ParB complex.

From the model solutions considered so far, we predict that ParA bundle dynamics are extremely important to assuring proper segregation in the *C. crescendus* cell independent of ParB depolymerization. First, we saw that when the ParA bundle is allowed to freely depolymerize ($\alpha = 0$), then the ParB complex will move toward the new pole. If in addition ParB is slow at depolymerizing, the movement of the chromosome closely tracks ParA bundle edges and moves unidirectionally, in agreement with wild type cell observations. From our model results, we also see that if the bundle polymerization rate, α is not tightly controlled proper chromosome segregation is lost. More specifically, when $\alpha > \beta_0$, the ParB complex first moves toward the new pole, then it is overcome by polymerization and it will very slowly move toward the new pole essentially stalling as it undergoes erratic motion due to diffusion of ParB on ParA filament tips. In these cases, ParA will appear behind ParB and grow toward the new pole. Our model predictions are in agreement with experimental observations. When TipN is deleted, ParB complexes first move toward the new pole and then slow down and experience frequent reversals in direction while ParA filaments appear behind ParB [3]. In $\triangle$tipN $\triangle$popZ cells where all polar interaction with ParA is removed, which is the direct equivalent to our results above with $\alpha > \beta_0$, the slow erratic motion of ParB eventually results in complete failure of segregation with ParB return to the old pole [5]. Thus, we believe that the mechanism proposed in our model may be a good representation of what is happening in dividing *C. crescendus* cells.

In conclusion, we predict that segregation will be restored if the polymerization rates of the ParA bundle are properly controlled. Since polymerization rates for ParA filaments are monomer concentration-dependent, it follows that cytoplasmic ParA monomer concentrations need to be tightly controlled to allow for chromosome segregation. In the next section, we discuss mechanisms by which ParA monomer concentrations can be controlled in dividing *C. crescendus* cells.

4.4.2 Chromosome segregation with TipN and ParA dimerization

So far we have not taken into account that the ParA monomers, released due to depolymerization, are required to dimerize before returning to the ParA bundle. Recent experimental evidence seems to indicate that ParA monomers may undergo conformational changes [6] before dimerizing in the cytoplasm. This data suggests that there is a delay in the polymerization of ParA filaments once monomers are in solution. We introduce such a delay by adding the dimerization term in the model equations with $k_A = 1/3$ min^{-1} μM^{-1} (note that k_A is chosen to be much smaller than α).

In Figure 4.12 we show model solutions when dimerization is allowed with $k_A = 1/3$ min^{-1} μM^{-1} and there is no ParA monomer interaction with polar proteins (kTipN=0).

From the $A(x)$ and $p_B(x)$ solutions in Figure 4.12 we see that when dimerization is added, the ParB complex initially experiences slow motion toward the new pole. The ParB

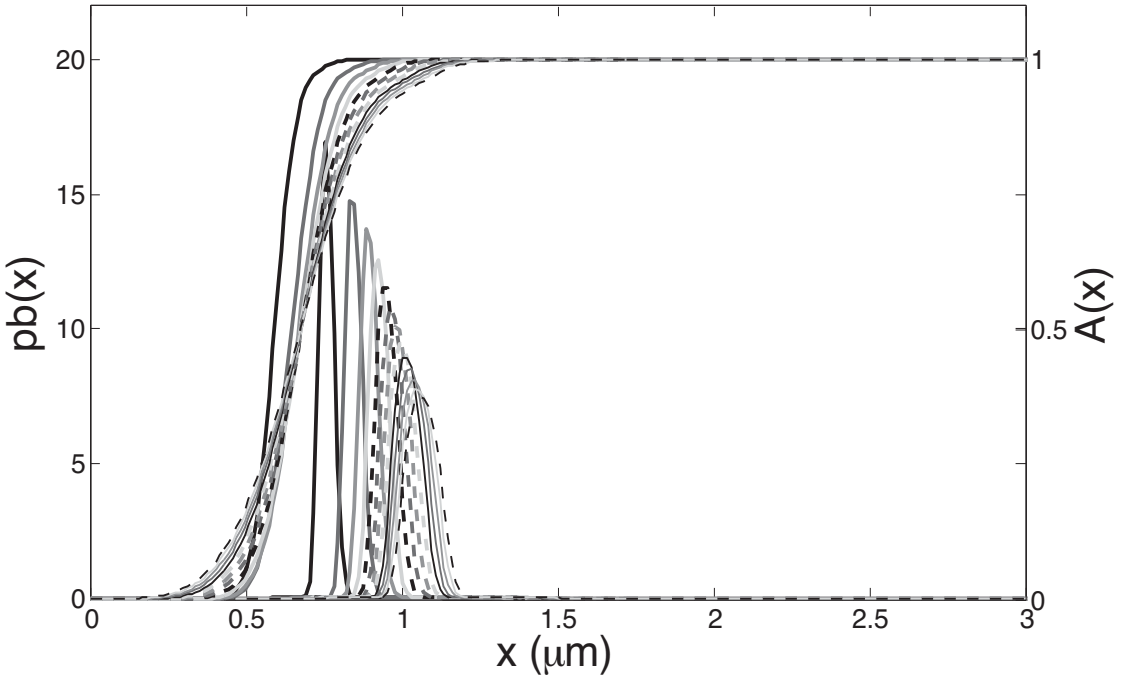

Figure 4.12. $p_B(x)$ and $A(x)$ when ParA monomers dimerize in the cytoplasm. Each ParA profile and ParB distribution solution is shown after $t = .67$ min of simulation for a total of 10 min. Despite the delay from dimerization, if ParA monomers are not removed from the cytoplasm, the ParB complexes fail to find the new pole in the allotted time and will eventually become stalled. The parameters are $\beta_0 = .5$ s^{-1}, $\beta = .1$ s^{-1},$\alpha = 1$ s$^{-1}\mu$M^{-1}, $k_A = 1/3$ min^{-1} μM^{-1} and kTipN= 0.

distributions in this case move closer to the new pole and retain their peaks better than in Figure 4.11B, where no dimerization delay was present. However, even in this case when the dimer concentrations are sufficiently high, $A(x)$ will grow toward the old pole. As a consequence, the ParB complex will fail to segregate the chromosome in the same time frame as when ParA bundles are allowed to freely depolymerize. Thus, unless the dimerization delay is long enough to allow for full chromosome segregation (which from experiments seems that it is not [6]), the monomers in solution need to be somehow removed or recycled in locations that do not prevent ParB from moving with a depolymerizing ParA bundle. This monomer sequestration or nucleation action is precisely what TipN is hypothesized to do.

We start by testing the model of [5], where TipN is assumed to sequester ParA monomers from the cytoplasm. To this end, we introduce TipN in the model using the rate function $ktip(x)$ and $\kappa_n = 0$, indicating that the monomers are not returned to the ParA bundle after being sequestered. In Figure 4.13 we show model results when ParA dimerizes and TipN sequesters monomers out of the solution.

As can be seen from the plot in Figure 4.13, the delay from ParA dimerization coupled with fast TipN monomer sequestration fully restore segregation of the *C. crescendus* chromosome in the cell. Thus, in this model TipN is essential to warrant segregation.

Next, we test the hypothesis where TipN not only sequesters monomers but also assembles them onto the existing ParA bundle so that dimers can be recruited and new ParA filaments are formed. We simulate our model with $\kappa_n = 1$ and the results are plotted in Figure 4.14.

The plots in Figure 4.14 show that the introduction of the nucleation action from TipN creates new ParA bundle filaments at the new pole. The TipN-generated filaments grow with rate α. The ParB complex segregates the chromosome due to the delay in dimerization coupled with the monomer recruitment from TipN. We note that the main difference between the nucleation and the sequestration model for TipN operation has to do with the shape of the ParB probability density solutions, p_B. In the case when TipN only sequesters monomers, the shape of p_B is identical to the distributions of depolymerizing ParA filaments in the previous section. Accordingly, the distributions diffuse out as the ParA tip density is decreased. In the case of nucleation, the tip density is kept high close to the new pole due to the addition of TipN nucleated polymers. Thereby, TipN nucleation keeps the p_B distributions sharply focused on the ParA edge even when close to the new pole (A_x is large close to the new pole as TipN nucleates). Thus our model predicts that the

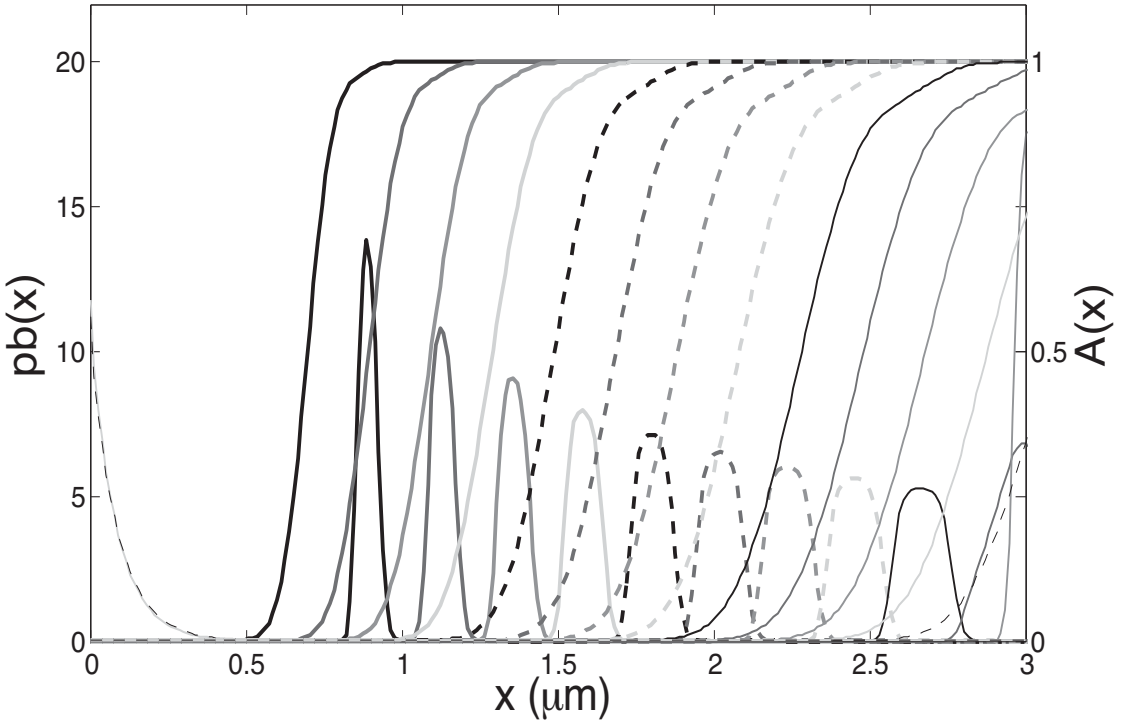

Figure 4.13. $p_B(x)$ and $A(x)$ for the TipN sequestration model. Each solution is shown after $t = .67$ min for a total of 10 min. The addition of TipN sequestration removes ParA monomers from the cytoplasm so that the ParA bundle depolymerizes and ParB follows to the new pole. Segregation is completely restored. The parameters are $\beta_0 = .5$ s^{-1}, $\beta = .1$ s^{-1} and $\alpha = 1$ s$^{-1}\mu$M^{-1} , $k_A = 1/3$ min^{-1} μM^{-1}, and kTipN= 5 s^{-1}.

probability of late filament detachment is lowered when TipN nucleates ParA filaments at the new pole, supporting a more robust segregation mechanism. Both TipN models restore segregation, with accumulation of either monomers or generation of polymers at the new pole. In both cases our model indicates that there is a large concentration of ParA protein at the new pole when TipN is working. These results are in agreement with experiments where the addition of TipN to $\triangle$tipN and $\triangle$popZ fully restored segregation and accumulations of ParA proteins were observed at the new pole [5].

We conclude this section by remarking on the role of the compensatory protein PopZ. As discussed in Chapter 1, when TipN is removed from cells, there is slow accumulation of ParA protein at the old pole. Since PopZ is postulated to work similarly to TipN in [5], we expect that PopZ works by slowly sequestering monomer from the cytoplasmic pool. This PopZ action would introduce a delay in the build-up of ParA monomers in solution and thus a delay in the growth of ParA bundles. From our model results with $\beta_0 < \alpha$, we expect that

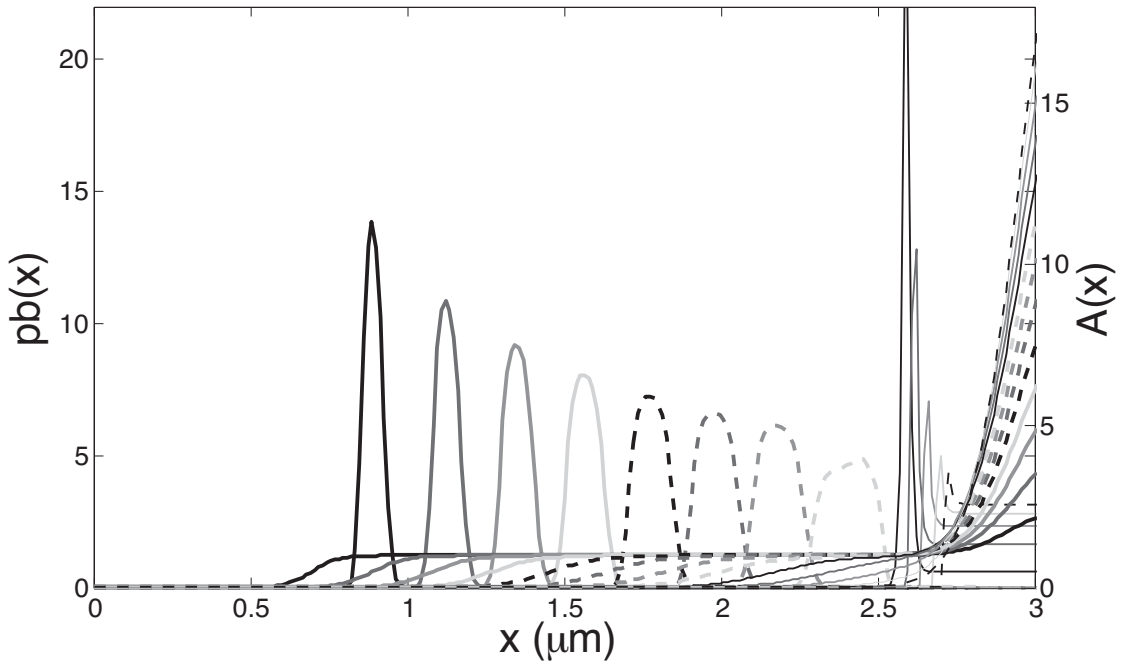

Figure 4.14. $p_B(x)$ and $A(x)$ for the TipN nucleation model. Each solution is shown after $t = .67$ min for a total of 10 min. The addition of TipN nucleation not only removes ParA monomers from cytoplasm but also adds new filaments to the bundle. The ParA bundle depolymerizes and ParB follows to the new pole with densities that retain their peaks as they get close to the new pole due to the TipN-nucleated ParA filaments. Segregation is also completely restored in this model. The parameters are $\beta_0 = .5$ s^{-1}, $\beta = .5$ s^{-1} and $\alpha = 1$ s$^{-1}\mu$M^{-1} , $k_A = 1/3$ min^{-1} μM^{-1}, and kTipN$= 5$ s^{-1}.

when PopZ is operating ParB will initially approach the new pole, then it will slow down and eventually move toward and away from the new pole as the ParA bundle grows. In this case the chromosome might be segregated if it the erratically moving ParB is anchored at the new pole by PopZ. These predictions are in agreement with experimental observations in TipN depleted cells [5]. It is not clear whether and how PopZ nucleates ParA filaments, so further experimental data is needed to clarify the action of this protein. Note that in the PopZ sequestration scenario, slow removal of ParA only allows the complex to advance a little farther in the cell, but it does not restore unidirectionality. Indeed, we predict that fast ParA sequestration is key to TipN restoring unidirectional segregation in cells.

4.5 Discussion

In this chapter we have presented two models that explore the mechanisms for the segregation of the circular chromosome of *C. crescendus* bacterium. In the first model, we

put forward a simple mechanism for how a ParB complex can hold on and move with a polymerizing/depolymerizing ParA bundle. From our model we deduced that if ParB is allowed to have multiple binding interactions with the ParA bundle which depolymerizes with a natural depolymerization rate, movement of the ParB complex toward the new pole can be sustained. We showed that in order to reproduce experimental observations ParB is required to depolymerize the ParA bundle with rates that are much lower than the natural depolymerization rate of the ParA bundle filaments. Thus, we predict that the ParB complex has a passive role in ParA bundle shortening. On the other hand, the velocity of ParB is directly dependent upon the ParA growth/shortening rates. We also showed that if polymerization is allowed in this simple model, segregation fails and the complex has an increased probability of experiencing backward motion toward the new pole. We thus predict that a simple mechanisms of biased diffusion of an array of binding sites on a bundle of depolymerizing polymers can be sufficient to allow ParB to track the edge of a retracting ParA bundle of polymers.

In the second part of the chapter, we presented a more generalized continuous model which built on the discrete model results in order to capture ParB/ParA interactions and also followed the biochemical reactions that ParA monomers and dimers undergo once released in the cytoplasm. From this continuous model, we obtained similar results to the discrete model, where biased diffusion coupled with a retracting polymer bundle generated proper segregation of the ParB complex. Next, using the continuous model we could test the effects of dimerization delay on the system as well as the effects of TipN proteins acting at the new pole end. Our model supports a scenario where TipN action on ParA monomers controls ParA dynamics and thus consequently the polymerization rate of the ParA bundle. Since ParB movement is sensitive to ParA growth/shortening rates, this TipN action is sufficient to control the direction of ParB movement. These results are in agreement with experimental observations. We tested two modes of TipN operation in the cell and showed that both mechanisms could work to properly segregate ParB in a dividing cell.

One of the most interesting aspects of the *C. Crescendus* models is that a recurring theme appears in chromosome movement machines across different cell types. We see that weak binding in conjunction with dynamic polymers and diffusion can produce movement of objects in the cell. The advantage of these dynamic assemblies in the context of cell division is that the direction and velocity of movement can be easily controlled biochemically by altering polymer dynamics.

4.6 References

[1] K. Gerdes, M. Howard, and F. Szardenings, *Pushing and pulling in prokaryotic DNA segregation*, Cell, 141 (2010), pp. 927–942.

[2] C. Jacobs-Wagner. personal communication, 2010.

[3] J. L. Ptacin, S. F. Lee, E. C. Garner, E. Toro, M. Eckart, L. R. Comolli, W. E. Moerner, and L. Shapiro, *A spindle-like apparatus guides bacterial chromosome segregation*, Nat. Cell Biol., 12 (2010), pp. 791–798.

[4] S. Ringgaard, J. van Zon, M. Howard, and K. Gerdes, *Movement and eqipositioning of plasmids by ParA filament disassembly*, Proc. Natl. Acad. Sci. USA, 106 (2010), pp. 19369–19374.

[5] W. B. Schofield, H. C. Lim, and C. Jacobs-Wagner, *Cell cycle coordination and regulation of bacterial chromosome segregation dynamics by polarly localized proteins*, EMBO J., 29 (2010), pp. 3068–3081.

[6] A. G. Vecchiarelli, Y. W. Han, X. Tan, M. Mizuuchi, R. Ghirlando, and C. Biertumpfel, *ATP control of dynamic P1 ParA-DNA interactions: a key role for the nucleoid in plasmid partition*, Mol. Microbiol., 78 (2010), pp. 78–91.

CHAPTER 5

CONCLUSIONS

In this thesis, we have presented mathematical models that describe mechanisms for how chromosome movement is sustained and controlled in eukaryotic and bacterial cells. In this chapter we give a brief overview of our model results and predictions.

5.1 Model results summary

In eukaryotic cells, a kinetochore is shown to move with velocities that match the balance of kMT tip rates. In Chapter 1 we asked the following question: How can very unstable polymers such as microtubules carry large loads such as chromosomes with constant velocities over significant distances? In Chapter 2, we presented a mathematical model of the mechanical coupling between chromosomes and dynamic microtubule polymers. The key components of this model were that kinetochores were composed of multiple binders which could associate with the kMT lattice. The binders would undergo diffusion on the microtubule lattice due to weak interactions with specific MT sites. Finally, the attached microtubules were assumed to grow or shorten with prescribed rates. We showed that multiple weak binders could indeed move with a growing or shortening polymer provided that it was energetically favorable for the system to engage as many binders as possible. In this model, diffusion is essential to warranting that a Kt motor is able to move. This because when the binders were allowed to have strong preference for specific binding sites, the effects of diffusion diminish and the motor is stalled without being able to readjust on the growing or shortening polymer. Therefore, in our model diffusion essentially lubricates the Kt/MT interaction such that the kinetochore can rearrange on the MT in order to move with the polymer tip. In the case of weak binding, we showed that kinetochore motors moved with rates that matched the balance of kMT polymerization/depolymerization rates, in agreement with experimental observations. We also were able to calculate how much load it took to break the motor. Note that a key property of binding in this case is that there be multiple interactions between the Kt and the microtubule, otherwise thermal effects overcome binding energies and cause a failure of the motor. This need for multiple weak

binding interactions in order to harvest the dynamics of polymers is a theme which we encountered again in Chapter 4.

A key and novel result of the Kt motor model is our study on the effect of Kt binder arrangement on motor velocities. We showed that if the binders are arranged off-register to the MT lattice, then diffusion could relocate the Kt more easily on the MT lattice so that the motor would be harder to stall as the binding affinity between the binder and the MT increased. Thus, we showed that a random arrangement of binders at the Kt might be advantageous to maintaining nonzero chromosome velocities.

Finally, an important contribution of the Kt motor we proposed in Chapter 2 has to do with the analytical expressions we obtained, for the first time, for the load-velocity relationship of kinetochore motors. These analytical results give us a quick way of assessing Kt movement velocities as a function of MT polymerization/depolymerization rates and motor loads.

Next, we posed two questions about the control of eukaryotic chromosome movement during mitosis: 1) why and how does directional instability of chromosome movement take place, 2) how is chromosome congression achieved and how do chemical signals affect ana-phase transition? In order to answer these questions, we constructed a model for chromosome movement during mitosis in Chapter 3. The underlying idea of the chromosome movement model was that chromosome movement is generated by a negative feedback mechanism between mechanical and chemical signals in the cell. For this model, we used results from the Kt motor model in the second chapter to get relationships between chromosome velocities, kMT rates and loads. We postulated that a localized chemical control mechanism is in place at each kinetochore. We constructed a minimal biochemical control loop which contained a force sensor protein, a kinase and a kinesin. The kinetochore chemical reactions were constructed to be switch-like, to be turned on and off depending on the amount of load or resistance that a chromosome feels at a given position in the cell. The load on the kinetochore motors in this model was assumed to arise due to interactions between spindle MTs and chromosome arms. We showed that the presence of switch-like chemical reactions introduces a delay in a negative feedback loop between loads and kMT rates- which results in oscillations. We showed that oscillations were bound to arise as long as the chemical switch at kinetochores provided enough delay to kinesin shut down in response to force.

Further, we showed that chemical control of movement in chromosomes is essential not only to generate oscillations, but also to establish a leading kinetochore during congression. Due to the asymmetry in forces that sister kinetochores feel when close to a pole, the sister

kinetochore chemical reactions are also asymmetrically activated. The chemical asymmetry, creates a propensity for kinetochores to move away from the pole independent of how many microtubules are attached on each side of the chromosome. Therefore, in our model a leading kinetochore is established independent of mechanical signals. This finding is in agreement with experimental observations which show that leading kinetochores during mitosis often contain fewer attached microtubules than the trailing kinetochore.

The control of the chemical feedback at kinetochores is key to proper transition of the cell during various phases of mitosis. We showed that if the chemical feedback was not properly disassembled at the beginning of anaphase, a chromosome would experience oscillations when approaching the poles. So we predicted that chromosome movement has a strong chemical component and is not the result of a simple balance of spindle and Kt motor forces.

For bacterial systems, we asked two questions concerning chromosome movement: 1) how do the interactions between ParA/ParB generate motion, and 2) how do chemical species at the cell poles control chromosome movement direction? We developed two models, where the underlying assumption for ParB/ParA interactions was that ParB had multiple binders that could diffuse on the lattice of ParA bundles, similar to the kinetochore model. The new element in this model had to do with the depolymerizing action of ParB. We showed that ParB would closely tack retracting ParA bundle edges to the new pole if it depolymerized the ParA polymers slowly compared to the natural ParA depolymerization rate. We also showed that the movement of ParB was directly dependent on ParA dynamics. In the case when ParA could depolymerize, then ParB moved to the new pole with velocities that were directly dependent on ParA depolymerization rates. In the case when ParA polymers were allowed to grow with rates proportional to ParA monomer concentrations, ParB also followed the stalled edges of ParA bundles and failed to properly congress. Thus, in this model biased diffusion coupled with depolymerizing ParA polymers and slow ParB depolymerization lead to chromosome congression, in agreement with experimental observations.

In wild type cells ParA has been shown to polymerize in the presence of ParA monomers. Using the second continuous model we set to test mechanisms by which the dynamics of ParA could be controlled in order to allow for ParA/ParB poleward movement. We introduced the action of the pole protein TipN in the model and showed that fast ParA monomer removal from the cytoplasm from the new pole fully restored unidirectional chromosome segregation. Thus, our model predicted that TipN is a necessary and sufficient

protein that can be used to control chromosome movement in these cells. The role of TipN in this system is similar to the role of MCAK in eukaryotic cells. The kinesin MCAK controlled the direction of chromosome movement and magnitude of velocities by modulating the depolymerization rate of attached MTs. On the other hand, TipN also controls ParB movement by modulating the polymerization rate of ParA. In the case of TipN, the action is delayed by the need of the ParA monomers to diffuse to the new pole where they can be removed or renucleated in the ParA bundle. However, for both cases we see that a unifying mechanism is at play for these dynamic polymer machines: movement control is achieved by modification of the biochemical reactions that control the growth/shortening rates of polymers that interact with chromosomes.

5.2 Future directions

In the context of eukaryotic cells, many questions remain open about chromosome movement. In the chromosome movement model of Chapter 2, only one chromosome was considered; however, in many eukaryotic cells several chromosomes move to the cell equator. An important aspect of this motility has to do with the coordination of chromosomes right before the cohesins break in anaphase. From experiments it is seen that the transition into anaphase is a well coordinated process; however, it is not known how such an event takes place. Recent data have pointed out that some of the chemical species which we considered in our model might be involved in the synchronization of chromosomes.

Another important aspect in mitosis is related to the mechano-chemical signaling pathways. In the model of Chapter 3, we considered chemical reactions which altered the rates of kMTs. However, a very large network of proteins localizes at kinetochores and constantly monitors the amount of force exerted at kinetochores. These proteins are part of the SAC network, and their primary function is to hold the mitotic checkpoint until all the chromosomes are properly attached. Experiments show that the loss of even a single kMT triggers a hold signal to the mitotic checkpoint. It is not known how these proteins check the attachment status of microtubules at kinetochores or how their signal can quickly amplify and propagate in a cell to prevent erroneously attached chromosomes from dividing.

In the context of *C. crescendus* many questions remain open. An important aspect of segregation here is related to the dynamics of ParA polymers. In our model in Chapter 4, we proposed that the filaments of ParA are disassembled from the tips distal to the new pole, similarly to spindle MTs. We also assumed that polymerization occurs at the ParA tips. Recent experimental data, however, suggest that ParA polymers might not be polar, so

that ParA growth may occur in either direction. This feature will require the modification of our model to test the case when polymerization and nucleation of ParA dimers is allowed to occur throughout the cell.

In conclusion, we have so far studied two cellular motors that were composed of arrangements of binders and dynamic polymers. These types of assemblies fall in the category of polymer motors, which operate by harvesting the energy of polymerizing and depolymerizing biopolymers. These polymer motors are thought to be the precursors of ATP-dependent motors such as dynein and kinesin. A key characteristic of these assemblies is that movement velocity and direction can be easily controlled by modulating the rates of polymer growth or shrinking. In the context of cell division, this flexibility of movement seems to be essential since chromosomes need to be able to rearrange their position in the cell until they can be placed either at the cell equator or at the new pole. Further, the chemical control of movement seems to be an important aspect, since it integrates chromosome movement into the larger network of chemical control of mitosis progression. We propose that this chemical control of motility in chromosome movement is very important not only for precise localization, but also for the cell to be able to check that movement is progressing in the right direction and no errors have occurred. Since mitosis errors are fatal to a cell, it makes sense that mechanical events in dividing cells be tightly controlled and chaperoned by chemical networks that set off a variety of checkpoints if there are mechanical anomalies.

APPENDIX

SUPPLEMENTARY INFORMATION

In this appendix we present supplemental assumptions and figures for the chromosome movement model discussed in Chapter 3.

A.1 Simplifying assumptions

We model the motion of only one chromosome. In newt lung cells with several chromosomes there could be interactions between motile chromosomes. We do not take any such interactions into account.

We assume that the biochemical reaction species are localized at the kinetochores i.e., do not diffuse in the cytoplasm.

We assume that each kMT is attached to a pole that has a fixed position (i.e., constant pole to pole distance). Also we ignore any flux effects at MT minus ends.

Polar ejection forces are assumed to be density dependent and thus modeled with a smooth distribution as in [4]. It is likely that this force distribution varies more with position and time, which in our context would produce less regular oscillations. Chromosome arms contain chromokinesin motors which are thought to contribute in the generation of polar ejection forces. We do not directly model fluctuations in chromokinesin motor activity.

A.2 Potential well for the motor

Note that in agreement with [3] and [4] we position the binding sites so that a fully attached coupler binds 65 sites along 40 nm of the polymer lattice with each site separated by $\delta = \frac{8 \text{ nm per monomer}}{13 \text{ protofilaments}}$. The equation for the well is given by,

$$\Psi(y) = \begin{cases} 0 & 0 \le x < \frac{\delta}{2} \\ (n-1)\left(-\frac{3a}{2} + \frac{b}{2} - \frac{b+a}{2}\cos(\frac{2\pi x}{\delta})\right) & \frac{(2n-1)\delta}{2} \le x < n\delta \\ n\left(-a + \frac{b}{2} - \frac{b}{2}\cos(\frac{2\pi x}{\delta})\right) & n\delta \le x < \frac{(2n+1)\delta}{2}. \end{cases}$$

A.3 Cohesin spring stiffness

For our cohesin springs we used the spring coefficient estimated by [4] of .1 pN/nm and a relaxed intra-kinetochore distance of 1 μm as measured in [7]. The magnitude of the spring coefficient dictates sister kinetochore coupling during bioriented movement. We tested several values and observed that if the spring coefficient is lowered to 0.001 pN/nm coupling is almost completely lost with bioriented oscillations looking like monooriented oscillations around the equator. Higher spring coefficients (up to .2 pN/nm) on the other hand, enhance sister chromatid coupling but also lower oscillation amplitudes since loads are greatly increased when a kinetochore tries to initiate movement away from the equator. Intermediate values allow for both coupling and reasonable amplitudes. Furthermore, we have imposed repulsion for springs compressing more than L_k, which corresponds to a physical barrier that does not allow chromosome arms to get closer than what has been observed experimentally.

A.4 Chemical reaction parameter estimation

We estimated the parameters for growth and decay of S so that the amplitude and frequency of monooriented chromosome oscillations (which are the most regular ones) matched data from newt lung cells in [5]. For the kinetic parameters of the bicyclic phosphorylation cascade we use the values of K_A, K_M, k_A^+, k_A^-, k_M^-, k_M^+ estimated in [6], similar to the cascade parameters for cyclin and Cdc2 kinase in [2]. These parameters give the needed time delays for chromosomal directional switches.

A.5 Congression and AP force gradient

For the simulation of the monooriented chromosome the AP force density factor is decreased to allow the chromosome to move close enough to the pole to which it is attached. Lower gradients can be justified since it takes time for the astral microtubules to grow enough to exert forces on the arms so that AP forces gain strength as mitosis progresses. Thus, we envision this gradient to gain strength over time. For congression the factor was increased to allow timely equator approach. After congression is achieved the AP gradient is increased to reach the measured value of ≈ 100 pN at 2 μm from the equator [1].

A.6 System with noise

To study the effects of noise we include the stochastic forcing term $\xi(t)$ with $<\xi_i>=0$, $<\xi_i(t_1), \xi_i(t_2)>=\sigma_i^2\delta(t_1-t_2)$ which perturbs the velocity of each kinetochore. The equations

of motion (3.1) are modified to be of the form

$$\nu \frac{dx_i}{dt} = \sum F + \xi(t), \tag{A.1}$$

In the simulations the noise level is adjusted to be such that $\sigma_i/V_{\max}$=.06, where V_{max} is the effective maximal velocity the system reaches when there is no noise.

A.7 Supplementary Figures

In this section we present supplemental figures for Chapter 3.

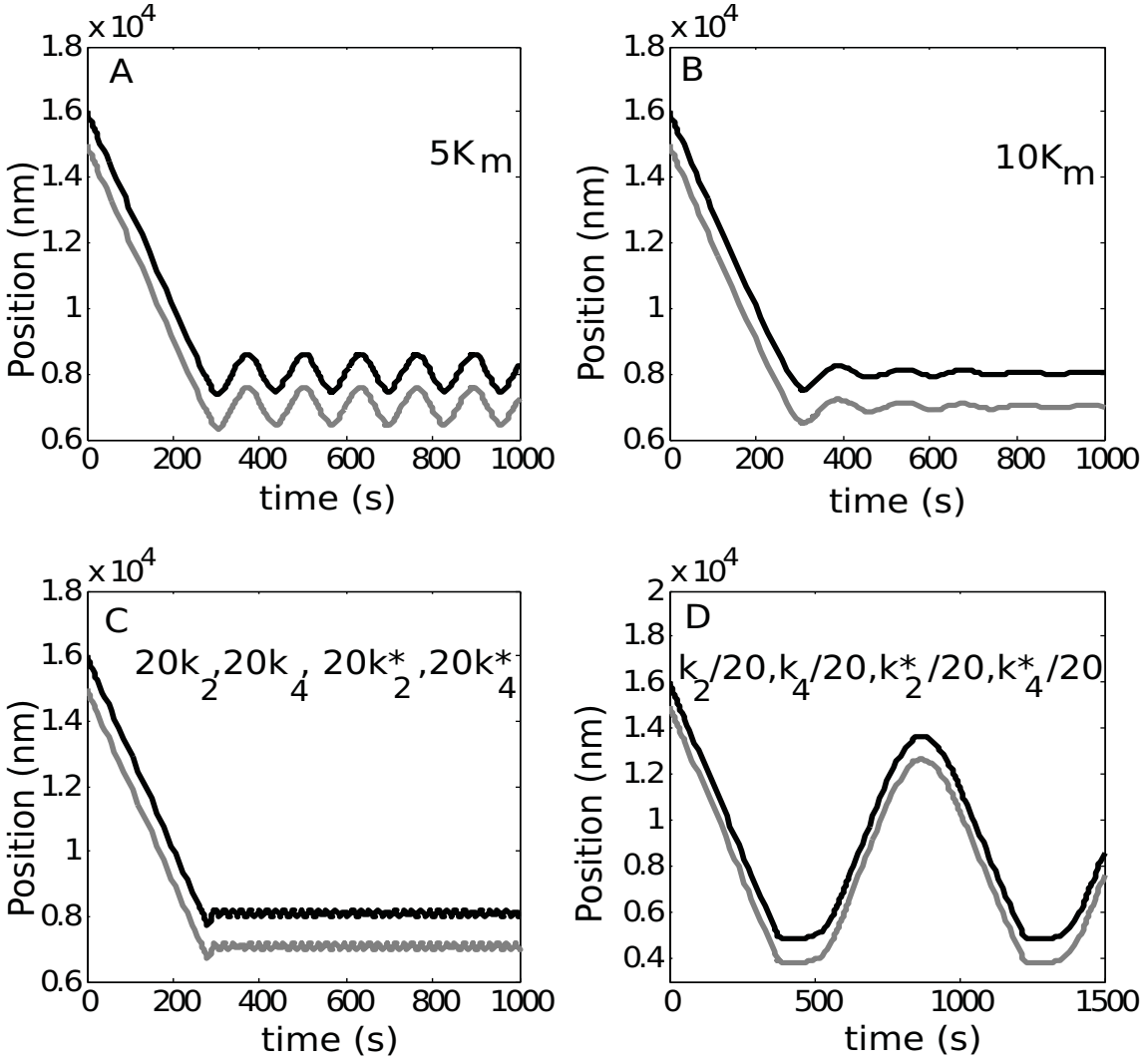

Figure A.1. Monooriented oscillations dependence on phosphorylation cascade kinetic parameters. For each plot only the parameters indicated in the legend are varied; the rest of parameters are kept the same as in the main text. (A-B) System oscillations are sensitive to K_m values, allowing for up to $10K_m$ before oscillations are lost. (C-D) For $K_m = .01$ nM, oscillations persist for a wide range of cascade kinetic parameters, even for $k_i < k_i/20$ and $k_i > 20k_i$, however oscillation amplitudes vary accordingly and we restricted our plots to parameter values for which oscillations can be easily depicted.

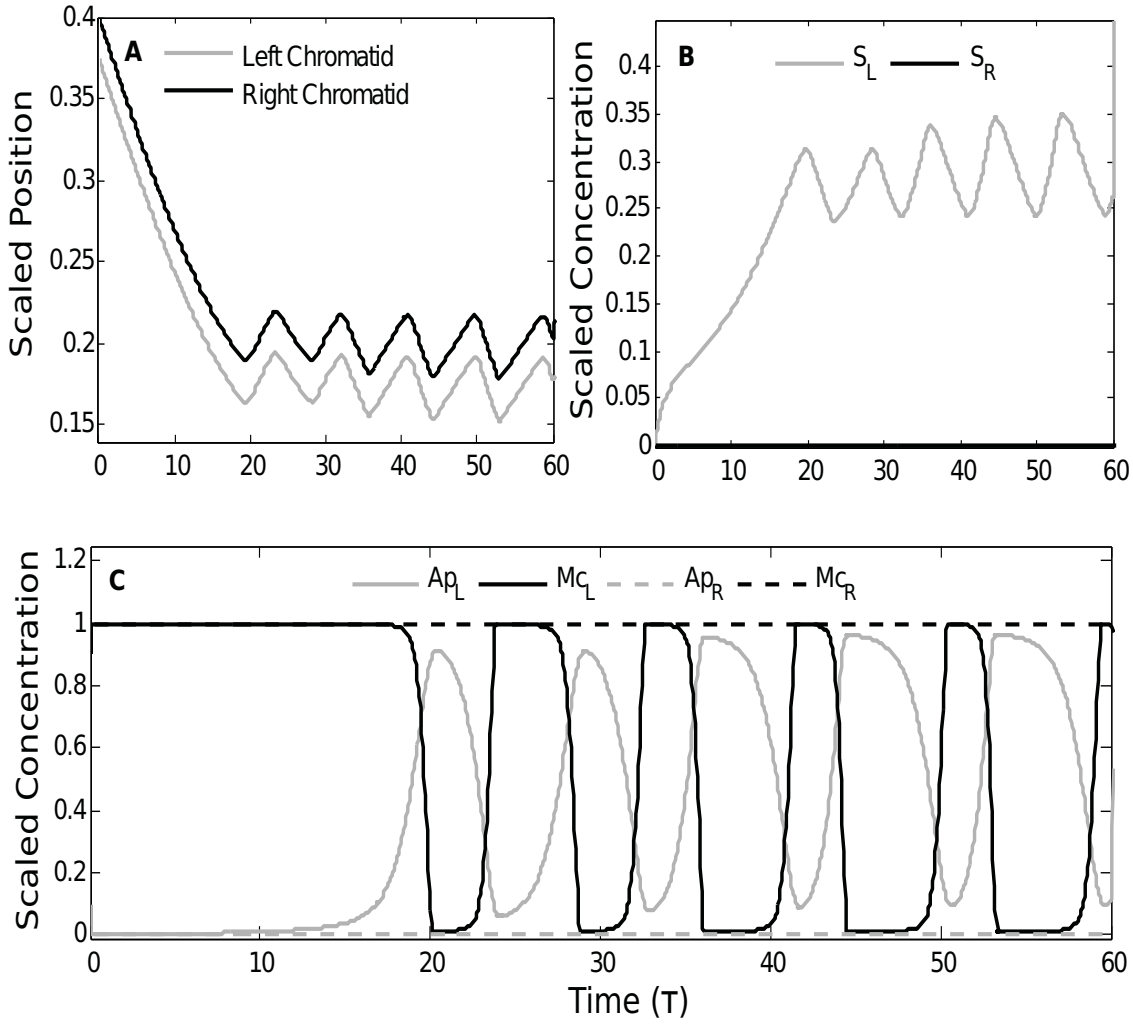

Figure A.2. Monooriented chromosome oscillations with linear load-velocity curves. (A) Chromatid positions are controlled by respective feedback loops acting via the linear load-velocity curves. The left pole is located at $\chi = 0$. The initial conditions for sister chromatids are: $\chi_L = 0.375$,$\chi_R = 0.4$; s_L=s_R=0; a_L=a_R=0.1,m_L=m_R=0.9.(B and C) Chemical species levels during chromosome oscillations.

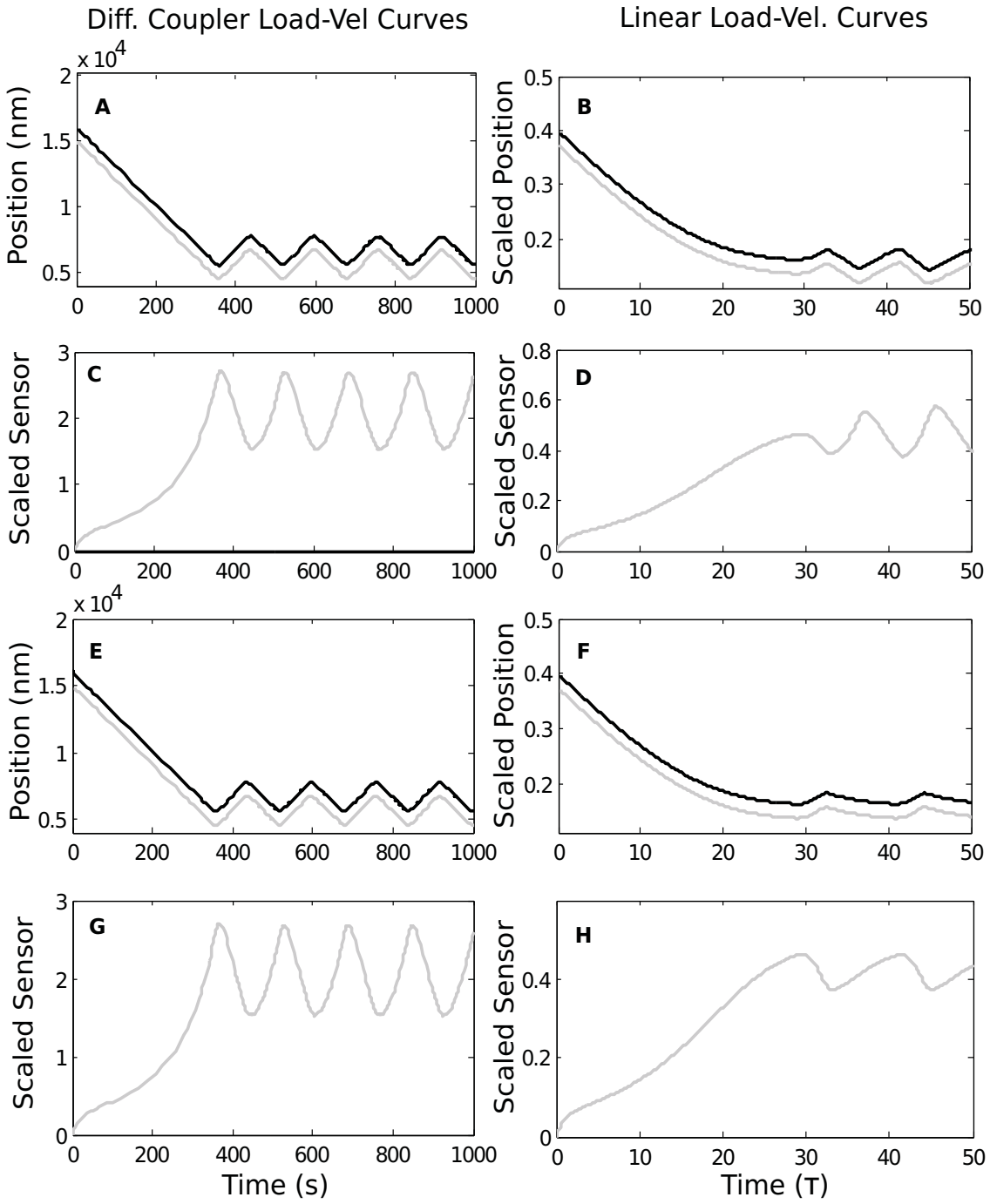

Figure A.3. Monooriented oscillations comparison between the linear and diffusive couplers for sensor rate variations. (A-B) The sensor growth rate is decreased from k=.02 to k=.0125 for both the linear and diffusive couplers. (C-D) Sensor levels for each coupler shown from A and B. (E-F) Monooriented oscillations for a single left Kt attachment. The sensor growth rate is set to k=.0125 for both couplers. (G-H) Sensor levels for each type of coupler (shown in E and F) with only one attachment at the left Kt.

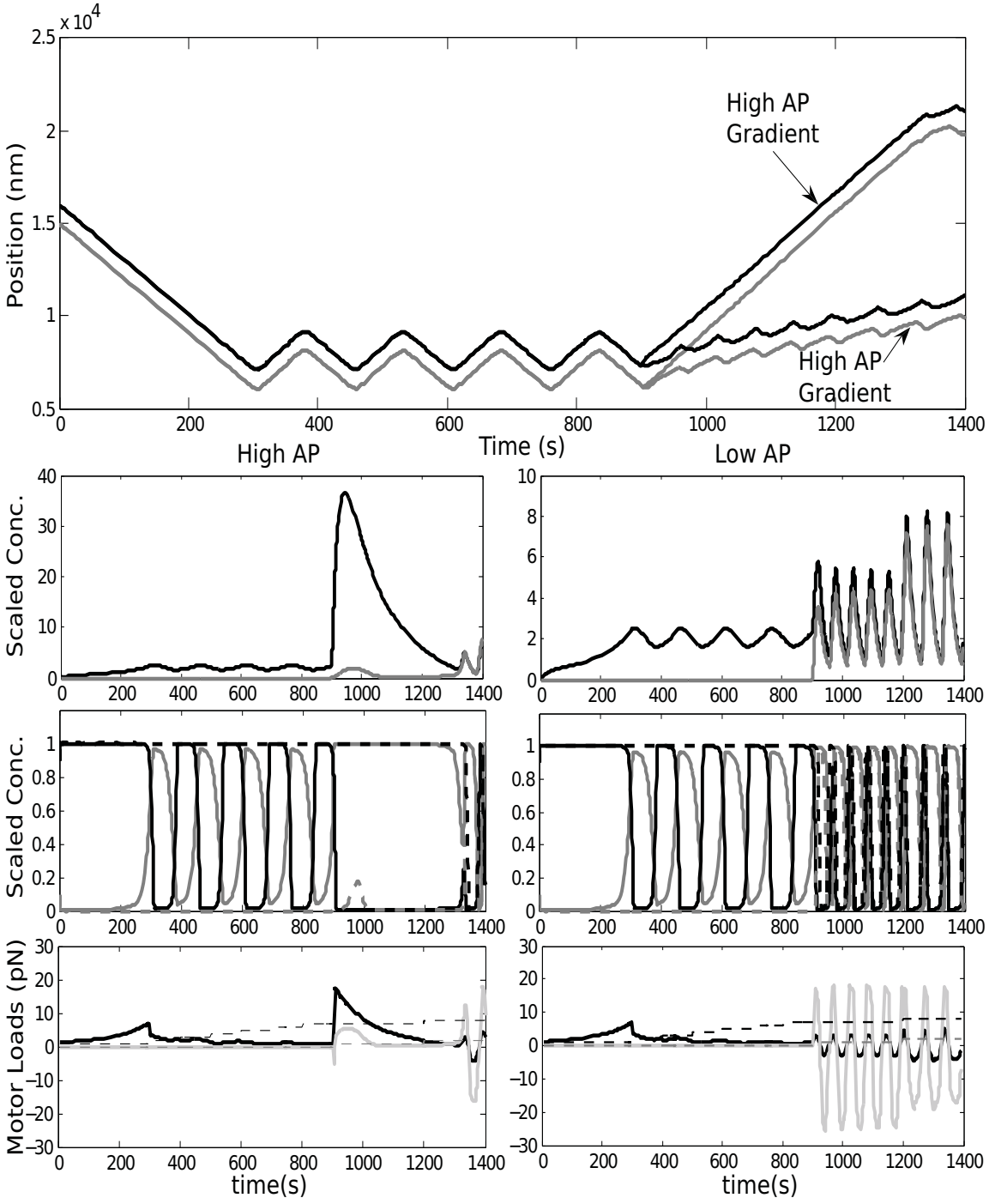

Figure A.4. Congression depends on the strength of the AP gradient. For low gradients a bioriented chromosome starts oscillating close to the pole taking a long time to congress. Higher gradients, however, allow for congression. The cascade and loads follow sensor dynamics.

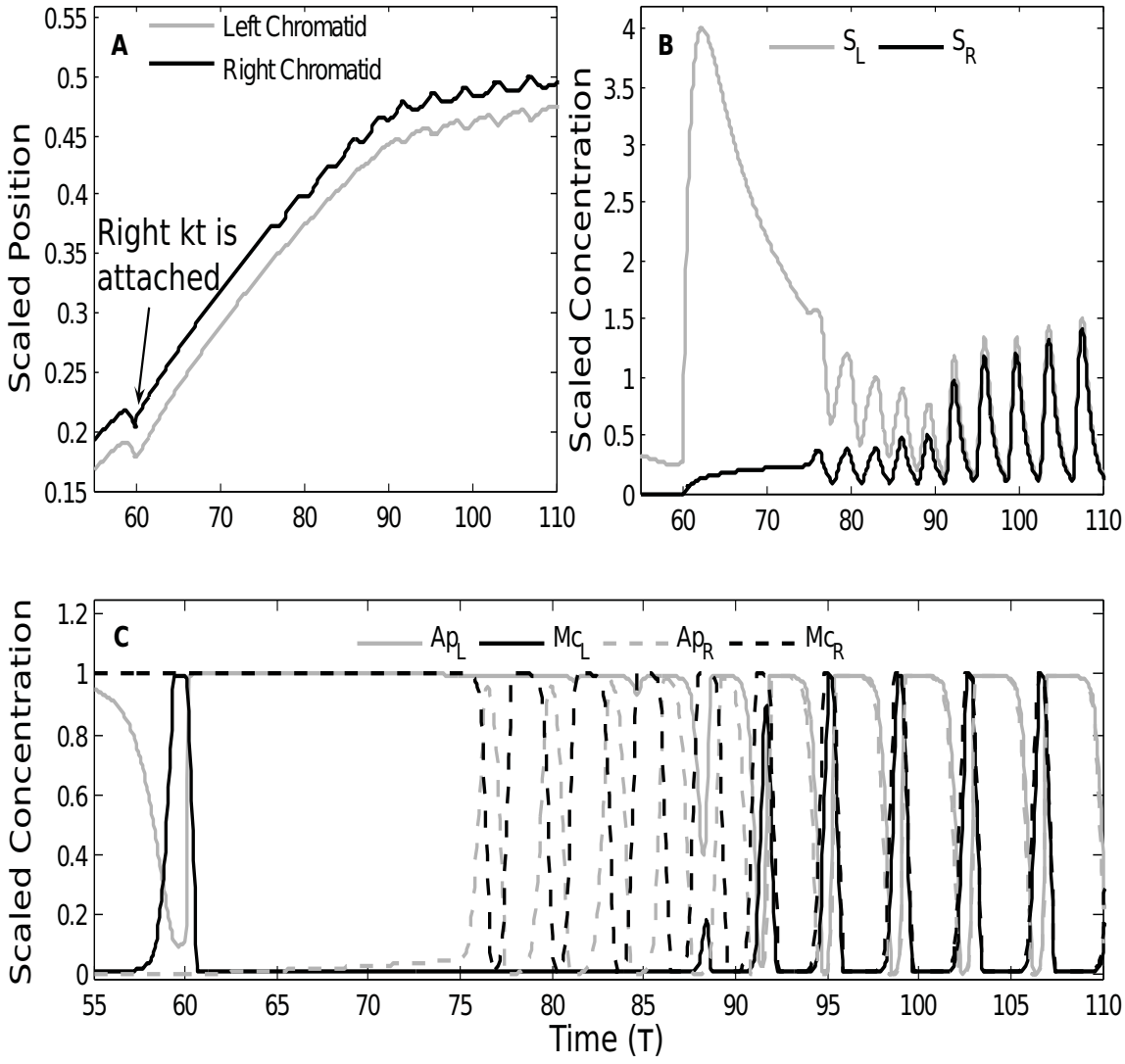

Figure A.5. Bioriented congression for linear couplers. (A) The position of a chromosome which becomes bioriented at $\tau = 60$ (7 left couplers and 1 right coupler). Despite unequal attachment numbers, a leading Kt is established and congression is achieved. (B and C) Chemical species levels.

A.8 References

[1] G. J. Brouhard and A. J. Hunt, *Microtubule movements on the arms of mitotic chromosomes: Polar ejection forces quantified in vitro*, Proc. Natl. Acad. Sci. USA, 102 (2005), pp. 13903–13908.

[2] A. Goldbeter, *A minimal cascade model for the mitotic oscillator involving cyclin and Cdc2 kinase*, Proc. Natl. Acad. Sci. USA, 88 (1991), pp. 9107–9111.

[3] T. L. Hill, *Theoretical problems related to the attachment of microtubules to kinetochores*, Proc. Natl. Acad. Sci. USA, 82 (1985), pp. 4404–4408.

[4] A. P. Joglekar and A. J. Hunt, *Simple mechanistic model for directional instability during mitotic chromosome movement*, Biophys. J., 83 (2002), pp. 42–58.

[5] R. V. Skibbens, V. Petrie-Skeen, and E. D. Salmon, *Directional instability of kinetochore motility during chromosome congression and segregation in mitotic newt lung cells: a push pull mechanism*, J. Cell Biol., 122 (1993), pp. 859–875.

[6] J. J. Tyson, K. C. Chen, and B. Novak, *Sniffers, buzzers, toggles and blinkers: dynamics of regulatory and signaling pathways in the cell*, Curr. Opin. Cell Biol., 15 (2003), pp. 221–231.

[7] J. C. Waters, R. V. Skibbens, and E. D. Salmon, *Oscillating mitotic newt lung cell kinetochores are, on average, under tension and rarely push*, J. Cell Sci., 109 (1996), pp. 2823–2831.